3-2006

Air Gap Error Compensation for Coaxial Transmission Line Method of Electromagnetic Material Characterization

Ronald G. Fehlen

AIR GAP ERROR COMPENSATION FOR COAXIAL TRANSMISSION LINE METHOD OF ELECTROMAGNETIC MATERIAL CHARACTERIZATION

THESIS

Ronald G. Fehlen, Captain, USAF

AFIT/GE/ENG/06-20

DEPARTMENT OF THE AIR FORCE
AIR UNIVERSITY

AIR FORCE INSTITUTE OF TECHNOLOGY

Wright-Patterson Air Force Base, Ohio

The views expressed in this thesis are those of the author and do not reflect the official policy or position of the United States Air Force, Department of Defense, or the United States Government.

AFIT/GE/ENG/06-20

AIR GAP ERROR COMPENSATION FOR COAXIAL TRANSMISSION LINE METHOD OF ELECTROMAGNETIC MATERIAL CHARACTERIZATION

THESIS

Presented to the Faculty

Department of Electrical and Computer Engineering

Graduate School of Engineering and Management

Air Force Institute of Technology

Air University

Air Education and Training Command

In Partial Fulfillment of the Requirements for the

Degree of Master of Science in Electrical Engineering

Ronald G. Fehlen, B.S.E.E.

Captain, USAF

March 2006

AFIT/GE/ENG/06-20

AIR GAP ERROR COMPENSATION FOR COAXIAL TRANSMISSION LINE METHOD OF ELECTROMAGNETIC MATERIAL CHARACTERIZATION

Ronald G. Fehlen, B.S.E.E.

Captain, USAF

Approved:

/signed/	21 Mar 2006
Dr. Michael J. Havrilla (Chairman)	date
/signed/	21 Mar 2006
Dr. William P. Baker (Member)	date
/signed/	21 Mar 2006
Dr. Andrew J. Terzouli (Member)	date

Abstract

This research analyzes material characterization measurements where axially symmetric air gaps exist between the sample material and the inner or outer conductor of a coaxial test fixture. Higher order fields are excited by the air gap and are not accounted for in generally used algorithms for determining the material permittivity and permeability. The result is error in the material characterization measurement.

This research defines the fields within the material and air gap, assuming them to be axially symmetric. The fields are then used via the modal method to calculate theoretical scattering parameters as a function of permittivity, permeability, and frequency. A complex, two-dimensional Newton root search then iterates the permittivity and permeability for a given frequency minimizing the difference between the calculated scattering parameters and the measured scattering parameters. In this manner, the root corresponds to the permittivity and permeability of the sample.

The modal method provides accurate results for non-magnetic material measurements when the material sample fills only 30% of the radial distance between the inner and outer conductor of the coaxial line. Due to the concentration of the electric field at the inner conductor, accurate results were achieved with a 29.25 mil material layer (400 mil air gap) on the inner conductor. It is shown that the modal method result converges to the material properties by using 10 modes.

The modal method provides good results for high-dielectric constant magnetic material. Results for an outer gap scenario were more accurate than inner gap results. The modal method appears to converge with very little error at approximately 20 modes, but diverges for greater than 20 modes. This behavior is not expected and is attributed to a failure of computer calculated Bessel functions with large real and small complex arguments.

The sensitivity of results to uncertainty in sample radial thickness and length measurements were analyzed. Uncertainty in the radial thickness was the dominate source of error, particularly when the air gap is large or the material is heavily loaded.

Two factors significantly impacted the performance of the modal method. First, the presence of an air gap effects the physical support to the center conductor. For the air gap to remain axially symmetric (a fundamental assumption of this research), the center conductor must remain along the axis of the test fixture outer conductor. Second, accurately determining the z-directed wavenumber in the material and air gap region is critical and requires much care, particularly when measuring heavily loaded materials.

Acknowledgements

The act of discovery is making known what was previously unknown. There is nothing new, only that which is unknown. And all that is unknown to us, is known by its Creator. Logic compels then an inescapable gratitude and awe toward He who created what we discover and for His grant of curiosity and mental capability. With these tools He allows us to pull back the mist of His creation, not for our own pride or self-advancement, but to reveal Himself, His majesty and His great power in speaking it into existence. Thank God for His grace, His mercy, and the His love on which the former are founded.

I must also thank my wife and best friend. Her support was immeasurable and unfailing. What we accomplish together, our Lord with us, I could never accomplish on my own. And to my patient and understanding boys, thank you.

This research was greatly encouraged along by and builds upon the ideas of Dr. Michael Havrilla. Thank you for your seemingly inexhaustible time and care. I have truly stood on the shoulders of a giant.

Ronald G. Fehlen

Table of Contents

Page

Abstract iv

Acknowledgements vi

List of Figures viii

List of Tables ix

List of Abbreviations x

I. Introduction 1
- 1.1 Material Characterization 1
- 1.2 Accounting for Discontinuity Error 2

II. Discontinuity Error in Coaxial Line Material Measurements . . . 4
- 2.1 Why a Coaxial Test Fixture? 4
- 2.2 NRW Algorithm and Discontinuities 6
- 2.3 Radial Air Gap Discontinuities 8
- 2.4 Air Gap Correction 13
- 2.5 Fields in Region with Sample and Air Gap 18
- 2.6 Summary 26

III. Full Wave Modal Method 30
- 3.1 General Modal Analysis 30
  - 3.1.1 General Definition of System Modes 31
  - 3.1.2 Application of Boundary Conditions 35
  - 3.1.3 Select and Apply Testing Operator 37
- 3.2 Application of Modal Analysis 41
  - 3.2.1 Mode Dependent Transverse Electric and Magnetic Field Vectors 41
  - 3.2.2 Mode Coupling Integrals in Coaxial Line 47
- 3.3 Summary 51

IV. Full Wave Modal Method Results 53
- 4.1 Test Setup 53
- 4.2 Error Analysis 55
- 4.3 Modal Method Performance 56
  - 4.3.1 Modal method performance for Rexolite® . . . 56

Page

4.3.2 Modal method performance for MagRAM . . . 60
4.4 Root Search Algorithm Performance . . . 64
4.4.1 Newton Root Search for Minimization . . . 69
4.4.2 Muller Root Search for Wavenumbers . . . 70

V. Conclusions and Recommendations for Improvement . . . 79
5.1 Recommended Improvements . . . 79
5.1.1 Initial Guesses for Wavenumbers . . . 79
5.1.2 Compensation for Eccentric Center Conductor . 79
5.1.3 Compensation for Eccentric Material . . . 80
5.1.4 Impedance Boundary Conditions . . . 81
5.1.5 Time Domain Analysis of Scattering Parameters 83
5.1.6 Non-linear Least Squares Algorithm for Minimization . . . 83
5.1.7 Efficiency in calculation of Bessel Functions . . 84

Appendix A. Wave Equation . . . 85

Appendix B. Solution to Helmholtz's Wave Equation in Cylindrical Coordinates . . . 88

Appendix C. Cutoff Frequency of a TEM Field . . . 91

Appendix D. TEM and TM Mode Orthogonality . . . 94
D.1 General Field Solution in Cylindrical Coordinates . . . 94
D.2 Orthogonality of $\hat{z}$ directed fields . . . 95
D.3 Orthogonality of transverse fields . . . 97

Appendix E. Bessel Integration Identities . . . 99

Appendix F. Fields Within a Coaxial Transmission Line . . . 103
F.1 TM Fields in a Coaxial Line . . . 103
F.2 TEM Fields in a Coaxial Line . . . 105

Appendix G. Transverse Mode dependent Vector Coupling Integrals . 108
G.1 Symbols Defined . . . 108
G.1.1 General . . . 108
G.1.2 Regions I and III (Freespace) . . . 108
G.1.3 Region II (Material with Air Gap) . . . 108
G.2 TEM testing operator coupling to Region II TM fields . 109
G.3 TM testing operator coupling to Region II TM fields . . 111

Page

Appendix H. Higher Order Mode Excitation By Waveguide Discontinuity 115

Bibliography 119

List of Figures

Figure		Page
1.1.	Disassembled Coaxial Test Fixture	3
2.1.	Test Setup Diagram	5
2.2.	Coaxial line cross sections with different air gap scenarios	9
2.3.	High temperature ceramic material measurement problem	10
2.4.	Effect of 100 mil Air Gap on Rexolite® measurement	13
2.5.	Effect of 9 mil air gap in MagRAM measurements	14
2.6.	Lumped circuit air gap correction for Rexolite® measurements	18
2.7.	Lumped circuit air gap correction for MagRAM measurements	19
2.8.	Lumped circuit correction for MagRAM measurement of real permittivity at 2 GHz	20
2.9.	Exclusion of TEM wave when air gap exists	21
2.10.	Rexolite® TEM and air gap TM^z Field Profiles	28
2.11.	MagRAM TEM and air gap TM^z Field Profiles	29
3.1.	Inner and outer air gap modal diagram and coaxial line dimensions	34
4.1.	Coaxial test fixture center conductor inserted	54
4.2.	Assembled coaxial test fixture	54
4.3.	10 Mode Correction to Rexolite® with 100 mil air gap	60
4.4.	Error Analysis for Rexolite® with 100 mil inner air gap	61
4.5.	Mode Sweep at 2 GHz for Rexolite® with 100 mil air gap	61
4.6.	Effect of eccentric center conductor on Rexolite® with 400 mil air gap	62
4.7.	Modal method performance at 2 GHz for Rexolite® with increasing outer air gap size	62
4.8.	10 Mode Correction to MagRAM with 9 mil air gap	65
4.9.	Effect of 9 mil air gap in MagRAM measurements	66
4.10.	Mode Sweep at 1 GHz for MagRAM with 9 mil air gap	67

Figure Page

4.11. Modal method performance at 2 GHz for MagRAM with increasing outer air gap size 68

4.12. Newton root search solution surface for non-magnetic material 71

4.13. Wavenumbers as a function of frequency for MagRAM with 9 mil inner air gap 75

4.14. Solutions to Characteristic Equation as Gamma is varied . . . 76

4.15. 50 Wavenumbers at 50 MHz for MagRAM with 9 mil inner air gap 78

5.1. Center Conductor Droop in Coaxial Line 80

5.2. Dimensioned Center Conductor Droop 81

5.3. Eccentric material diagram 82

5.4. Coaxial Line Empty Measurement 83

D.1. Integration Paths for Orthogonality Proof 96

G.1. Diagram of coaxial line with air gap 114

H.1. Waveguide Transverse and Step Discontinuities 118

List of Tables

Table		Page
2.1.	First 10 modes and cutoff frequencies in freespace filled coaxial line	7
2.2.	Wavenumbers in Rexolite® with 100 mil inner and outer air gaps	27
2.3.	Wavenumbers in MagRAM with 9 mil inner and outer air gaps	27
F.1.	Bessel and logarithmic function small argument limits	107

List of Abbreviations

Abbreviation		Page
T/R	Transmission/Reflection	1
NRW	Nicolson-Ross-Weir Algorithm	1
NWA	Network Analyzer	4
TEM	Transverse Electromagnetic Field	4
TRL	Thru, Reflect, Line	7
MagRAM	Magnetic Radar Absorbing Material	11
NIST	National Institute of Standards and Technology	13
MAM	Modal Analysis Matrix	31

AIR GAP ERROR COMPENSATION FOR COAXIAL TRANSMISSION LINE METHOD OF ELECTROMAGNETIC MATERIAL CHARACTERIZATION

I. Introduction

A material's response to the application of an electromagnetic field is quantified by the material's complex permittivity and permeability. The real and imaginary parts can be viewed as the susceptibility to polarization and attenuation (or loss) respectively. The permittivity is in response to the electric field and the permeability to the magnetic field.

A material's permittivity and permeability are exploited for a wide variety of antenna, electromagnetic interference, and low signature applications. Accurate characterization of a material's electromagnetic properties is therefore a necessary and crucial step in the research, development, and design of new material mixture formulas and in the verification of manufacturing processes.

1.1 Material Characterization

The Transmission/Reflection (T/R) method of material characterization determines the complex permittivity and permeability of a linear, homogeneous, isotropic material by measuring the material's scattering parameters [4]. A sample of the material is mounted internal to a test fixture and an attached network analyzer measures the scattering parameters necessary to determine the material's electromagnetic properties. The well-known Nicolson-Ross-Weir (NRW) algorithm extracts the material parameters from the measured scattering parameters [12, 17]. The NRW algorithm assumes the unknown material completely fills the cross sectional area of the test fixture. This assumption, in conjunction with the measurement frequency band, restricts the fields within the test fixture to a single propagating mode.

Discontinuities may unintentionally exist within the test fixture as a result of imprecise machining of the sample or other defect. Deliberate discontinuities are also possible. For example, high temperature measurements are prone to gaps due to the different thermal expansion rates for the material and conductor.

Discontinuities in the test fixture will excite high-order evanescent or higher-order propagating modes. Due to the conservation of energy and mode orthogonality, the incident field power will couple into both classes of higher order modes. Detection circuitry within the network analyzer is typically too far from the forward face of the material under test to detect power coupled into higher-order evanescent waves. Additionally, the test setup (network analyzer and test fixture) is normally designed to excite and detect only one field, the dominant mode. If higher-order propagating modes are excited, their power will not be effectively identified by the detector element.

1.2 Accounting for Discontinuity Error

The power loss to higher-order modes is a source of measurement error in the NRW algorithm. This research seeks to account for the error induced when higher-order modes are excited in order to accurately determine the material parameters in such cases.

The test fixture for this research is the coaxial line shown in figure 1.1. The discontinuities considered in this research are axially symmetric air gaps between the outer radius of the sample or the inner radius of the outer conductor.

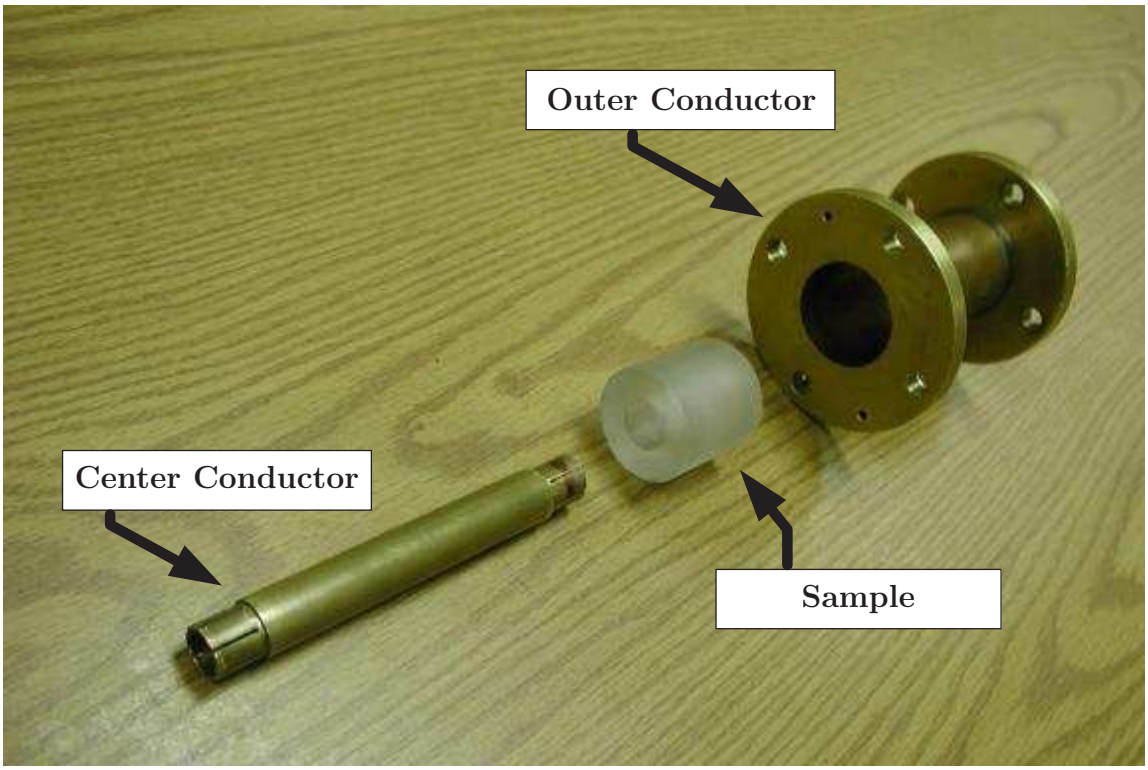

Figure 1.1: Disassembled Coaxial Test Fixture and Rexolite Sample®

II. Discontinuity Error in Coaxial Line Material Measurements

The T/R method of material characterization is widely used due to its simplicity [4] and is the measurement method for this research. The method requires a single measurement device, typically a network analyzer (NWA), and a means to mount the sample for testing, typically a waveguide test fixture. This research uses a coaxial line as the test fixture. The system is connected as shown in figure 2.1.

2.1 Why a Coaxial Test Fixture?

Measurement frequency band is a primary concern when selecting a test fixture. A two conductor, coaxial transmission line's ability to propagate a TEM wave makes it an ideal fixture for tests that require relatively broadband, low frequency measurements. Additionally, the typically small size of a coaxial line ensures a reasonable material sample size.

Each field configuration (mode) within a waveguide has a lower frequency bound known as the cutoff frequency. The propagating mode with the lowest frequency bound is the dominant mode for a given waveguide. The cutoff frequency is determined from waveguide boundary conditions and, in the case of rectangular and cylindrical single-conductor waveguide, is inversely proportional to the dimensions of the waveguide therefore requiring very large dimensions to measure low frequencies [3]. On the other hand, a multi-conductor waveguide is unique in its ability to propagate a TEM wave. The cutoff frequency for a TEM wave is 0 Hz (see appendix C) making it the dominant mode in a multi-conductor waveguide such as a coaxial line. This fact permits low frequency material measurements.

The dimensions of the coaxial test fixture dictate the measurement frequency bandwidth. The coaxial test fixture for this research has an inner conductor of radius $a = 0.331$ inches and outer conductor radius of $b = 0.76025$ inches. The bandwidth of the measurement is typically kept at $\approx 90\%$ of the dominant mode bandwidth. As

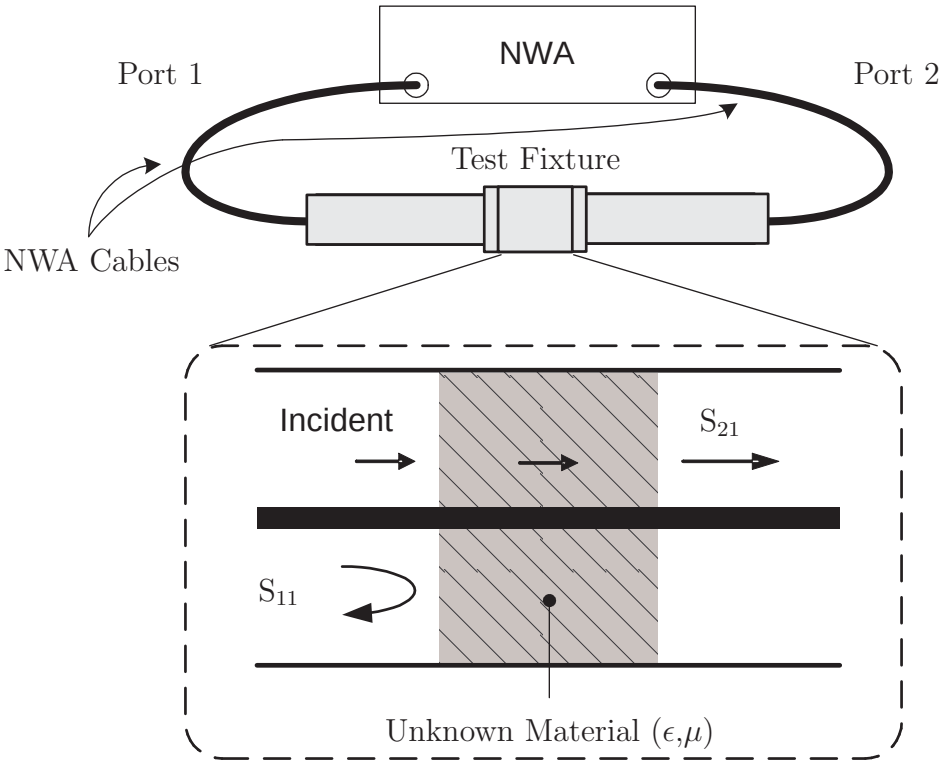

Figure 2.1: Test setup with an exploded view of the test fixture and mounted sample. The forward scattering parameters, S_{11} and S_{21}, are measured at the NWA ports 1 and 2 respectively.

seen from table 2.1, the first higher order mode in the coaxial test fixture is the TE_{11} with a cutoff frequency of 3.5 GHz [10]. This sets the upper frequency bound.

Although the cutoff of a TEM is a 0 Hz, the lower frequency bound of the NWA is 50 MHz. Therefore, the measurement frequency bandwidth for this research is 50 Mhz to 3.05 GHz or $\approx 85\%$ of the available TEM bandwidth.

The frequency bounds must consider the evanescent fields excited by the transition from the NWA cables to the coaxial test fixture. These fields may not propagate, but they may not decay rapidly either. For example, a 50 Mhz TEM wave in the freespace filled region of the coaxial line in this research will lose 63% of its field strength in approximately 0.94 m. If a sample is placed to close to the end of the coaxial test fixture, there will be error due to the higher order evanescent modes excited at the transition. This research assumes a single mode excitation, meaning the sample is far enough away from the end of the coaxial test fixture with respect to the given measurement frequency band.

The coaxial line dimensions also define the amount of sample needed and the impedance of the test fixture. The coaxial line in this research requires only a 1.5205 in. by 1.5205 in. sample to fill the cross section. Additionally, the coaxial line dimensions produce an impedance

$$Z = \frac{1}{2\pi} \ln\left(\frac{b}{a}\right) \sqrt{\frac{\mu_0}{\epsilon_0}} = 49.85\Omega \approx 50\Omega$$

necessary to match the characteristic impedance of the NWA cables.

2.2 NRW Algorithm and Discontinuities

The network analyzer excites a field, typically of the dominant mode, that travels through the waveguide until it strikes the mounted sample. A portion of the incident field is reflected and a portion transmitted through the material. The magnitude and phase of the reflected and transmitted field is measured by the network analyzer and reported as complex scattering parameters S_{11} and S_{21} (see figure 2.1).

Table 2.1: The first 10 modes in a coaxial line with inner conductor of radius 0.331 inches and outer conductor radius of 0.76025 inches. The TE_{02} and TM_{11} are expected to have the same cutoff frequency [10].

Freespace Filled Coax			
Mode	Cutoff Frequency [GHz]	γ	$k_\rho = k_c$
TEM	0.000	$0.0+41.9j$	$0.0+0.0j$
TE_{11}	3.514	60.6	73.6
TE_{21}	6.888	138.1	144.4
TE_{31}	10.041	206.2	210.4
TE_{41}	12.986	268.9	272.2
TM_{01}	13.633	282.6	285.7
TE_{02}	14.088	292.3	295.3
TM_{11}	14.088	292.3	295.3
TE_{12}	14.652	304.2	307.1
TM_{21}	15.364	319.3	322.0

Physically, S_{11} and S_{21} are the ratio of the reflected field amplitude and transmitted field amplitude, respectively, to the incident field amplitude under matched conditions. The NRW algorithm provides analytical expressions for the permittivity and permeability of the sample as a function of the measured scattering parameters[1], S_{11} and S_{21} [4, 12, 17].

A calibrated system is critical for obtaining accurate measurements. Mismatches at cable connections, waveguide deformities, and coupling between measurement devices at ports 1 and 2 are just a few items that will introduce error into the measurement. Calibration will significantly reduce the impact these defects have on the measurements. This research assumes a properly calibrated system via a Thru, Reflect, Line (TRL) technique and that measured data is representative of the properties of the sample, not system imperfections. The details of system calibrations and specifically the TRL calibration, are thoroughly discussed in [4].

[1]Although the forward scattering parameters S_{11} and S_{21} are discussed in the text, they are interchangeable with the reverse scattering parameters S_{22} and S_{12} respectively. Measurement of S_{22} and S_{12} require exciting the incident field at port 2.

A fundamental assumption of the NRW method is that the power in the system is carried by a single mode (typically the dominant mode) and is therefore completely measured by the NWA and quantified in the S_{11} and S_{21} measurements. The orthogonality of field modes (see appendix D) ensures that a single mode excitation in a uniform guiding structure will carry the power in the system. If higher order modes are excited within the structure, power carried by the initial excitation will couple into the higher order modes, but will typically evanescence due to the cutoff frequency of the higher mode being greater than the measurement frequency band. This represents a loss in power and, consequently, perturbation in the S_{11} and S_{21} measurements. Not all discontinuities will excite higher order modes (as shown in appendix H), but if higher order modes are excited, they must be accounted for to produce accurate material parameter results.

2.3 Radial Air Gap Discontinuities

Radial air gap discontinuities as shown in figure 2.2b and 2.2c are the primary focus of this research. Samples are typically machined via a lathe by experienced machinists and therefore, if discontinuities exist, they are assumed to be axially symmetric. Samples are machined to fill the entire cross-sectional area of the test fixture (figure 2.2a) for the length of the sample and are press fit into the coaxial test fixture of figure 1.1, minimizing the potential for discontinuities and higher-order mode excitation.

Repeated mounting of a single sample, imprecise machining, or malleable material may unintentionally introduce discontinuities between the sample and test fixture conductors. Each time a material is mounted, some of the outer and inner surface is removed. Optimally, the amount of material removed is kept to a minimum by careful alignment of the sample during mounting. Precision machining is necessary, but difficult and potentially expensive. Unintentional discontinuities are usually small in scale and can be compensated for with conducting pastes between the material and conductor [15], but risk contaminating the sample.

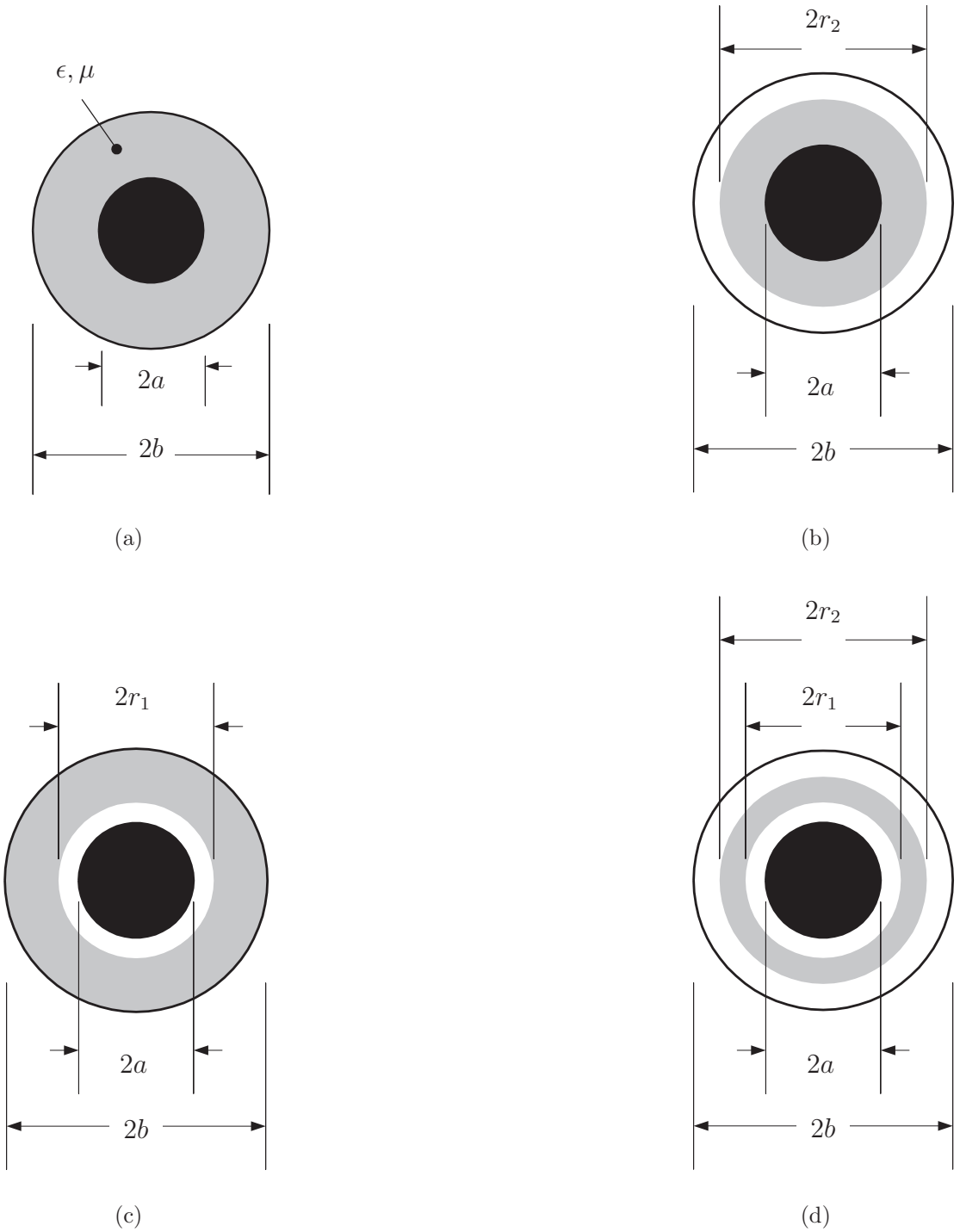

Figure 2.2: A sample that uniformly fills the cross-sectional area of the coaxial test fixture, shown in (a), is the ideal test scenario. Machining imperfections or temperature changes during measurement can introduce air gaps between the outer coaxial conductor and the outer radius of the sample (b) or between the inner conductor and the inner radius of the sample (c). A two air gap generalization (d) could be used for analysis, but physically would not remain axially symmetric. Scenarios (b) and (c) are addressed in this research.

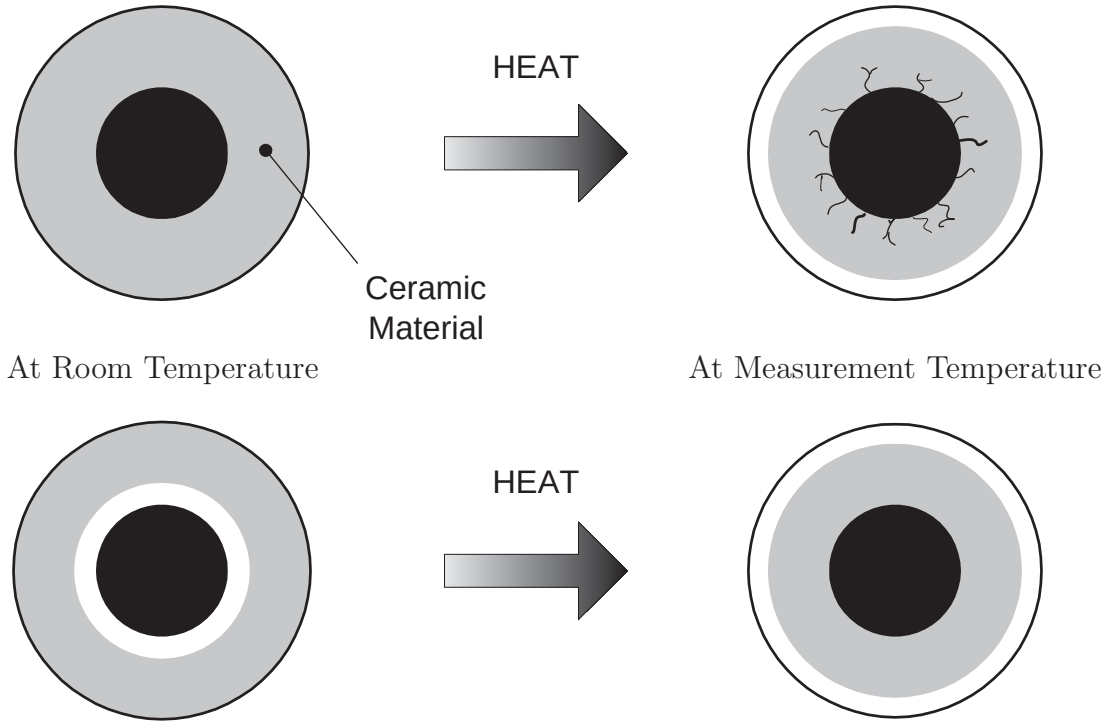

Figure 2.3: High temperature measurements of ceramic materials may crack the material if the inner conductor expands faster than the material as temperature increases (upper). Machining in an inner air gap (lower left) ensures the sample is undamaged at measurement temperature, but also introduces an outer air gap (lower right) and consequently error in the measurement.

Test profiles may require that relatively large gaps be machined into the material prior to measurement. For example, measuring a ceramic material at high temperature requires the sample be machined with an inner air gap at room temperature (figure 2.3). The mismatch in thermal expansion rates between the sample and the conductor may crack or otherwise damage the material at measurement temperature. If the test profile calls for measurements at high temperatures, a sample may require an inner air gap at room temperature that is filled in as the coax center conductor expands with increase in temperature (assuming a mismatch in the thermal expansion coefficients between the coax metal and the sample). Obviously, as temperature increases the outer conductor is also expanding away from the outer material face leaving an unavoidable outer air gap.

The results from measurements of two different materials are presented as an example of the impact of air gaps. Both materials are assumed to be a simple media (i.e. linear, isotropic, and homogeneous). The first material is Rexolite®, a non-magnetic, lossless dielectric material with a relative permittivity of approximately 2.525 over the measurement frequency band. Three samples were used:

1. Fully-Filled: the sample fully-fills the cross-sectional area of the coaxial waveguide between the inner and outer conductor. The sample was press-fitted dry into the sample holder shown in figure 1.1. Measurements from this sample are assumed to be representative of the true properties of the material given the test setup used.
2. 100 mil Outer Gap: the sample was machined to have a 100 mil radial air gap between the outer conductor and the material. The sample was press-fitted dry onto the inner conductor. The air gap is $\approx 30\%$ of the cross-sectional area in the coax test fixture between the inner and outer conductor.
3. 100 mil Inner Gap: the sample was machined to have a 100 mil radial air gap between the inner conductor and the material. The sample was press-fitted dry into the outer conductor. The air gap is $\approx 17\%$ of the cross-sectional area in the coax test fixture between the inner and outer conductor.

Each sample was 1 in. in length.

The second material is Magnetic Radar Absorbing Material (MagRAM), a high dielectric constant, lossy, magnetic material. It is designed for applications requiring significant attenuation of electric and magnetic fields. The permittivity and permeability of the MagRAM vary with frequency and are shown in subsequent figures as the fully filled result. Three MagRAM samples were used and are identical in description to the Rexolite® samples except for their radial and length measurements. One MagRAM sample fully filled the cross-section of the coaxial test fixture, while the other two samples had 9 mil inner and outer air gaps. The 9 mil outer air gap is 3% of the cross sectional area of the coaxial test fixture between the inner and outer

conductor. The 9 mil inner air gap is 1.3%. The MagRAM sample lengths for the fully filled, outer and inner gap are 173.4 mil, 150 mil and 179 mil respectively. The MagRAM samples were cut from sheets of the material with care taken to minimize variations in the material composition (i.e. cutting samples in the same general area of the sheet).

The impact of air gaps on the permittivity measurements follows physical intuition. The permittivity measurements for Rexolite® are shown in figure 2.4. As evident in (a), introducing an air gap in the measurement is equivalent to "mixing" air with the material to be measured. Therefore, the real permittivity is expected to decrease, approaching that of freespace (ϵ_0, μ_0) for large gaps. The measurements validate this expectation. The imaginary permittivity is expected to remain constant (the material and freespace are both very low loss). The NRW algorithm results do not validate this expectation. The coupling of power into higher order evanescent modes represents a "loss" in system power as measured at the NWA. The NRW algorithm expects that the NWA measurements (S_{11} and S_{21}) are representative of the sample permittivity and permeability and therefore misreports the sample as lossy. In neglecting the higher order mode excitation, the NRW algorithm is accurately reporting a property of the system, but not of the material being measured. Similar results are noted for the MagRAM material shown in figure 2.5.

The location of the air gap impacts the degree of error in the measurement. The electric field is concentrated around the center conductor of the coaxial line. To measure the effect of the electric and magnetic field on a material (permittivity and permeability), the material is optimally exposed to the field strengths of each field. For inner air gaps, the freespace region is exposed to the peak field strengths. Therefore, a greater error is expected when an air gap exists around the inner conductor versus an equivalent width air gap around the outer conductor. The measurements shown in figure 2.4 and 2.5 match this expectation.

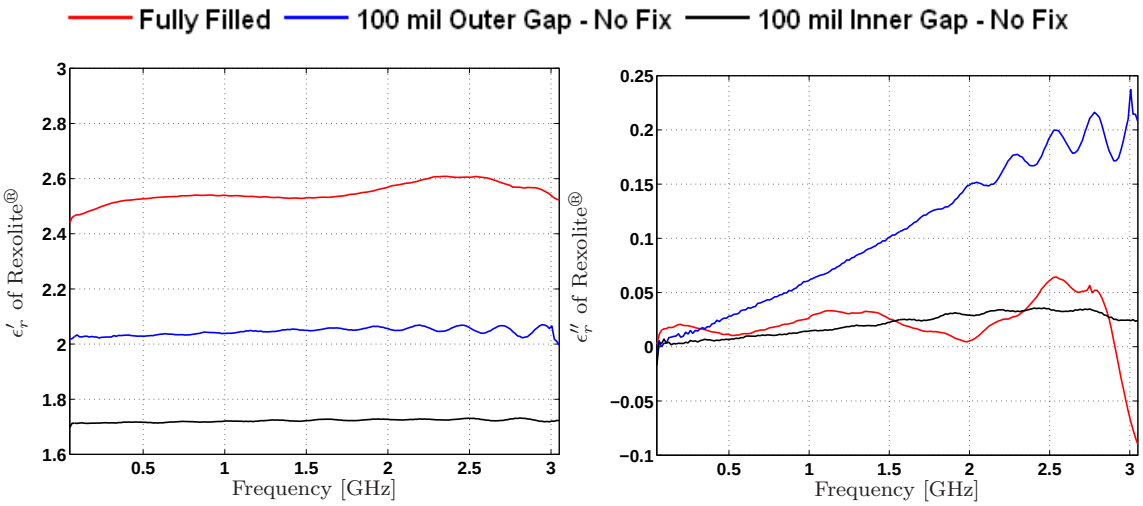

(a) (b)

Figure 2.4: Measured permittivity is shown as $\epsilon_r = \epsilon_r' - j\epsilon_r''$. Rexolite® is a non-magnetic, lossless dielectric ($\epsilon_r \approx 2.525$). The real part of the permittivity (a) decreases toward that of freespace when an air gap is introduced. Additionally, the imaginary part of the permittivity (b) indicates more loss when higher order modes are excited, but not accounted for. The concentration of the electric field around the center gives rise to more error if an air gap exists around the inner conductor.

2.4 Air Gap Correction

Frequency independent permittivity and permeability corrections for coaxial line measurements where an air gap exists in the sample region are available from the National Institute of Standards and Technology (NIST) [2]. The corrections assume that the fields in the sample region are TEM. The sample with air gap is then modelled independently as a layered capacitor and a series inductor where the singely directed components of the electric, E_ρ, and magnetic, H_ϕ, fields are applied across the lumped circuit components. As an example, using the generalized case of 2.2(d), the total capacitance of the sample with air gaps is equivalent to a layered or series capacitor and is given by

$$\frac{1}{C_{\text{total}}} = \frac{1}{C_{\text{outer air gap}}} + \frac{1}{C_{\text{sample}}} + \frac{1}{C_{\text{inner air gap}}} \tag{2.1}$$

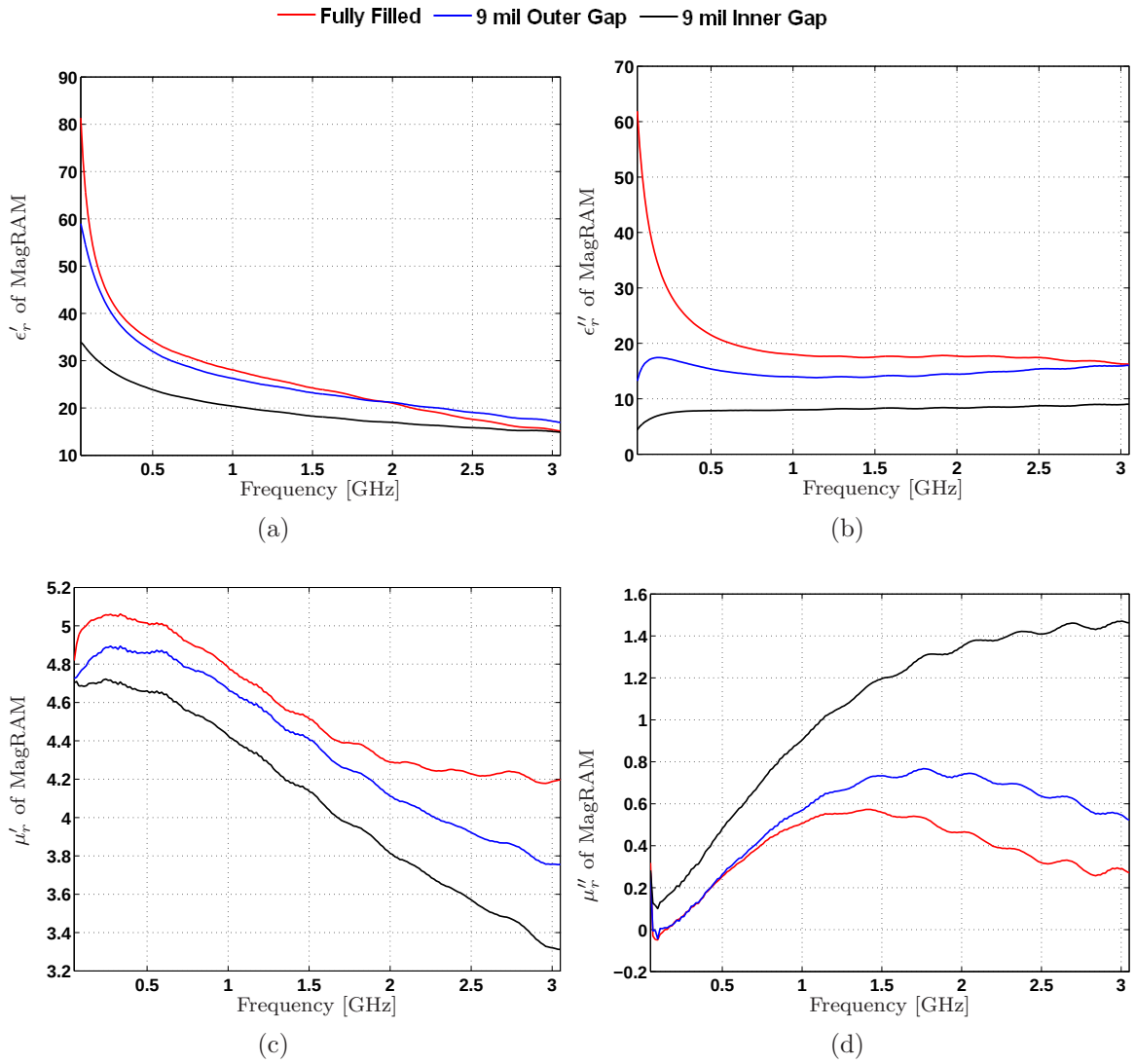

Figure 2.5: Measured permittivity and permeability of MagRAM are shown as $\epsilon_r = \epsilon_r' - j\epsilon_r''$ and $\mu_r = \mu_r' - j\mu_r''$, respectively. Even small air gaps have a significant impact on the measurement of highly load materials. The exact effects are as noted before, a decrease in measured real permittivity and permeability toward that of freespace and an increase in imaginary part of both the permittivity and permeability due to unaccounted for power coupled into higher order evanescent modes.

Knowing that capacitance is the ratio of charge to potential, the capacitance of each individual layer is equivalent to [6]

$$\begin{aligned} C &= \frac{Q}{V} \\ &= \frac{\epsilon \oint\limits_{S} \hat{\rho} \cdot \hat{\rho} E_\rho \, dl}{\int\limits_{\rho_1}^{\rho_2} \hat{\rho} E_\rho \cdot dl} L \end{aligned}$$

where surface S is the cross sectional area of the layer, ρ_1 and ρ_2 are the inner and outer radius of the layer respectively, ϵ is the permittivity of the layer, L is the length of the sample, and $\hat{\rho} E_\rho$ is the $\hat{\rho}$ directed electric field for a TEM excitation or

$$\hat{\rho} E_\rho = \frac{E_0}{\rho} \hat{\rho}$$

Solving C in a radial layer produces

$$\begin{aligned} C &= \frac{\epsilon \int\limits_{0}^{2\pi} E_\rho \rho d\phi}{\int\limits_{\rho_1}^{\rho_2} E_\rho d\rho} \\ &= \frac{\epsilon 2\pi L}{\ln\left(\frac{\rho_2}{\rho_1}\right)} \end{aligned}$$

which can be calculated for each layer and substituted into (2.1) to produce simple, analytical correction factors for the real and imaginary parts of the permittivity calculated via the NRW algorithm. An identical process is accomplished for the series inductance and results in a correction factor for the permeability. The corrections

are [2]

$$\begin{aligned}
\epsilon'_{cR} &= \frac{L_2\left[\epsilon'_{mR}L_3 - (\epsilon''_{mR})^2 L_1 - (\epsilon'_{mR})^2 L_1\right]}{(\epsilon'_{mR}L_1)^2 - 2\epsilon'_{mR}L_1L_3 + (\epsilon''_{mR}L_1)^2 + L_3^2} \\
\epsilon''_{cR} &= \frac{L_2L_3\epsilon''_{mR}}{(\epsilon'_{mR}L_1)^2 - 2\epsilon'_{mR}L_1L_3 + (\epsilon''_{mR}L_1)^2 + L_3^2} \\
\mu'_{cR} &= \frac{\mu'_{cR}L_3 - L_1}{L_2} \\
\mu''_{cR} &= \mu''_{cR}\frac{L_3}{L_2}
\end{aligned}$$

where $\epsilon'_{mR} - j\epsilon''_{mR}$ and $\mu'_{mR} - j\mu''_{mR}$ are the relative permittivity and permeability calculated from measurements, $\epsilon'_{cR} - j\epsilon''_{cR}$ and $\mu'_{cR} - j\mu''_{cR}$ are the corrected relative permittivity and permeability, and using dimensions from figures 2.2b and 2.2c

$$L_1 = \ln\left(\frac{r_1}{a}\right) + \ln\left(\frac{b}{r_2}\right) \qquad L_2 = \ln\left(\frac{r_2}{r_1}\right) \qquad L_3 = \ln\left(\frac{b}{a}\right)$$

The correction factors are very simple to apply to measured data and require only knowledge of the radii of the coaxial line and sample.

In 1994, NIST enlisted eleven organizations to independently measure five unique, low-loss material samples of known permittivity to compare each organizations method of air gap error correction[2]. The real part of the permittivity, $\epsilon_r\,'$, for the five materials was on the order of 10 with one notable exception of $\epsilon_r\,' = 50$ (Barium titanate ceramic). Based on participant measurements, the samples had inner and outer air gaps on the order of 1 mil so that the air gap accounted for 2.5% of the cross sectional area of the coaxial line while the sample filled the remaining 97.5%. Participants used one of three means to calculate the material permitttivity: the NRW algorithm with no corrections, the NRW algorithm with the NIST correction and other undisclosed (assumed proprietary) techniques. The results, published in [15], show most measurements agreeing within 10%, although a great deal of frequency dependent error

[2]Measurements were taken at room temperature and the use of conductive pastes, mentioned previously, was forbidden.

is noted in the high permittivity material. The authors concluded that "accurate knowledge of the air-gap dimensions is fundamental to the proper determination of material characteristics using the T/R method."

The NIST correction factors were applied to the Rexolite® and MagRAM measurements to judge their effectiveness on the materials used for this research. The resulting corrected measurements are shown in figures 2.6 and 2.7 respectively.

Corrected ϵ_r' values for both the Rexolite® and MagRAM are reasonably accurate. Figure 2.8 provides more detail of the MagRAM ϵ_r' corrections at 2 GHz and showing a general trend toward the vicinity of the actual value despite the large discrepancy in low frequency corrected values. In the case of MagRAM, μ_r' is undercorrected, but the correction is toward the actual value of μ_r' and maintains the same general slope over a change in frequency.

The corrected imaginary material parameters do not give a good understanding of the behavior of each material. For Rexolite®, the corrected ϵ_r'' is diverging from the actual material parameters. For MagRAM, both the corrected ϵ_r'' and μ_r'' are diverging from the actual value. These results are expected since higher order evanescent fields are not being accounted for in either the NRW algorithm or the NIST correction.

Herein lies the difficulty in applying the correction factor. For both the low and high permittivity materials, the amount of correction is fixed. Although a sensitivity analysis may lend confidence to the final result, no physical insight is readily available from the correction factor. One of the acknowledged shortcomings of the layered capacitor model is the assumption of a single-propagating mode and that the fields internal to the material region are TEM. It is already proven that higher order modes will be excited when an air gap discontinuity is present. It is now necessary to define the fields within the material region to determine how close they are to TEM.

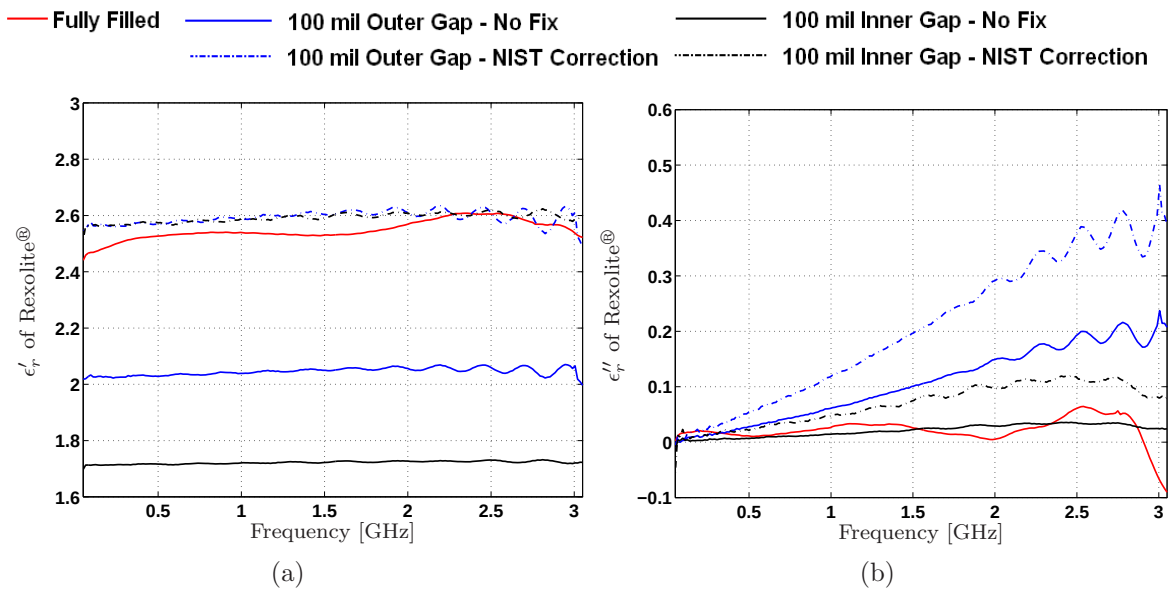

Figure 2.6: Measured permittivity is shown as $\epsilon_r = \epsilon_r' - j\epsilon_r''$. Rexolite® is a non-magnetic, lossless dielectric ($\epsilon_r \approx 2.525$). The NIST correction performs very well for the ϵ_r' (a), but ϵ_r'' is over-corrected (b).

2.5 Fields in Region with Sample and Air Gap

Air gaps between the sample and the outer or inner conductor of the coaxial test fixture eliminate the possibility of a TEM field within the material. Considering a $\hat{z}$-directed field as in figure 2.9, the phase front must propagate uniformly through the air gap and material so that fields at the material to air gap interface are continuous, or, mathematically, independent of z. For the $\hat{z}$-directed phase front to remain continuous across the radial boundary

$$e^{-jk_z^0 z} = e^{-jk_z^s z} \tag{2.2}$$

must be true, where k_z^0 and k_z^s are the $\hat{z}$-directed wave numbers of free space and the sample respectively. The cutoff wave number of a TEM field is $k_c = k_{rho} = 0$ (see appendix C). Therefore, for a TEM mode to propagate in the sample, the constraint equations for the air gap and sample

$$\begin{aligned} \left(k_\rho^0\right)^2 + \left(k_z^0\right)^2 &= k_0^2 \\ \left(k_\rho^s\right)^2 + \left(k_z^s\right)^2 &= k_s^2 \end{aligned}$$

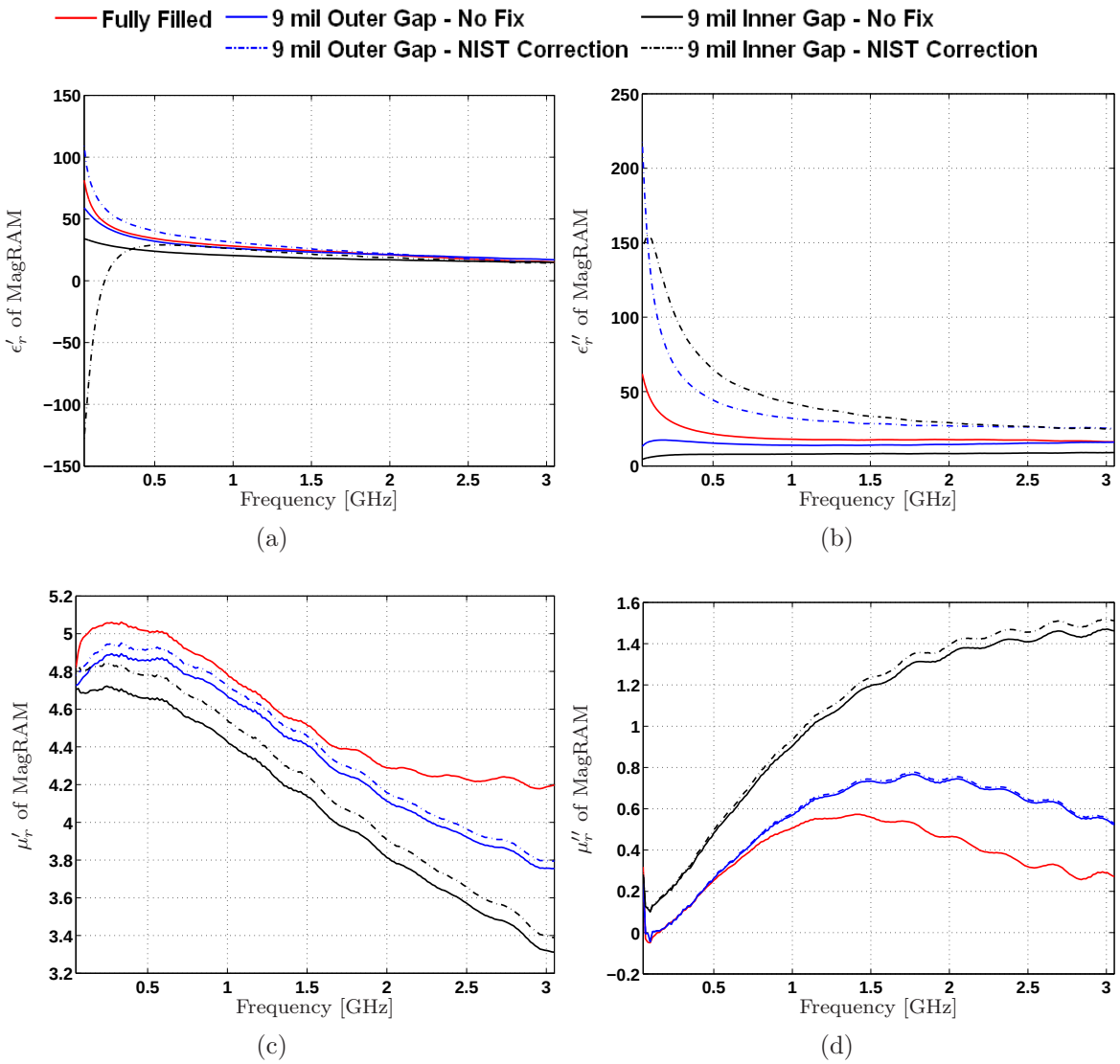

Figure 2.7: Measured permittivity and permeability of MagRAM are shown as $\epsilon_r = \epsilon_r' - j\epsilon_r''$ and $\mu_r = \mu_r' - j\mu_r''$, repectively. The NIST Correction of ϵ_r' appears to approach the actual value for higher frequencies, but does not perform well at lower frequencies. The corrections to values of μ_r' approach the actual value, but are not significant enough. Both ϵ_r'' and μ_r'' are biased higher, again indicating a misreporting of material loss properties.

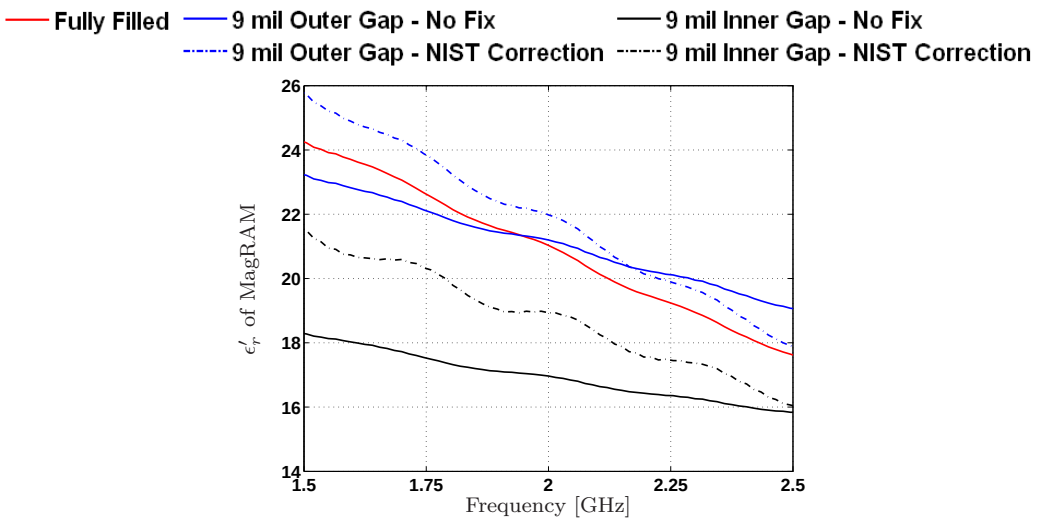

Figure 2.8: In figure 2.7(a) the corrected ϵ_r' of MagRAM appears to approach the actual value. Zooming in at 2 GHz shows that, while realtive close, the corrected values for both inner and outer gap are approximately correct and nearly follow the slope of the actual value.

are reduced to

$$\begin{aligned} k_z^0 &= k_0 \\ k_z^s &= k_s \end{aligned}$$

The consequence for (2.2) is

$$e^{-jk_0 z} = e^{-jk_s z} \tag{2.3}$$

must hold for a uniform phase front. Of course, $k_0 = \omega\sqrt{\epsilon_0\mu_0}$ will not equal $k_s = \omega\sqrt{\epsilon_s\mu_s}$ and therefore a TEM mode cannot exist.

Furthermore, two assumptions regarding the final field equations are made to match the physical expectation of the system. First, the higher order modes excited by the air gaps in Region II will tend to match the symmetry of the air gaps. Provided the material in Region II is axially symmetric, only axially symmetric higher order modes are expected.

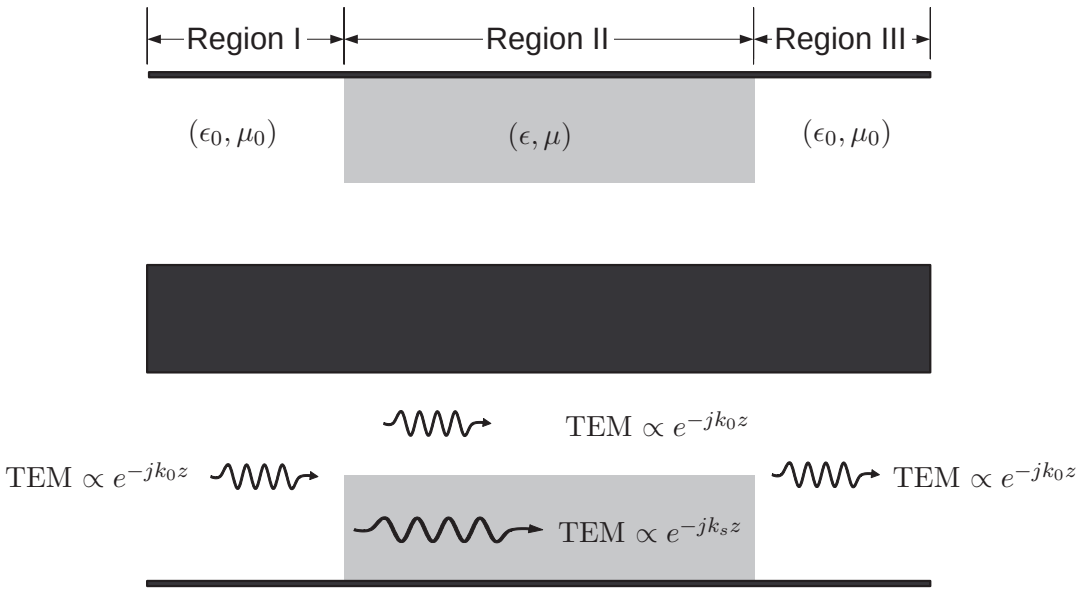

Figure 2.9: Considering only a forward propagating TEM excitation and ignoring any reflections, the fields in Region II must be continuous across the radial material-air gap boundary. Since $e^{-jk_0 z} \neq e^{-jk_s z}$, a propagating TEM field in Region II is not physically possible.

Second, TE modes will not be excited within Region II. The fields of the TEM excitation are (see appendix F)

$$E_\rho = \Upsilon \left[\frac{1}{\rho}\right] e^{-jkz} \tag{2.4}$$

$$H_\phi = \frac{\Upsilon}{Z_{TEM}} \left[\frac{1}{\rho}\right] e^{-jkz} \tag{2.5}$$

where Υ is a constant with respect to frequency and the material parameters. Axially symmetric TE fields in general are

$$E_\rho = E_z = H_\phi = 0 \qquad E_\phi \neq 0,\ H_\rho \neq 0,\ H_z \neq 0$$

For a TE field to be excited, the incident TEM field components must excite orthogonal fields (i.e. E_ρ^{TEM} must excite E_ϕ^{TE}). Using the previous assumption of an isotropic media, this type of excitation is not possible.

Axially symmetric TM field equations within the sample and within the air gap of Region II must independently satisfy the wave equation, constraint equation, and applicable boundary conditions. The TM field equations derived in appendix F are axially symmetric for $m = 0$ and will satisfy these conditions, but the fields within the material region and the air gap region will be unique such that (considering only forward propagating fields)

$$E_\rho = \begin{cases} \frac{k_{\rho 1_n}\tilde{\gamma}_n}{j\omega\mu_1\epsilon_1}\left[A^+_{1,0n}J_1\left(k_{\rho 1_n}\rho\right) + B^+_{1,0n}Y_1\left(k_{\rho 1_n}\rho\right)\right]e^{-\tilde{\gamma}_n z} & \ldots \quad a < \rho < R \\ \\ \frac{k_{\rho 2_n}\tilde{\gamma}_n}{j\omega\mu_2\epsilon_2}\left[A^+_{2,0n}J_1\left(k_{\rho 2_n}\rho\right) + B^+_{2,0n}Y_1\left(k_{\rho 2_n}\rho\right)\right]e^{-\tilde{\gamma}_n z} & \ldots \quad R < \rho < b \end{cases}$$

$$H_\phi = \begin{cases} \frac{k_{\rho 1_n}}{\mu_1}\left[A^+_{1,0n}J_1\left(k_{\rho 1_n}\rho\right) + B^+_{1,0n}Y_1\left(k_{\rho 1_n}\rho\right)\right]e^{-\tilde{\gamma}_n z} & \ldots \quad a < \rho < R \\ \\ \frac{k_{\rho 2_n}}{\mu_2}\left[A^+_{2,0n}J_1\left(k_{\rho 2_n}\rho\right) + B^+_{2,0n}Y_1\left(k_{\rho 2_n}\rho\right)\right]e^{-\tilde{\gamma}_n z} & \ldots \quad R < \rho < b \end{cases}$$

$$E_z = \begin{cases} \frac{k^2_{\rho 1_n}}{j\omega\mu_1\epsilon_1}\left[A^+_{1,0n}J_0\left(k_{\rho 1_n}\rho\right) + B^+_{1,0n}Y_0\left(k_{\rho 1_n}\rho\right)\right]e^{-\tilde{\gamma}_n z} & \ldots \quad a < \rho < R \\ \\ \frac{k^2_{\rho 2_n}}{j\omega\mu_2\epsilon_2}\left[A^+_{2,0n}J_0\left(k_{\rho 2_n}\rho\right) + B^+_{2,0n}Y_0\left(k_{\rho 2_n}\rho\right)\right]e^{-\tilde{\gamma}_n z} & \ldots \quad R < \rho < b \end{cases}$$

where $\tilde{\gamma}_n = jk_z$ for mode n, A and B are constants where the subscripts indicate the mode and region where the constants are defined, and for each gap scenario

Outer Air Gap	Inner Air Gap
$R = r_2$	$R = r_1$
ϵ_1, μ_1 are sample properties	ϵ_1, μ_1 are ϵ_0, μ_0
ϵ_2, μ_2 are ϵ_0, μ_0	ϵ_2, μ_2 are sample properties
figure 2.2(b)	figure 2.2(c)

Boundary conditions at the inner and outer conductors require the tangential electric field at the surface to be zero

$$E_z(\rho = a, \phi, z) = E_z(\rho = a, \phi, z) = 0$$

which are applied to solve for constants A and B

$$A^+_{1,0n} = -B^+_{1,0n}\frac{Y_0\left(k_{\rho 1_n}a\right)}{J_0\left(k_{\rho 1_n}a\right)} \qquad A^+_{2,0n} = -B^+_{2,0n}\frac{Y_0\left(k_{\rho 2_n}b\right)}{J_0\left(k_{\rho 2_n}b\right)} \tag{2.6}$$

Substituting this result into the field equations produces

$$E_\rho = \begin{cases} \tilde{B}^+_{1,0n}\left[J_1\left(k_{\rho 1_n}\rho\right)Y_0\left(k_{\rho 1_n}a\right) - J_0\left(k_{\rho 1_n}a\right)Y_1\left(k_{\rho 1_n}\rho\right)\right]e^{-\tilde{\gamma}_n z} & \ldots \quad a < \rho < R \\ \tilde{B}^+_{2,0n}\left[J_1\left(k_{\rho 2_n}\rho\right)Y_0\left(k_{\rho 2_n}b\right) - J_0\left(k_{\rho 2_n}b\right)Y_1\left(k_{\rho 2_n}\rho\right)\right]e^{-\tilde{\gamma}_n z} & \ldots \quad R < \rho < b \end{cases}$$

$$H_\phi = \begin{cases} \dfrac{\tilde{B}^+_{1,0n}}{Z_{\mathrm{TM}_{1n}}}\left[J_1\left(k_{\rho 1_n}\rho\right)Y_0\left(k_{\rho 1_n}a\right) - J_0\left(k_{\rho 1_n}a\right)Y_1\left(k_{\rho 1_n}\rho\right)\right]e^{-\tilde{\gamma}_n z} & \ldots \quad a < \rho < R \\ \dfrac{\tilde{B}^+_{2,0n}}{Z_{\mathrm{TM}_{2n}}}\left[J_1\left(k_{\rho 2_n}\rho\right)Y_0\left(k_{\rho 2_n}b\right) - J_0\left(k_{\rho 2_n}b\right)Y_1\left(k_{\rho 2_n}\rho\right)\right]e^{-\tilde{\gamma}_n z} & \ldots \quad R < \rho < b \end{cases}$$

$$E_z = \begin{cases} \dfrac{k_{\rho 1_n}\tilde{B}^+_{1,0n}}{\tilde{\gamma}_n}\left[J_0\left(k_{\rho 1_n}\rho\right)Y_0\left(k_{\rho 1_n}a\right) - J_0\left(k_{\rho 1_n}a\right)Y_0\left(k_{\rho 1_n}\rho\right)\right]e^{-\tilde{\gamma}_n z} & \ldots \quad a < \rho < R \\ \dfrac{k_{\rho 2_n}\tilde{B}^+_{2,0n}}{\tilde{\gamma}_n}\left[J_0\left(k_{\rho 2_n}\rho\right)Y_0\left(k_{\rho 2_n}b\right) - J_0\left(k_{\rho 2_n}b\right)Y_0\left(k_{\rho 2_n}\rho\right)\right]e^{-\tilde{\gamma}_n z} & \ldots \quad R < \rho < b \end{cases}$$

where

$$\tilde{B}^{+}_{1,0n} = \frac{-k_{\rho 1_n}\tilde{\gamma}_n B^{+}_{1,0n}}{j\omega\mu_1\epsilon_1 J_0\left(k_{\rho 1_n}a\right)} \qquad \tilde{B}^{+}_{2,0n} = \frac{-k_{\rho 2_n}\tilde{\gamma}_n B^{+}_{2,0n}}{j\omega\mu_2\epsilon_2 J_0\left(k_{\rho 2_n}b\right)}$$

$$Z_{\mathrm{TM}_{1n}} = \frac{\tilde{\gamma}_n}{j\omega\epsilon_1} \qquad Z_{\mathrm{TM}_{2n}} = \frac{\tilde{\gamma}_n}{j\omega\epsilon_2}$$

The final boundary condition to satisfy requires the tangential fields to be continuous across the material to air gap interface or

$$\begin{aligned} H_\phi(R^{-}) &= H_\phi(R^{+}) \\ E_z(R^{-}) &= E_z(R^{+}) \end{aligned}$$

Applying these conditions produces two separate equations for the constant $\tilde{B}^{+}_{2,0n}$

$$\begin{aligned} \tilde{B}^{+}_{2,0n} &= \tilde{B}^{+}_{1,0n}\frac{Z_{\mathrm{TM}_{2n}}}{Z_{\mathrm{TM}_{1n}}}\frac{\left[J_1\left(k_{\rho 1_n}R\right)Y_0\left(k_{\rho 1_n}a\right) - J_0\left(k_{\rho 1_n}a\right)Y_1\left(k_{\rho 1_n}R\right)\right]}{\left[J_1\left(k_{\rho 2_n}R\right)Y_0\left(k_{\rho 2_n}b\right) - J_0\left(k_{\rho 2_n}b\right)Y_1\left(k_{\rho 2_n}R\right)\right]} \\ \tilde{B}^{+}_{2,0n} &= \tilde{B}^{+}_{1,0n}\frac{k_{\rho 1_n}}{k_{\rho 2_n}}\frac{\left[J_0\left(k_{\rho 1_n}R\right)Y_0\left(k_{\rho 1_n}a\right) - J_0\left(k_{\rho 1_n}a\right)Y_0\left(k_{\rho 1_n}R\right)\right]}{\left[J_0\left(k_{\rho 2_n}R\right)Y_0\left(k_{\rho 2_n}b\right) - J_0\left(k_{\rho 2_n}b\right)Y_0\left(k_{\rho 2_n}R\right)\right]} \end{aligned}$$

which are equated to produce the characteristic equation for $\tilde{\gamma}_n$,

$$\begin{aligned} k_{\rho 1_n} Z_{\mathrm{TM}_{1n}} &\left[J_0\left(k_{\rho 1_n}R\right)Y_0\left(k_{\rho 1_n}a\right) - J_0\left(k_{\rho 1_n}a\right)Y_0\left(k_{\rho 1_n}R\right)\right] \\ &\left[J_1\left(k_{\rho 2_n}R\right)Y_0\left(k_{\rho 2_n}b\right) - J_0\left(k_{\rho 2_n}b\right)Y_1\left(k_{\rho 2_n}R\right)\right] - \\ k_{\rho 2_n} Z_{\mathrm{TM}_{2n}} &\left[J_0\left(k_{\rho 2_n}R\right)Y_0\left(k_{\rho 2_n}b\right) - J_0\left(k_{\rho 2_n}b\right)Y_0\left(k_{\rho 2_n}R\right)\right] \\ &\left[J_1\left(k_{\rho 1_n}R\right)Y_0\left(k_{\rho 1_n}a\right) - J_0\left(k_{\rho 1_n}a\right)Y_1\left(k_{\rho 1_n}R\right)\right] = 0 \end{aligned} \quad (2.7)$$

where

$$k_{\rho 1_n} = \tilde{\gamma}_n^2 + \omega^2\epsilon_1\mu_1 \quad \text{and} \quad k_{\rho 2_n} = \tilde{\gamma}_n^2 + \omega^2\epsilon_2\mu_2$$

Using (2.7), the first 5 mode wavenumbers at 2 GHz in a test fixture with a Rexolite® sample and 100 mil inner and outer air gap are calculated and for MagRAM with a 9 mil inner and outer air gap and compared to wavenumbers in the fully filled case.

The results are reported in table 2.2 and 2.3. It is immediately evident that the propagating TEM field corresponds to a propagating, axially symmetric TM_{00} field in both materials.

The NIST correction factors rely on the similarity of the transverse field components of the TEM and TM_{00} fields. Recall that the correction factors are based on the material modelled as a lumped capacitor and inductor with a TEM field. The capacitance and inductance per unit length are defined as

$$C = \frac{\epsilon \int_0^{2\pi} E_\rho \rho d\phi}{\int_{\rho_1}^{\rho_2} E_\rho d\rho} \qquad L = \frac{\mu \int_{\rho_1}^{\rho_2} H_\phi d\rho}{\int_0^{2\pi} H_\phi \rho d\phi} \tag{2.8}$$

respectively. The final form of the correction factors completes the integration assuming the transverse field components behave in a $\frac{1}{\rho}$ fashion, the expected behavior for a TEM field. If the TM_{00} field components within the material and air gap region do not follow the $\frac{1}{\rho}$ behavior, the accuracy of the correction factors will be compromised.

The TM_{00} field components for a Rexolite® sample with an 100 mil inner and outer air gap are plotted against their respective TEM field components in figure 2.10. The H_ϕ component is continuous across the air gap to material boundary as required by the tangential boundary conditions at the material to air gap interface. The E_z field component is non-zero as expected for a TM^z field. A discontinuity equal to the magnitude of the permittivity exists in E_ρ for both gap scenarios. This is expected from the constitutive relationship for a simple media which state

$$\begin{aligned} \hat{\rho} \cdot \mathbf{D}^{\text{ air}} &= \hat{\rho} \cdot \mathbf{D}^{\text{ sample}} \\ \epsilon_0 E_\rho^{\text{ air}} &= \epsilon E_\rho^{\text{ sample}} \\ E_\rho^{\text{ air}} &= \epsilon_r E_\rho^{\text{ sample}} \end{aligned}$$

It is this discontinuity that (2.1) is accounting for. For both gap scenarios, the fields within both the air and material exhibit a near $\frac{1}{\rho}$ behavior. This fact is exploited

by the NIST correction factor and justifies the excellent corrected ϵ_r' values shown in figure 2.6(a). Again, correction to ϵ_r'', shown in figure 2.6(b), is based on the same TEM assumption, not accounting for the loss of power due to higher mode excitation, and therefore is not expected to be as accurate as the correction to ϵ_r'.

The TM_{00} field components for a MagRAM sample with an 9 mil inner and outer air gap are plotted against their respective TEM field components in figure 2.11. The properties of the fields with respect to an E_ρ discontinuity, E_z presence, and H_ϕ continuity at the material to air gap boundary remain the same as the Rexolite® case. The field profiles though do not exhibit a $\frac{1}{\rho}$ behavior. This violates the expected $\frac{1}{\rho}$ behavior and mathematically increases the complexity of the integrations in (2.8). The performance of the correction factors is reduced as shown in figure 2.7 (zoomed in figure 2.8 for the real permittivity). The imaginary part, for both permittivity and permeability, are over corrected again due to power lost to higher mode excitation.

2.6 Summary

Correction factors derived by modelling a sample plus axially symmetric air gap as a lumped capacitor and inductor model perform well when the assumptions regarding the model are met. It was shown that for a low loss dielectric material, the assumption of a TEM-like field within the sample region with air gap is valid and produces excellent results for the real permittivity. For heavily loaded, magnetic samples the fields within the material region with air gap appear less TEM-like and therefore the correction to the real permittivity and real permeability are less accurate. In both material cases, corrections to the imaginary part of the permittivity and permeability are hampered by not accounting for power coupling into excited higher order evanescent modes.

Table 2.2: Comparison of Wavenumbers in Rexolite® when inner and outer air gaps are present. For $\tilde{\gamma}$ the frequency is 2 GHz.

Rexolite® Filled Coax				100 mil Outer Air Gap			
Mode	γ	k_ρ		Mode	$\tilde{\gamma}$	k_ρ	k_ρ^0
TEM	0.0+66.6j	0.0+0.0j	$\Rightarrow$	TM_{01}	0.0+59.5j	29.9+0.0j	0.0+42.3j
TM_{01}	277.9	285.7	$\Rightarrow$	TM_{02}	232.4	241.8	236.2
TM_{02}	571.1	575.0	$\Rightarrow$	TM_{03}	561.0	564.9	562.5
TM_{03}	861.0	863.5	$\Rightarrow$	TM_{04}	894.6	897.1	895.6
TM_{04}	1150.0	1151.9	$\Rightarrow$	TM_{05}	1171.3	1173.2	1172.0

Rexolite® Filled Coax				100 mil Inner Air Gap			
Mode	γ	k_ρ		Mode	$\tilde{\gamma}$	k_ρ	k_ρ^0
TEM	0.0+66.6j	0.0+0.0j	$\Rightarrow$	TM_{00}	0.0+54.8j	37.8+0.0j	0.0+35.4j
TM_{01}	277.9	285.7	$\Rightarrow$	TM_{01}	245.1	253.9	248.6
TM_{02}	571.1	575.0	$\Rightarrow$	TM_{02}	569.7	573.6	571.2
TM_{03}	861.0	863.5	$\Rightarrow$	TM_{03}	899.3	901.8	900.3
TM_{04}	1150.0	1151.9	$\Rightarrow$	TM_{04}	1171.5	1173.4	1172.3

Table 2.3: Comparison of Wavenumbers in MagRAM ($\epsilon_r = 21.03 - i(17.71)$, $\mu_r = 4.289 - i(0.4633)$) when inner and outer air gaps are present. For $\tilde{\gamma}$ the frequency is 2 GHz.

MagRAM Filled Coax				9 mil Outer Air Gap			
Mode	γ	k_ρ		Mode	$\tilde{\gamma}$	k_ρ	k_ρ^0
TEM	179.3+419.8j	0.0+0.0j	$\Rightarrow$	TM_{00}	183.4+403.4i	122.9-10.6i	184.3+401.6i
TM_{01}	224.3+335.7j	285.7+0.0j	$\Rightarrow$	TM_{01}	133.9+214.3i	364.0-128.0i	135.8+211.3i
TM_{02}	461.7+163.1j	575.0+0.0j	$\Rightarrow$	TM_{02}	347.6+197.9i	475.3-13.7i	349.5+196.9i
TM_{03}	781.6+96.3j	863.5-0.0j	$\Rightarrow$	TM_{03}	663.5+122.6i	754.5+8.0i	664.7+122.3i
TM_{04}	1089.8+69.1j	1151.9-0.0j	$\Rightarrow$	TM_{04}	973.0+86.0i	1040.9+8.0i	973.9+85.9i

MagRAM Filled Coax				9 mil Inner Air Gap			
Mode	γ	k_ρ		Mode	$\tilde{\gamma}$	k_ρ	k_ρ^0
TEM	179.3+419.8j	0.0+0.0j	$\Rightarrow$	TM_{00}	189.2+388.1i	171.4-10.8i	190.1+386.3i
TM_{01}	224.3+335.7j	285.7+0.0j	$\Rightarrow$	TM_{01}	114.7+210.6i	364.2-140.4i	116.5+207.3i
TM_{02}	461.7+163.1j	575.0+0.0j	$\Rightarrow$	TM_{02}	362.1+195.2i	487.0-9.5i	364.0+194.1i
TM_{03}	781.6+96.3j	863.5-0.0j	$\Rightarrow$	TM_{03}	673.1+120.3i	763.4+7.4i	674.4+120.1i
TM_{04}	1089.8+69.1j	1151.9-0.0j	$\Rightarrow$	TM_{04}	980.4+84.9i	1047.9+7.6i	981.3+84.8i

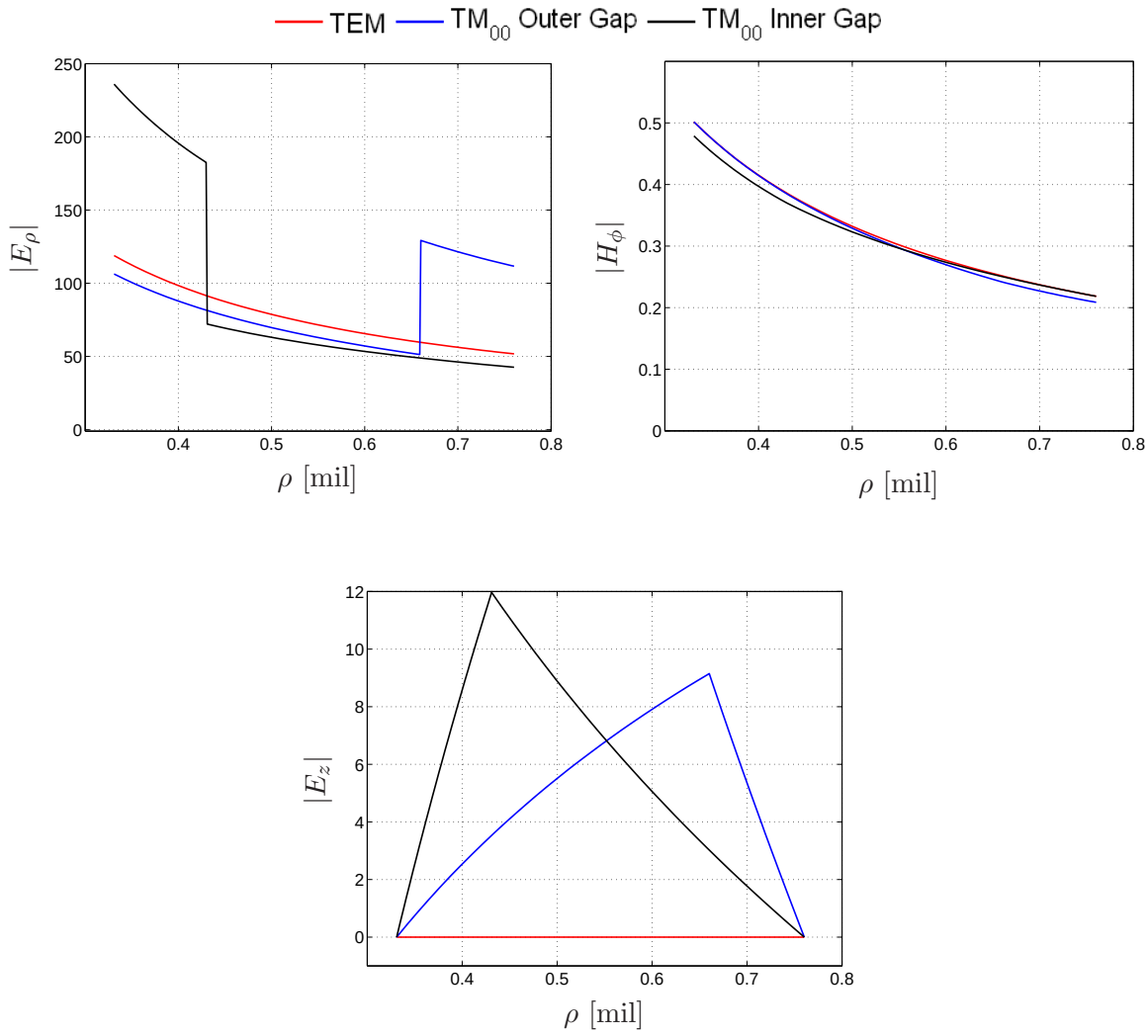

Figure 2.10: Fields at 2 GHz for a Rexolite® sample with a 100 mil air gap. The Rexolite® sample properties are $\epsilon_r = 2.525 - i(0.0)$ and $\mu_r = 1 - i(0.0)$. For the coaxial test fixture, the inner and outer conductor radii are 0.331 mil and 0.76025 mil respectively. The fields are normalized to a TEM electric field of $\frac{1}{\rho}$.

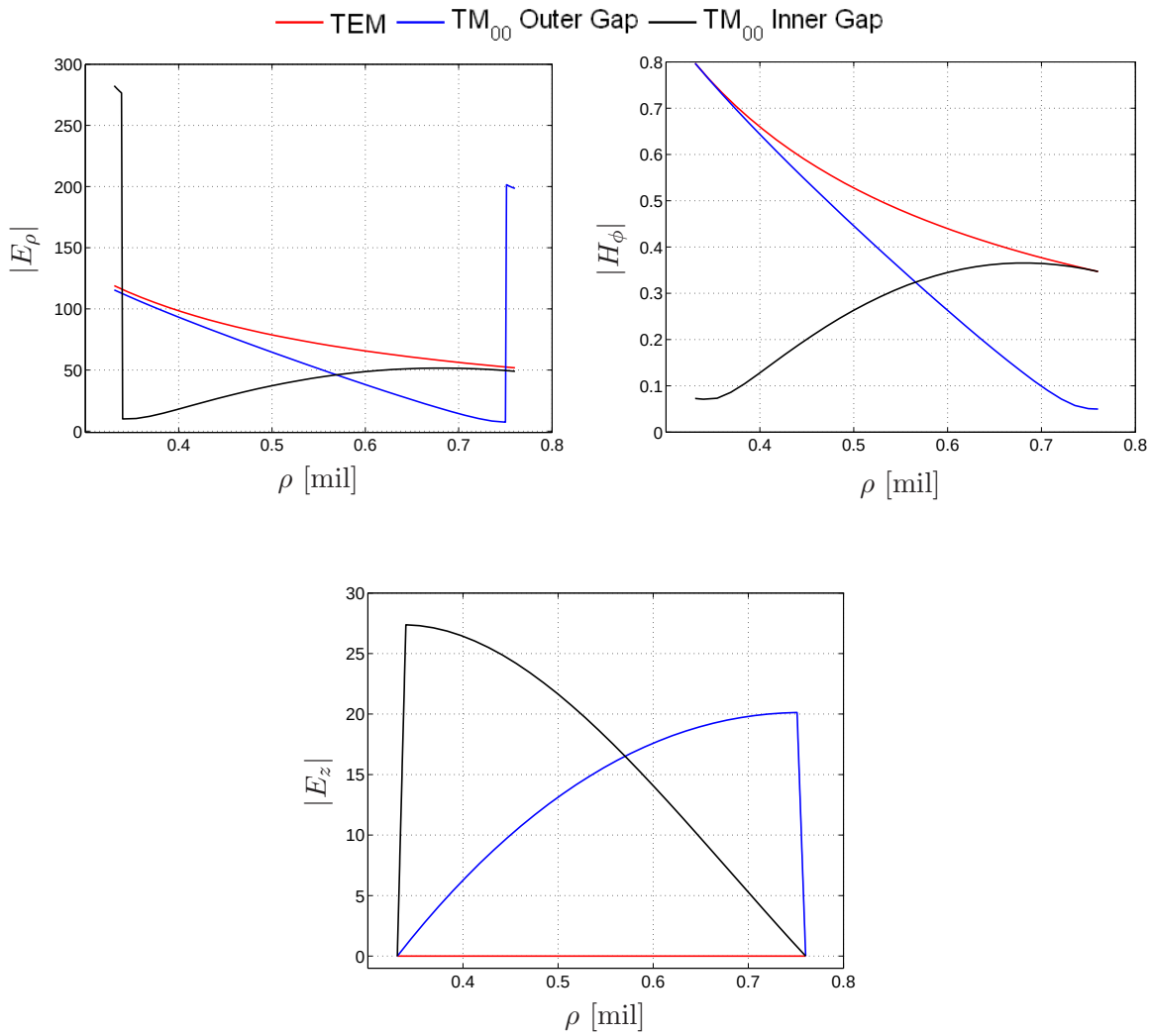

Figure 2.11: Fields at 2 GHz for a MagRAM sample with a 9 mil air gap. The MagRAM sample properties are $\epsilon_r = 21.03 - i(17.71)$ and $\mu_r = 4.289 - i(0.4633)$. For the coaxial test fixture, the inner and outer conductor radii are 0.331 mil and 0.76025 mil respectively.

III. Full Wave Modal Method

Accurate material characterization measurements where air gaps exist between the sample and test fixture conductors require consideration of the higher order modes excited by the air gap. The full wave modal method describes the relationship between the fields within Regions I, II, and III of figure 3.1 as a function of the frequency and material permittivity, ϵ, and permeability, μ. The analysis is directed at determining a theoretical value for the scattering parameters, S_{11}^{thy} and S_{21}^{thy}, given the specific gap scenario and measured gap size. The calculated theoretical values are compared to the experimentally measured values[1] as

$$\begin{aligned} \left| S_{11}^{\text{thy}}(\omega, \epsilon, \mu) - S_{11}^{\text{exp}}(\omega) \right| < T \\ \left| S_{21}^{\text{thy}}(\omega, \epsilon, \mu) - S_{21}^{\text{exp}}(\omega) \right| < T \end{aligned} \tag{3.1}$$

A Newton root search over the parameters ϵ and μ is executed to achieve the selected threshold, T (i.e. (3.1) is evaluated with different values of ϵ and μ until both equations are true). The values of ϵ and μ used in the final iteration are assumed to be the actual values for the material being measured.

3.1 General Modal Analysis

Modal analysis is a method of solving a linear system for unknown parameters by considering all the potential solutions or modes of the system. Applied to a guided-wave problem, the modes are the electric and magnetic field particular solutions of the Helmholtz wave equation. A primary advantage of modal analysis is the clear physical picture maintained through the development that not only calculates the unknown parameters, but readily reveals the reason for the solution. The three steps of modal analysis are

1. Describe the potential modes of the system (field expansion),

[1] As cited previously, the reverse measurements, S_{22} and S_{12} may be used interchangeable with the forward measurements, S_{11} and S_{21}

2. apply system boundary conditions at interfaces to ensure uniqueness of the solution,
3. and apply a selected testing operator to generate a linear system of equations that is well-posed.

The resulting system of equations are in the form

$$\overline{\overline{\mathbf{A}}}\mathbf{x} = \mathbf{b} \tag{3.2}$$

where the unknown vector $\mathbf{x}$ is readily solved for via linear algebra techniques. Physically, the modal analysis matrix (MAM), $\overline{\overline{\mathbf{A}}}$, for the guided wave system of this research describes the coupling between field modes. The forcing vector $\mathbf{b}$ describes the system excitation and the unknown vector $\mathbf{x}$ describes the interaction of field modes at transverse system boundaries, or more specifically the reflection and transmission coefficients. The needed scattering parameters, S_{11}^{thy} and S_{21}^{thy}, are extracted from the vector $\mathbf{x}$.

3.1.1 General Definition of System Modes. An infinite number of modes are possible given the general solution of fields within a guided wave system and application of the appropriate boundary conditions. The total transverse electric and magnetic field at any point in the system is described as the superposition of each potential mode

$$\mathbf{E}_t^{\pm} = \sum_{n=1}^{\infty} a_n^{\pm} \mathbf{e}_n e^{\mp\gamma_n z} \tag{3.3}$$

$$\mathbf{H}_t^{\pm} = \sum_{n=1}^{\infty} \pm a_n^{\pm} \mathbf{h}_n e^{\mp\gamma_n z} \quad , \quad \mathbf{h}_n = \frac{\hat{z} \times \mathbf{e}_n}{Z_n} \tag{3.4}$$

where the subscript t represents only the fields transverse to the direction of propagation ($\hat{z}$), $\gamma_n = jk_z$ is the $\hat{z}$ directed wavenumber, and Z_n is the wave impedance of mode n. Coefficients $a_n^{\pm}$ represent the complex amplitudes associated with each

mode. The coefficients are unique and constant [2] for each material region the field is defined in and for each mode. The term $e^{\mp\gamma_n z}$ describes the field's propagation along the $\hat{z}$ axis.[3]

The field vectors $\mathbf{e}_n$ and $\mathbf{h}_n$ are mode dependent vectors describing the electric and magnetic field components transverse to the direction of propagation. Discontinuities in the coaxial line are assumed to be planar and perpendicular to the primary axis of the coaxial line. Therefore, only the transverse components are retained in order to satisfy the tangential boundary conditions at transverse discontinuities. The complex amplitude and field vector terms may differ mathematically for each n (i.e. TEM or TM^z fields) and may differ over the cross section of the coaxial line (i.e. different air gap sizes). Therefore, the general descriptions of (3.3) and (3.4) are used to simplify the subsequent development.

The sign reversal with respect to direction of propagation for the magnetic field of (3.4) is necessary for the mathematical description to match the physical power flow in the system. The time average power flow in the direction of propagation is given by [5]:

$$P_e = \frac{1}{2}\left(E \times H^* \cdot \hat{n}\right) \tag{3.5}$$

where $\hat{n}$ is the field propagation direction. Using the field descriptions in (3.3) and (3.4) evaluated at $z = 0$, the power flow is

$$\begin{aligned} P_e &= \frac{1}{2}\left\{\left(a_n^{\pm}\mathbf{e}_n e^{-\gamma_n z}\right) \times \left(a_n^{\pm}\mathbf{h}_n e^{-\gamma_n z}\right)^* \cdot \hat{n}\right\}) \\ &= \frac{|a_n^{\pm}|^2}{2Z_n}\left\{\mathbf{e}_n \times (\hat{z} \times \mathbf{e}_n)\right\} \cdot \hat{n} \\ &= \frac{|a_n^{\pm}|^2}{2Z_n}\left\{(\mathbf{e}_n \cdot \mathbf{e}_n)\hat{z} - (\mathbf{e}_n \cdot \hat{z})\mathbf{e}_n\right\} \cdot \hat{n} \\ &= \frac{|a_n^{\pm} e_n|^2}{2Z_n}\left(\hat{z} \cdot \hat{n}\right) \end{aligned}$$

[2]The materials for this analysis are assumed to linear, homogenous, and isotropic (i.e. simple media) and therefore each $a_n^{\pm}$ is a constant.

[3]By convention ($exp^{j\omega t}$), the term $e^{\mp\gamma z}$ implies a field propagating in the $\pm\hat{z}$ direction

Forward propagating fields ($\hat{n} = \hat{z}$) exhibit an expected positive power flow, P_e, along $\hat{z}$. Reverse propagating fields ($\hat{n} = -\hat{z}$) exhibit a non-physical reverse power flow. Therefore, the sign of the magnetic field, $\hat{h}_n$, is made equivalent to the sign of the direction of propagation to ensure the system matches the physical expectation of a positive power flow in the direction of propagation.

The general field definitions of (3.3) and (3.4) are applied using figure 3.1 as a guide to define the *possible* field modes of the system. Physically, the coaxial line system is excited from Region I by a single, $\hat{z}$ travelling TEM field produced by a network analyzer. Therefore, (3.3) and (3.4) in Region I are

$$\left.\begin{array}{l} a_1^+ \mathbf{e}_1 e^{-\gamma_1 z} + \sum\limits_{n=1}^{\infty} a_n^- \mathbf{e}_n e^{+\gamma_n z} \\ a_1^+ \mathbf{h}_1 e^{-\gamma_1 z} - \sum\limits_{n=1}^{\infty} a_n^- \mathbf{h}_n e^{+\gamma_n z} \end{array}\right\} z < 0 \tag{3.6}$$

where the frequency of excitation is assumed below the cutoff frequency of the next higher mode and therefore only a single, forward propagating mode is excited. It is also assumed that the NWA is perfectly matched to the system so there are no reflections from the excitation port of the NWA (see figure 2.1)[4]. Therefore, only one forward propagating wave (the excitation) will exist, yet an infinite number of reverse propagating fields (reflections from the Region I to Region II boundary) will exist where all but the $n = 1$ field will be evanescent.

The configuration of fields in Region II, although possessing the same general form (3.3) and (3.4), may be significantly different. Therefore, the general forms are defined uniquely for the fields in Region II as

$$\left.\begin{array}{l} \sum\limits_{n=1}^{\infty} b_n^+ \tilde{\mathbf{e}}_n e^{-\tilde{\gamma}_n z} + \sum\limits_{n=1}^{\infty} b_n^- \tilde{\mathbf{e}}_n e^{+\tilde{\gamma}_n z} \\ \sum\limits_{n=1}^{\infty} b_n^+ \tilde{\mathbf{h}}_n e^{-\tilde{\gamma}_n z} - \sum\limits_{n=1}^{\infty} b_n^- \tilde{\mathbf{h}}_n e^{+\tilde{\gamma}_n z} \end{array}\right\} 0 < z < L \tag{3.7}$$

[4]In practice, the network analyzer will not be perfectly matched to the test system. A perfectly matched measurement device is a good assumption though if a good calibration of the system is accomplished prior to measurement.

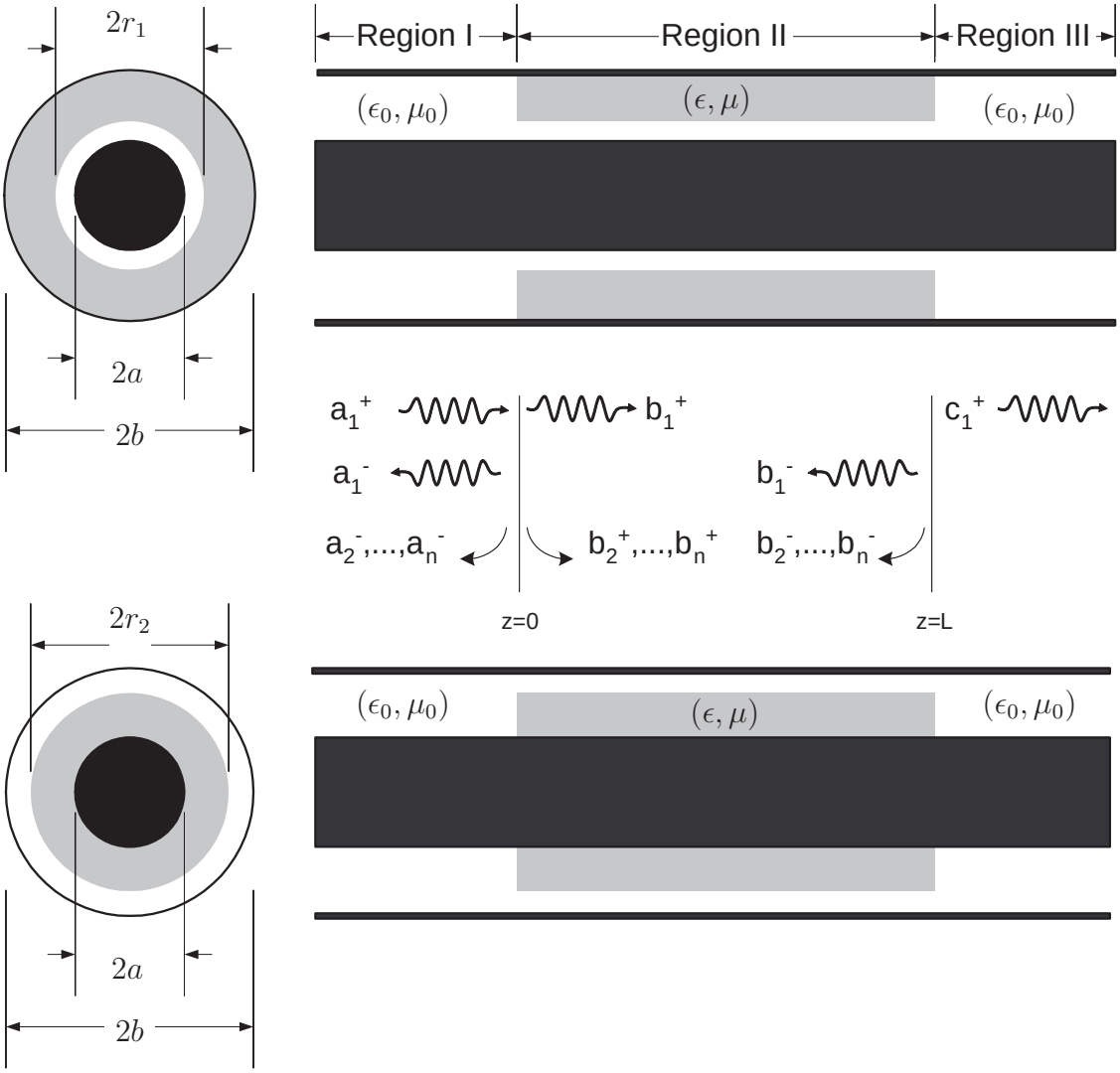

Figure 3.1: The air gap in Region II presents a discontinuity that will excite higher-order modes. The bandwidth of the measurement is chosen so that only one mode (subscript 1) propagates and any higher order modes evanescence (subscripts 2,...,n).

recognizing that the material and makeup of Region II may produce different field vectors and complex amplitudes then Region I.

Region III is filled with freespace as in Region I. As in Region I, the NWA is assumed to operate at a frequency where only a single propagating mode is supported by the coaxial line and that the network analyzer is perfectly matched to the system. Therefore, the fields for Region III are given by

$$\left.\begin{array}{l} \sum_{n=1}^{\infty} c_n^+ \mathbf{e}_n e^{-\gamma_n (z-L)} \\ \sum_{n=1}^{\infty} c_n^+ \mathbf{h}_n e^{-\gamma_n (z-L)} \end{array}\right\} L < z \tag{3.8}$$

where only forward propagating fields are present and where all but the $n = 1$ field will be evanescent. It follows then that the $n = 1$ is the only field measured by the NWA[5]. The complex amplitude, c_n^+, is referenced to the boundary at $z = L$ by including a phase shift of L,

$$c_n^+ e^{\gamma_n L} e^{-\gamma_n z} = c_n^+ e^{-\gamma_n (z-L)}$$

in the field definition. This is done to simplify subsequent analysis.

3.1.2 Application of Boundary Conditions. The transverse components of the electric and magnetic fields are continuous across the transverse interfaces between Region I and II, and Region II and III as shown in figure 3.1 [3]. Boundary conditions

[5]Certainly evanescent fields carry power that may reach the NWA, but the attenuation is significant provided the NWA detectors are reasonably far from the material being measured. It is assumed that any evanescent field power at the NWA detectors is significantly below detection capability of the NWA and therefore insignificant.

at $z = 0$ and $z = L$ due to the presence of the sample in the coaxial line are

$$\begin{aligned}
\hat{n} \times \mathbf{E}^I(z = 0^-) &= \hat{n} \times \mathbf{E}^{II}(z = 0^+) \\
\hat{n} \times \mathbf{H}^I(z = 0^-) &= \hat{n} \times \mathbf{H}^{II}(z = 0^+) + \mathbf{J}_s(z = 0) \\
\hat{n} \times \mathbf{E}^{II}(z = L^-) &= \hat{n} \times \mathbf{E}^{III}(z = L^+) \\
\hat{n} \times \mathbf{H}^{II}(z = L^-) &= \hat{n} \times \mathbf{H}^{III}(z = L^+) + \mathbf{J}_s(z = L)
\end{aligned}$$

Assuming the sample has no impressed sources present is non-conducting ($\mathbf{J}_s = 0$) and that $\hat{n} = \hat{z}$, the boundary conditions are simplified to

$$\begin{aligned}
\mathbf{E}_t^I(z = 0^-) &= \mathbf{E}_t^{II}(z = 0^+) \\
\mathbf{H}_t^I(z = 0^-) &= \mathbf{H}_t^{II}(z = 0^+) \\
\mathbf{E}_t^{II}(z = L^-) &= \mathbf{E}_t^{III}(z = L^+) \\
\mathbf{H}_t^{II}(z = L^-) &= \mathbf{H}_t^{III}(z = L^+)
\end{aligned}$$

A system of linear equations is formed by substituting the field equations defined in (3.6), (3.7), and (3.8) into the boundary conditions as

$$\begin{aligned}
a_1^+ \mathbf{e}_1 + \sum_{n=1}^{\infty} a_n^- \mathbf{e}_n &= \sum_{n=1}^{\infty} b_n^+ \tilde{\mathbf{e}}_n + \sum_{n=1}^{\infty} b_n^- \tilde{\mathbf{e}}_n \\
a_1^+ \mathbf{h}_1 - \sum_{n=1}^{\infty} a_n^- \mathbf{h}_n &= \sum_{n=1}^{\infty} b_n^+ \tilde{\mathbf{h}}_n - \sum_{n=1}^{\infty} b_n^- \tilde{\mathbf{h}}_n \\
\sum_{n=1}^{\infty} b_n^+ \tilde{\mathbf{e}}_n e^{-\tilde{\gamma} L} + \sum_{n=1}^{\infty} b_n^- \tilde{\mathbf{e}}_n e^{\tilde{\gamma} L} &= \sum_{n=1}^{\infty} c_n^+ \mathbf{e}_n \\
\sum_{n=1}^{\infty} b_n^+ \tilde{\mathbf{h}}_n e^{-\tilde{\gamma} L} - \sum_{n=1}^{\infty} b_n^- \tilde{\mathbf{h}}_n e^{\tilde{\gamma} L} &= \sum_{n=1}^{\infty} c_n^+ \mathbf{h}_n
\end{aligned}$$

Recalling that the scattering parameters are the ratio of incident to reflected energy, the system is scaled by $\frac{1}{a_1^+}$. This translates the constant coefficients, a, b, and c, to

the scattering parameters per mode at each transverse interface or

$$\begin{aligned} R_n &= \frac{a_n^-}{a_1^+} & r_n &= \frac{b_n^-}{a_1^+} \\ T_n &= \frac{c_n^+}{a_1^+} & t_n &= \frac{b_n^+}{a_1^+} \end{aligned}$$

where R_n are the reflection coefficients at $z = 0$, r_n are the ratio of fields reflected at $z = L$ and propagated to $z = 0$ over the incident field, t_n are the transmission coefficients for the $z = 0$ boundary, and T_n are the transmission coefficients through the material. It is evident that the terms needed for the comparisons in (3.1) are

$$\begin{aligned} \mathrm{S}_{11}^{\mathrm{thy}} &= R_1 = \frac{a_1^-}{a_1^+} \\ \mathrm{S}_{21}^{\mathrm{thy}} &= T_1 = \frac{c_1^+}{a_1^+} \end{aligned} \tag{3.9}$$

By substituting the scattering parameters per mode into the linear system and truncating the summations to N for the sake of computability, the linear system

$$\begin{aligned} \sum_{n=1}^{N} R_n \mathbf{e}_n - \sum_{n=1}^{N} t_n \tilde{\mathbf{e}}_n - \sum_{n=1}^{N} r_n \tilde{\mathbf{e}}_n &= -\mathbf{e}_1 \\ \sum_{n=1}^{N} R_n \mathbf{h}_n + \sum_{n=1}^{N} t_n \tilde{\mathbf{h}}_n - \sum_{n=1}^{N} r_n \tilde{\mathbf{h}}_n &= \mathbf{h}_1 \\ \sum_{n=1}^{N} t_n \tilde{\mathbf{e}}_n e^{-\tilde{\gamma}_n L} + \sum_{n=1}^{N} r_n \tilde{\mathbf{e}}_n e^{\tilde{\gamma}_n L} - \sum_{n=1}^{N} T_n \mathbf{e}_n &= 0 \\ \sum_{n=1}^{N} t_n \tilde{\mathbf{h}}_n e^{-\tilde{\gamma}_n L} - \sum_{n=1}^{N} r_n \tilde{\mathbf{h}}_n e^{\tilde{\gamma}_n L} - \sum_{n=1}^{N} T_n \mathbf{h}_n &= 0 \end{aligned} \tag{3.10}$$

is now a set of 4 equations with $4N$ unknowns. Although a very clear physical picture is drawn by the system, it is just as clear that the system is unsolvable for $N > 1$. For $N = 1$, the system is well-posed, but does not account for higher order modes.

3.1.3 Select and Apply Testing Operator. A testing operator is applied to the system of equations to produce a well-posed system (i.e. 4N equations by 4N unknowns). The selection of the testing operator should be physically meaningful,

not alter the scattering parameter definitions, and not introduce excessive complexity into the system. It is also advantageous computationally if the set of testing operators is orthogonal to a large set of the field equations.

The Region I fields meet the criteria set for testing operators. Coupling between two field modes is determined by multiplying the two fields together and integrating over the cross-section of the coaxial line as shown in section 2.2. The scattering parameters are constant over the surface of integration and are therefore not altered by applying the testing operator. This is true for the fields in all three regions, but the fields within region I and III (see figure 3.1) are identical, orthogonal for $m \neq n$ (as shown in appendix D), and unaltered for different air gap widths and material properties. Additionally, the fields in region I and III are defined by a single expression valid over the entire cross-section, whereas the region II fields are defined by unique expressions in the material and air gap. Using region II fields would require two integrations in application of the testing operators, whereas using region I fields as the testing operator results in a single integration (per mode, per operator) when testing in region I and III.

The testing operator is applied term-by-term to the linear system of equations as

$$\int_{CS} \mathbf{e}_m \cdot \{\} dS \qquad (m = 1, 2, \ldots, N) \qquad \ldots \text{Operator for E-field} \tag{3.11}$$

$$\int_{CS} \mathbf{h}_m \cdot \{\} dS \qquad (m = 1, 2, \ldots, N) \qquad \ldots \text{Operator for H-field} \tag{3.12}$$

where the integration CS is over the cross section of the coaxial line. The resulting system of linear equations is well-posed and in the desired form, (3.1), as

$$\begin{pmatrix} A_{mn} & -B_{mn} & -B_{mn} & 0 \\ \dfrac{A_{mn}}{Z_m Z_n} & C_{mn} & -C_{mn} & 0 \\ 0 & B_{mn}e^{-\tilde{\gamma}_n L} & B_{mn}e^{\tilde{\gamma}_n L} & -A_{mn} \\ 0 & C_{mn}e^{-\tilde{\gamma}_n L} & -C_{mn}e^{\tilde{\gamma}_n L} & -\dfrac{A_{mn}}{Z_m Z_n} \end{pmatrix} \begin{pmatrix} R_n \\ t_n \\ r_n \\ T_n \end{pmatrix} = \begin{pmatrix} -A_{m1} \\ \dfrac{1}{Z_1 Z_1} A_{m1} \\ 0 \\ 0 \end{pmatrix} \tag{3.13}$$

where rows are indicated by m, columns by n, and the submatrices A_{mn}, B_{mn}, and C_{mn} are defined as

$$A_{mn} = \int_{CS} \mathbf{e}_m \cdot \mathbf{e}_n \, dS \tag{3.14}$$

$$B_{mn} = \int_{CS} \mathbf{e}_m \cdot \tilde{\mathbf{e}}_n \, dS \tag{3.15}$$

$$C_{mn} = \int_{CS} \mathbf{h}_m \cdot \tilde{\mathbf{h}}_n \, dS \tag{3.16}$$

The relationship between $\mathbf{e}$ and $\mathbf{h}$ eliminates the need to define a submatrix for applying a magnetic testing operator, $\mathbf{h}$, to the Region I and III magnetic fields. The electric and magnetic transverse mode vectors, $\mathbf{e}_n$ and $\mathbf{h}_n$ are related as

$$\mathbf{h}_n = \frac{\hat{z} \times \mathbf{e}_n}{Z_n}$$

where Z_n is the wave impedance for mode n. Using this relationship, the product and integration of the testing operator and fields is reduced to

$$\begin{aligned}
\int_{CS} \mathbf{h}_m \cdot \mathbf{h}_n dS &= \int_{CS} \frac{\hat{z} \times \mathbf{e}_m}{Z_m} \cdot \frac{\hat{z} \times \mathbf{e}_n}{Z_n} dS \\
&= \frac{1}{Z_m Z_n} \int_{CS} (\hat{z} \times \mathbf{e}_m) \cdot (\hat{z} \times \mathbf{e}_n) \; dS \\
&= \frac{1}{Z_m Z_n} \int_{CS} \{(\hat{z} \cdot \hat{z})(\mathbf{e}_m \cdot \mathbf{e}_n) - (\hat{z} \cdot \mathbf{e}_n)(\mathbf{e}_m \cdot \hat{z})\} \; dS \\
&= \frac{1}{Z_m Z_n} \int_{CS} \mathbf{e}_m \cdot \mathbf{e}_n \; dS
\end{aligned}$$

This reduction is only valid in Region I and III because the fields in these regions are defined independently of the material or air gap in Region II and the fields are defined over the entire surface of integration. If the dimensions of the coaxial test fixture remain fixed, the fields in Region I and III will vary only with respect to frequency. This reduction reduces the number of unique submatrices required in (3.13) and thereby reduces the computational load in forming the MAM.

The ill-posed system of equations, (3.10), is now a well-posed system, (3.13), that generally describes the inter-relationship of fields in the three coaxial test fixture regions. The system is in the form

$$\overline{\overline{\mathbf{A}}}\mathbf{x} = \mathbf{b} \tag{3.17}$$

where the vector $\mathbf{x}$ is readily solved for via linear algebra techniques and contains the scattering parameters, S_{11}^{thy} and S_{21}^{thy}, necessary to complete the minimization in (3.1) and determine the sample permittivity, ϵ, and permeability, μ.

3.2 Application of Modal Analysis

The modal analysis method to this point is not particular to a coaxial test fixture. The system of (3.13) is applicable to material measurements in any typical closed waveguide (i.e. rectangular or cylindrical). Although this research considers an air gap discontinuity, this fact is not used in developing the system of (3.13). The field equations within Region II characterize the effects of the air gaps. Therefore, to specify the general solution to a particular problem and waveguide configuration requires specifying the transverse electric and magnetic fields, $\mathbf{e}_n$, $\mathbf{h}_n$, $\tilde{\mathbf{e}}_n$, and $\tilde{\mathbf{h}}_n$, in the individual regions of the waveguide. Following this, the integrals (3.14), (3.15), and (3.16) must also be evaluated based on the defined transverse mode vectors and air gap scenario (inner or outer).

3.2.1 Mode Dependent Transverse Electric and Magnetic Field Vectors.

Region I and III are freespace-filled coaxial line. The fields are well-documented [10] and are derived in appendix F. As stated earlier, the system excitation is TEM and the axially symmetric air gaps in Region II are expected to excite axially symmetric, $(m = 0)$, TM^z modes. The mode dependent transverse field vectors, $\mathbf{e}_n$ and $\mathbf{h}_n$, as defined (3.6), (3.7), and (3.8) are the z-independent terms of the field equations.

Considering only forward propagating fields, the general equations in appendix F reduce to

$$E_\rho = \left[\frac{1}{\rho}\right] e^{-jkz} \tag{3.18}$$

$$H_\phi = \frac{1}{Z_n}\left[\frac{1}{\rho}\right] e^{-jkz} \tag{3.19}$$

for the TEM mode and

$$\begin{aligned} E_\rho &= \frac{\pi\gamma k_\rho}{j2k} V_1\left(k_{\rho_n}\rho\right) e^{-\gamma z} \\ E_z &= \frac{\pi k_{\rho_n}^2}{j2k} V_0\left(k_{\rho_n}\rho\right) e^{-\gamma z} \\ H_\phi &= \frac{\pi\gamma k_\rho}{j2k}\left[\frac{1}{Z_n}\right] V_1\left(k_{\rho_n}\rho\right) e^{-\gamma z} \\ H_z &= 0 \quad , \qquad H_\rho = 0 \quad , \qquad E_\phi = 0 \end{aligned}$$

where

$$V_m\left(\alpha\rho\right) = J_m\left(\alpha\rho\right) Y_0\left(\alpha a\right) - J_0\left(\alpha a\right) Y_m\left(\alpha\rho\right)$$

and the characteristic equation for k_{ρ_n} is

$$V_0\left(k_{\rho_n}b\right) = J_0\left(k_{\rho_n}b\right) Y_0\left(k_{\rho_n}a\right) - J_0\left(k_{\rho_n}a\right) Y_0\left(k_{\rho_n}b\right) = 0 \tag{3.20}$$

for the TM_{0n}^z modes. Note that $V_0\,' = -V_1$ and that the fields above are normalized to a TEM field of $\frac{1}{\rho}e^{-jkz}$ using the constant Υ, defined in appendix F as

$$\Upsilon = \frac{2kB_{0,n}^+}{\pi\omega\mu\epsilon}$$

This will simplify subsequent calculations. Based on these field definitions, the mode dependent transverse field vectors for Regions I and III are

$$\mathbf{e}_n = \begin{cases} \dfrac{1}{\rho}\,\hat{\rho} & \ldots \quad n = 1 \\ \\ \dfrac{\pi\gamma_n k_{\rho_n}}{j2k} V_1\left(k_{\rho_n}\rho\right)\ \hat{\rho} & \ldots \quad n > 1 \end{cases}$$

$$\mathbf{h}_n = \begin{cases} \dfrac{1}{Z_n}\left[\dfrac{1}{\rho}\right]\ \hat{\phi} & \ldots \quad n=1 \\ \\ \dfrac{\pi\gamma_n k_{\rho_n}}{j2k}\left[\dfrac{1}{Z_n}\right] V_1\left(k_{\rho_n}\rho\right)\ \hat{\phi} & \ldots \quad n>1 \end{cases}$$

where

$$\gamma_n^2 = k_{\rho_n}^2 - k^2 \qquad k = \omega\sqrt{\mu\epsilon}$$

$$Z_n = \frac{\gamma_n}{j\omega\epsilon}$$

and k_{ρ_n} is the $n-1$ zero of (3.20). For $n=1$, the TEM field, $k_{\rho_1}=0$ and therefore $Z_1 = \sqrt{\frac{\mu}{\epsilon}}$ which is the expected wave impedance for a TEM field.

The fields in Region II are defined in section 2.5. The forward propagating field equations, normalized to a TEM field of $\frac{1}{\rho}e^{-\gamma_1 z}$ using the constant Υ just as in the Region I and III fields, are

$$E_\rho = \begin{cases} \dfrac{\pi k_{\rho_{1n}}\tilde{\gamma}_n}{j2k_1}\ V_1\left(k_{\rho_{1n}}\rho\right)E_{1n}e^{-\tilde{\gamma}_n z} & \ldots \quad a<\rho<R \\ \\ \dfrac{\pi k_{\rho_{2n}}\tilde{\gamma}_n}{j2k_2}\ W_1\left(k_{\rho_{1n}}\rho\right)F_{1n}e^{-\tilde{\gamma}_n z} & \ldots \quad R<\rho<b \end{cases}$$

$$H_\phi = \begin{cases} \dfrac{\pi k_{\rho_{1n}}\tilde{\gamma}_n}{j2k_1 Z_{1n}}\ V_1\left(k_{\rho_{1n}}\rho\right)E_{1n}e^{-\tilde{\gamma}_n z} & \ldots \quad a<\rho<R \\ \\ \dfrac{\pi k_{\rho_{2n}}\tilde{\gamma}_n}{j2k_2 Z_{2n}}\ W_1\left(k_{\rho_{1n}}\rho\right)F_{1n}e^{-\tilde{\gamma}_n z} & \ldots \quad R<\rho<b \end{cases}$$

$$E_z = \begin{cases} \dfrac{\pi\left(k_{\rho_{1n}}\right)^2}{j2k_1}\ V_0\left(k_{\rho_{1n}}\rho\right)E_{1n}e^{-\tilde{\gamma}_n z} & \ldots \quad a<\rho<R \\ \\ \dfrac{\pi\left(k_{\rho_{2n}}\right)^2}{j2k_2}\ W_0\left(k_{\rho_{1n}}\rho\right)F_{1n}e^{-\tilde{\gamma}_n z} & \ldots \quad R<\rho<b \end{cases}$$

where

$$\tilde{\gamma}_n^2 = k_{\rho_{1n}}^2 - (k_1)^2 \qquad \tilde{\gamma}_n^2 = k_{\rho_{2n}}^2 - (k_2)^2$$

$$k_1 = \omega\sqrt{\mu_1\epsilon_1} \qquad k_2 = \omega\sqrt{\mu_2\epsilon_2}$$

$$Z_{1n} = \frac{\tilde{\gamma}_n}{j\omega\epsilon_1} \qquad Z_{2n} = \frac{\tilde{\gamma}_n}{j\omega\epsilon_2}$$

and

$$W_m(\alpha\rho) = J_m(\alpha\rho)\,Y_0(\alpha b) - J_0(\alpha b)\,Y_m(\alpha\rho)$$

As in section 2.5, the boundary conditions at the material to air gap interface requires that the tangential fields, E_z and H_ϕ, are continuous. Equating the fields at $\rho = R$ produces two continuity factors for the tangential fields

$$E_z(R^-) = E_z(R^+) \quad \text{produces} \quad E_{1n} = F_{1n}\left(\frac{k_{\rho_{2n}}}{k_{\rho_{1n}}}\right)^2 \frac{k_1}{k_2}\,\frac{W_0(k_{\rho_{2n}}R)}{V_0(k_{\rho_{1n}}R)}$$

$$H_\phi(R^-) = H_\phi(R^+) \quad \text{produces} \quad E_{1n} = F_{1n}\,\frac{k_{\rho_{2n}}\;k_1\;Z_{1n}}{k_{\rho_{1n}}\;k_2\;Z_{2n}}\,\frac{W_1(k_{\rho_{2n}}R)}{V_1(k_{\rho_{1n}}R)}$$

and, by equating the continuity factors, the characteristic equation

$$k_{\rho_{1n}} Z_{1n}\; V_0(k_{\rho_{1n}}R)\;\; W_1(k_{\rho_{2n}}R) - k_{\rho_{2n}} Z_{2n}\; V_1(k_{\rho_{1n}}R)\;\; W_0(k_{\rho_{2n}}R) = 0 \tag{3.21}$$

where $k_{\rho_{1n}}$ and $k_{\rho_{2n}}$ are the nth solution. This is equivalent to (2.7), but is reprinted here in simplified form.

Either of the continuity factors can be inserted into the field equations because the characteristic equation ensures they are equal in value. Using the continuity factor derived from H_ϕ is instructive though in that the ratio of the impedances $\frac{Z_{1n}}{Z_{2n}}$ reduces to a ratio of the permittivities, $\frac{\epsilon_2}{\epsilon_1}$. Thus, the H_ϕ continuity factor readily shows a discontinuity with respect to the permittivities. This is expected given the constitutive relationship for simple media (see section 2.5).

The continuity factors are defined above to substitute for E_{1n}, but can easily be redefined to substitute for F_{1n}. The choice is arbitrary. For this research, the choice is based on the air gap scenario, inner or outer. Rather than define simple general equations and in order to maintain consistency, the continuity factor is substituted into field equations for the air gap in Region II (i.e. field equations defined in $a < \rho < R$ for inner gap or $R < \rho < b$ for outer gap).

The final field equations for an inner air gap, using the dimensions defined in figure 3.1, are

$$E_\rho = \begin{cases} \dfrac{\pi k_{\rho_{2n}} \tilde{\gamma}_n}{j2k_2} \dfrac{\epsilon_2}{\epsilon_1} \dfrac{W_1\left(k_{\rho_{2n}} r_1\right)}{V_1\left(k_{\rho_{1n}} r_1\right)} V_1\left(k_{\rho_{1n}} \rho\right) F_{1n} e^{-\tilde{\gamma}_n z} & \ldots \quad a < \rho < r_1 \\ \dfrac{\pi k_{\rho_{2n}} \tilde{\gamma}_n}{j2k_2} W_1\left(k_{\rho_{2n}} \rho\right) F_{1n} e^{-\tilde{\gamma}_n z} & \ldots \quad r_1 < \rho < b \end{cases}$$

$$H_\phi = \begin{cases} \dfrac{\pi k_{\rho_{2n}} \tilde{\gamma}_n}{j2k_2 Z_{2n}} \dfrac{W_1\left(k_{\rho_{2n}} r_1\right)}{V_1\left(k_{\rho_{1n}} r_1\right)} V_1\left(k_{\rho_{1n}} \rho\right) F_{1n} e^{-\tilde{\gamma}_n z} & \ldots \quad a < \rho < r_1 \\ \dfrac{\pi k_{\rho_{2n}} \tilde{\gamma}_n}{j2k_2 Z_{2n}} W_1\left(k_{\rho_{2n}} \rho\right) F_{1n} e^{-\tilde{\gamma}_n z} & \ldots \quad r_1 < \rho < b \end{cases}$$

$$E_z = \begin{cases} \dfrac{\pi \left(k_{\rho_{2n}}\right)^2}{j2k_2} \dfrac{W_0\left(k_{\rho_{2n}} r_1\right)}{V_0\left(k_{\rho_{1n}} r_1\right)} V_0\left(k_{\rho_{1n}} \rho\right) F_{1n} e^{-\tilde{\gamma}_n z} & \ldots \quad a < \rho < r_1 \\ \dfrac{\pi \left(k_{\rho_{2n}}\right)^2}{j2k_2} W_0\left(k_{\rho_{2n}} \rho\right) F_{1n} e^{-\tilde{\gamma}_n z} & \ldots \quad r_1 < \rho < b \end{cases}$$

Based on these field definitions, the mode dependent transverse field vectors for Region II when an inner air gap is present are

$$\tilde{\mathbf{e}}_n = \begin{cases} \dfrac{\pi k_{\rho_{2n}} \tilde{\gamma}_n}{j2k_2} \dfrac{\epsilon_2}{\epsilon_1} \dfrac{W_1\left(k_{\rho_{2n}} r_1\right)}{V_1\left(k_{\rho_{1n}} r_1\right)} V_1\left(k_{\rho_{1n}}\rho\right)\ \hat{\rho} & \ldots \quad a < \rho < r_1 \\ \dfrac{\pi k_{\rho_{2n}} \tilde{\gamma}_n}{j2k_2} W_1\left(k_{\rho_{2n}}\rho\right)\ \hat{\rho} & \ldots \quad r_1 < \rho < b \end{cases} \tag{3.22}$$

$$\tilde{\mathbf{h}}_n = \begin{cases} \dfrac{\pi k_{\rho_{2n}} \tilde{\gamma}_n}{j2k_2 Z_{2n}} \dfrac{W_1\left(k_{\rho_{2n}} r_1\right)}{V_1\left(k_{\rho_{1n}} r_1\right)} V_1\left(k_{\rho_{1n}}\rho\right)\ \hat{\phi} & \ldots \quad a < \rho < r_1 \\ \dfrac{\pi k_{\rho_{2n}} \tilde{\gamma}_n}{j2k_2 Z_{2n}} W_1\left(k_{\rho_{2n}}\rho\right)\ \hat{\phi} & \ldots \quad r_1 < \rho < b \end{cases} \tag{3.23}$$

The final field equations for an outer air gap, using the dimensions defined in figure 3.1, are

$$E_\rho = \begin{cases} \dfrac{\pi k_{\rho_{1n}} \tilde{\gamma}_n}{j2k_1} V_1\left(k_{\rho_{1n}}\rho\right) E_{1n} e^{-\tilde{\gamma}_n z} & \ldots \quad a < \rho < r_2 \\ \dfrac{\pi k_{\rho_{1n}} \tilde{\gamma}_n}{j2k_1} \dfrac{\epsilon_1}{\epsilon_2} \dfrac{V_1\left(k_{\rho_{1n}} r_2\right)}{W_1\left(k_{\rho_{2n}} r_2\right)} W_1\left(k_{\rho_{2n}}\rho\right) E_{1n} e^{-\tilde{\gamma}_n z} & \ldots \quad r_2 < \rho < b \end{cases}$$

$$H_\phi = \begin{cases} \dfrac{\pi k_{\rho_{1n}} \tilde{\gamma}_n}{j2k_1 Z_{1n}} V_1\left(k_{\rho_{1n}}\rho\right) E_{1n} e^{-\tilde{\gamma}_n z} & \ldots \quad a < \rho < r_2 \\ \dfrac{\pi k_{\rho_{1n}} \tilde{\gamma}_n}{j2k_1 Z_{1n}} \dfrac{V_1\left(k_{\rho_{1n}} r_2\right)}{W_1\left(k_{\rho_{2n}} r_2\right)} W_1\left(k_{\rho_{2n}}\rho\right) E_{1n} e^{-\tilde{\gamma}_n z} & \ldots \quad r_2 < \rho < b \end{cases}$$

$$E_z = \begin{cases} \dfrac{\pi \left(k_{\rho_{1n}}\right)^2}{j2k_1} V_0\left(k_{\rho_{1n}}\rho\right) E_{1n} e^{-\tilde{\gamma}_n z} & \ldots \quad a < \rho < r_2 \\ \dfrac{\pi \left(k_{\rho_{1n}}\right)^2}{j2k_1} \dfrac{V_0\left(k_{\rho_{1n}} r_2\right)}{W_0\left(k_{\rho_{2n}} r_2\right)} W_0\left(k_{\rho_{2n}}\rho\right) E_{1n} e^{-\tilde{\gamma}_n z} & \ldots \quad r_2 < \rho < b \end{cases}$$

Based on these field definitions, the mode dependent transverse field vectors for Region II when an outer air gap is present are

$$\tilde{\mathbf{e}}_n = \begin{cases} \dfrac{\pi k_{\rho_{1n}} \tilde{\gamma}_n}{j2k_1} \; V_1\left(k_{\rho_{1n}}\rho\right) \; \hat{\rho} & \ldots \quad a < \rho < r_2 \\ \\ \dfrac{\pi k_{\rho_{1n}} \tilde{\gamma}_n}{j2k_1} \; \dfrac{\epsilon_1}{\epsilon_2} \; \dfrac{V_1\left(k_{\rho_{1n}} r_2\right)}{W_1\left(k_{\rho_{2n}} r_2\right)} \; W_1\left(k_{\rho_{2n}}\rho\right) \; \hat{\rho} & \ldots \quad r_2 < \rho < b \end{cases} \tag{3.24}$$

$$\tilde{\mathbf{h}}_n = \begin{cases} \dfrac{\pi k_{\rho_{1n}} \tilde{\gamma}_n}{j2k_1 Z_{1n}} \; V_1\left(k_{\rho_{1n}}\rho\right) \; \hat{\phi} & \ldots \quad a < \rho < r_2 \\ \\ \dfrac{\pi k_{\rho_{1n}} \tilde{\gamma}_n}{j2k_1 Z_{1n}} \; \dfrac{V_1\left(k_{\rho_{1n}} r_2\right)}{W_1\left(k_{\rho_{2n}} r_2\right)} W_1\left(k_{\rho_{2n}}\rho\right) \; \hat{\phi} & \ldots \quad r_2 < \rho < b \end{cases} \tag{3.25}$$

3.2.2 Mode Coupling Integrals in Coaxial Line. The general integrals (3.14), (3.15), and (3.16) can now be defined and evaluated based on the mode vectors of the previous section. The solutions are elements in the matrix (3.13) and are necessary to solve the system of equations.

The surface of integration in each case is the cross-section of the coaxial line. Hence, a double integral with respect to $d\rho$ and $\rho d\phi$ are expected for cylindrical coordinates. Axially symmetric, or ϕ invariant, field excitation is a primary assumption in the preceding development and therefore the integration over $d\phi$ reduces to a constant 2π factor. For example, (3.14) becomes

$$\begin{aligned} \int\limits_{CS} \mathbf{e}_m \cdot \mathbf{e}_n \; dS &= \int\limits_a^b \int\limits_0^{2\pi} \mathbf{e}_m \cdot \mathbf{e}_n \rho d\rho d\phi \\ &= 2\pi \int\limits_a^b \mathbf{e}_m \cdot \mathbf{e}_n \rho d\rho \end{aligned}$$

The factor of 2π is present in all the integrations necessary to populate (3.13) and is therefore normalized out of the following development.

Coupling between fields in the freespace region (Region I and III) are determined from (3.14). Knowing that application of the testing operator is identical in form to testing for orthogonality and that the transverse fields in this region are orthogonal (see appendix D), the solution to (3.14) is 0 for $m \neq n$. The self-coupling, $m = n$, solutions to (3.14) are in two forms. The first for the TEM, $m = n = 1$, field

$$\begin{aligned} A_{11} &= \int_a^b \mathbf{e}_1 \cdot \mathbf{e}_1 \rho d\rho \\ &= \int_a^b \left(\frac{1}{\rho}\,\hat{\rho}\right) \cdot \left(\frac{1}{\rho}\,\hat{\rho}\right) \rho d\rho \\ &= \int_a^b \left(\frac{1}{\rho}\right) d\rho \\ &= \ln\left(\frac{b}{a}\right) \end{aligned}$$

and the second for the TM, $m = n > 1$, fields

$$\begin{aligned} A_{nn} &= \int_a^b \left(\frac{\pi\gamma_n k_{\rho_n}}{j2k} V_1\left(k_{\rho_n}\rho\right)\right)^2 \rho d\rho \\ &= \left(\frac{\pi\gamma_n k_{\rho_n}}{j2k}\right)^2 \int_a^b \left(V_1\left(k_{\rho_n}\rho\right)\right)^2 \rho d\rho \end{aligned}$$

The integration is accomplished using the identity (E.1) and produces

$$A_{nn} = \left(\frac{\pi\gamma_n k_{\rho_n}}{j2k}\right)^2 \left\{ \frac{b^2}{2}\left[\left[V_1(k_{\rho_n}b)\right]^2 + \left[V_0(k_{\rho_n}b)\right]^2 - \frac{1}{k_{\rho_n}b} V_0(k_{\rho_n}b) V_1(k_{\rho_n}b)\right] - \frac{a^2}{2}\left[\left[V_1(k_{\rho_n}a)\right]^2 + \left[V_0(k_{\rho_n}a)\right]^2 - \frac{1}{k_{\rho_n}a} V_0(k_{\rho_n}a) V_1(k_{\rho_n}a)\right]\right\}$$

which is greatly simplified to

$$A_{nn} = \left(\frac{\gamma_n^2}{8k^2}\right)\left\{4 - b^2\pi^2 k_{\rho_n}^2 \left[V_1(k_{\rho_n}b)\right]^2\right\} \tag{3.26}$$

by recognizing the following equalities

$$\begin{aligned} V_0(k_{\rho_n}a) &= 0 && \ldots \text{trivial} \\ V_0(k_{\rho_n}b) &= 0 && \ldots \text{TM field characteristic equation (3.20)} \\ V_1(k_{\rho_n}a) &= \frac{2}{\pi k_{\rho_n}a} && \ldots \text{Wronskian relationship [1]} \end{aligned}$$

The remaining mode coupling integrations, (3.15) and (3.16), require lengthy proofs to simplify. General observations and the final solutions are provided here, but the proofs are relegated to appendix G.

Inner and outer air gap scenarios are shown in figure 3.1. The air gap discontinuities are invariant in ϕ and therefore integration with respect to $d\phi$ is a constant, 2π, as previously noted and is normalized out. The fields in the air gap and material regions are not equivalent and therefore the discontinuity in ρ requires the general integrations of (3.15) and (3.16) be split to

$$B_{mn} = \int_a^R \mathbf{e}_m \cdot \tilde{\mathbf{e}}_n \ \rho d\rho + \int_R^b \mathbf{e}_m \cdot \tilde{\mathbf{e}}_n \rho \ d\rho \tag{3.27}$$

$$C_{mn} = \int_a^R \mathbf{h}_m \cdot \tilde{\mathbf{h}}_n \rho \ d\rho + \int_R^b \mathbf{h}_m \cdot \tilde{\mathbf{h}}_n \rho \ d\rho \tag{3.28}$$

where $R = r_1$ for an inner air gap and $R = r_2$ for an outer air gap. Furthermore, there are two distinct forms of the testing operators $\mathbf{e}_m$ and $\mathbf{h}_m$, namely TEM ($m = 1$) and TM ($m > 1$), and two distinct forms of the field equations $\tilde{\mathbf{e}}_n$ and $\tilde{\mathbf{h}}_n$, one set of equations given an inner air gap and a different set given an outer air gap.

Close comparison of the inner and outer air gap transverse mode vectors in Region II, (3.22) to (3.24) and (3.23) to (3.24), reveals that variations with respect to ρ are identical for each set of equations. Only the constants change depending on an inner or outer air gap scenario. This is true for both the electric and magnetic fields

because

$$\mathbf{h}_n = \frac{\hat{z} \times \mathbf{e}_n}{Z_n}$$

where Z_n is independent of ρ. Thus, rather than the four integrations in (3.27) and (3.28) being carried out for inner and outer gap scenarios, and for a TEM and TM testing operator (a total of 16 unique integrations), only 4 unique integrations are necessary with respect to the ρ varying terms and then modified by the appropriate constants. This not only simplifies the development, but significantly reduces the computation time.

These insights permit simplifying the general proofs of appendix G to computationally efficient, air gap scenario (inner or outer) dependent solutions. The result for an ***outer*** air gap scenario is

$$B_{1n} = \frac{\pi\tilde{\gamma}_n}{j2k_1}\left[\left(\frac{k_{\rho 1n}}{k_{\rho 2n}}\right)^2 - 1\right] V_0(k_{\rho 1n}R) \tag{3.29}$$

$$C_{1n} = \frac{\pi\tilde{\gamma}_n}{j2k_1 Z_n}\left[\frac{1}{Z_{2n}}\left(\frac{k_{\rho 1n}}{k_{\rho 2n}}\right)^2 - \frac{1}{Z_{1n}}\right] V_0(k_{\rho 1n}R) \tag{3.30}$$

and for $m \neq 1$

$$B_{mn} = \frac{\pi\gamma_m k_{\rho m}}{j2k_0}\frac{\pi\tilde{\gamma}_n k_{\rho 1n}}{j2k_1}R \times \left[\left(\frac{1}{k_{\rho m}^2 - k_{\rho 1n}^2} - \frac{1}{k_{\rho m}^2 - k_{\rho 2n}^2}\right) k_{\rho 1n} V_1(k_{\rho m}R)V_0(k_{\rho 1n}R) + \left(\frac{\epsilon_1}{\epsilon_2(k_{\rho m}^2 - k_{\rho 2n}^2)} - \frac{1}{k_{\rho m}^2 - k_{\rho 1n}^2}\right) k_{\rho m} V_0(k_{\rho m}R)V_1(k_{\rho 1n}R)\right] \tag{3.31}$$

$$C_{mn} = \frac{\pi\gamma_m k_{\rho m}}{j2k_0 Z_n}\frac{\pi\tilde{\gamma}_n k_{\rho 2n}}{j2k_2 Z_{1n}}R \times \left[\left(\frac{1}{k_{\rho m}^2 - k_{\rho 1n}^2} - \frac{\epsilon_2}{\epsilon_1(k_{\rho m}^2 - k_{\rho 2n}^2)}\right) k_{\rho 2n} V_1(k_{\rho m}R)V_0(k_{\rho 1n}R) + \left(\frac{1}{k_{\rho m}^2 - k_{\rho 2n}^2} - \frac{1}{k_{\rho m}^2 - k_{\rho 1n}^2}\right) k_{\rho m} V_0(k_{\rho m}R)V_1(k_{\rho 1n}R)\right] \tag{3.32}$$

The result for an ***inner*** air gap scenario is

$$B_{1n} = \frac{\pi\tilde{\gamma}_n}{j2k_2}\left[1-\left(\frac{k_{\rho 2n}}{k_{\rho 1n}}\right)^2\right]W_0(k_{\rho 2n}R) \tag{3.33}$$

$$\tag{3.34}$$

$$C_{1n} = \frac{\pi\tilde{\gamma}_n}{j2k_2Z_n}\left[\frac{1}{Z_{2n}}-\frac{1}{Z_{1n}}\left(\frac{k_{\rho 2n}}{k_{\rho 1n}}\right)^2\right]W_0(k_{\rho 2n}R) \tag{3.35}$$

and for $m \neq 1$

$$\begin{aligned} B_{mn} = \frac{\pi\gamma_m k_{\rho m}}{j2k_0}\frac{\pi\tilde{\gamma}_n k_{\rho 2n}}{j2k_2}R \times \\ \left[\left(\frac{1}{k_{\rho m}^2-k_{\rho 1n}^2}-\frac{1}{k_{\rho m}^2-k_{\rho 2n}^2}\right)k_{\rho 2n}V_1(k_{\rho m}R)W_0(k_{\rho 2n}R) + \right. \\ \left.\left(\frac{1}{k_{\rho m}^2-k_{\rho 2n}^2}-\frac{\epsilon_2}{\epsilon_1(k_{\rho m}^2-k_{\rho 1n}^2)}\right)k_{\rho m}V_0(k_{\rho m}R)W_1(k_{\rho 2n}R)\right] \end{aligned} \tag{3.36}$$

$$\begin{aligned} C_{mn} = \frac{\pi\gamma_m k_{\rho m}}{j2k_0Z_n}\frac{\pi\tilde{\gamma}_n k_{\rho 2n}}{j2k_2Z_{2n}}R \times \\ \left[\left(\frac{\epsilon_1}{\epsilon_2(k_{\rho m}^2-k_{\rho 1n}^2)}-\frac{1}{k_{\rho m}^2-k_{\rho 2n}^2}\right)k_{\rho 2n}V_1(k_{\rho m}R)W_0(k_{\rho 2n}R) + \right. \\ \left.\left(\frac{1}{k_{\rho m}^2-k_{\rho 2n}^2}-\frac{1}{k_{\rho m}^2-k_{\rho 1n}^2}\right)k_{\rho m}V_0(k_{\rho m}R)W_1(k_{\rho 2n}R)\right] \end{aligned} \tag{3.37}$$

The integrations necessary to fill the matrices of (3.13) for both an inner and outer air gap scenario are complex, but computationally possible. Care must be taken in determining the values of $k_{\rho m}$ from (3.20), and $k_{\rho 1n}$ and $k_{\rho 2n}$ from (3.21). Additionally, if the values of $k_{\rho m}^2 - k_{\rho 2n}^2$ or $k_{\rho m}^2 - k_{\rho 1n}^2$ approach 0 the form of (3.36), (3.37), (3.31), and (3.32) will be unstable.

3.3 Summary

A method for calculating theoretical scattering parameters was developed for material characterization measurements where the material does not completely fill

the cross sectional area of a coaxial line test fixture. Expressions for filling the elements of the MAM are given for both an inner and outer air gap. After filling the MAM and forcing vector, $\mathbf{b}$, solving for the reflection and transmission coefficient vector in (3.13) is simply a matter of linear algebra. The needed terms S_{11}^{thy} and S_{21}^{thy} are easily extracted from the solution vector, $\mathbf{x}$, and compared to the measured scattering parameters. If the difference in theoretical and measured scattering parameters is below a user provided tolerance, the permittivity and permeability used in the MAM calculations are representative of the material. If not, a Newton root search iterates the values of permittivity and permeability until the desired tolerance is met.

IV. Full Wave Modal Method Results

The Full Wave Modal Method was developed in the previous chapter for the cases of a sample with inner or outer air gap. The objective of the analysis is to calculate theoretical scattering parameters S_{11}^{thy} and S_{21}^{thy} which are then compared against experimentally measured scattering parameters. The values of permittivity, ϵ, and permeability, μ, for a given frequency, ω, are iterated until the difference is below a specified tolerance, T, or

$$\begin{aligned} \left| S_{11}^{\text{thy}}(\omega, \epsilon, \mu) - S_{11}^{\text{exp}}(\omega) \right| < T \\ \left| S_{21}^{\text{thy}}(\omega, \epsilon, \mu) - S_{21}^{\text{exp}}(\omega) \right| < T \end{aligned} \tag{4.1}$$

and the final values of ϵ and μ are that of the measured sample.

The algorithm uses a Newton's root search to accomplish the minimization in 4.1. For a non-magnetic material, only a 1D complex root search is needed ($\mu_r = 1$), whereas a 2D complex root search is used for magnetic material. In either case, the algorithm requires an initial guess that is updated with each iteration until the final solution is reached.

4.1 Test Setup

The method described in chapter III is implemented in Matlab®. Measurements of the Rexolite® and MagRAM materials shown in chapter II are evaluated using the modal method and the results reported herein. Although multiple samples of Rexolite® and MagRAM were used, all of the samples are assumed to be homogeneous. The material dimensions and electromagnetic properties are described in section 2.3.

The coaxial test fixture is shown assembled in figure 4.2. The coaxial line inner conductor radius is 0.331 inches and outer conductor radius is 0.76025 inches, as described in chapter II. The test fixture center conductor is not held together with hardware. The sample holder center conductor (detail shown in figure 1.1 and 4.1) is flanged on both ends. The center conductor in the sample holder is tension fit

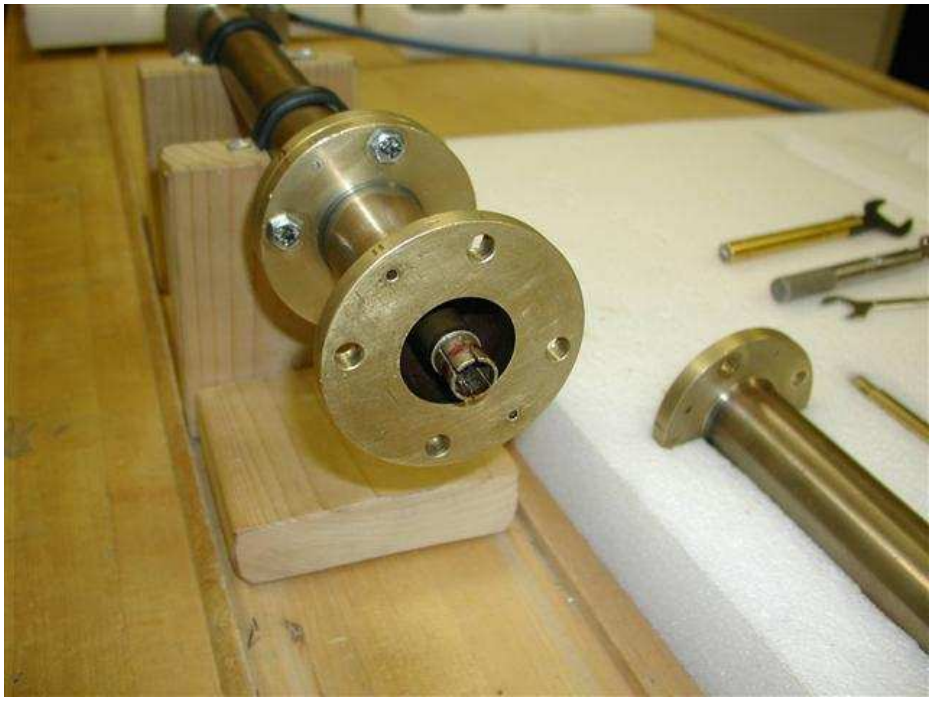

Figure 4.1: Coaxial test fixture opened with center conductor inserted.

into mating center conductor pieces that run the length of the test fixture shown in 4.2. The flanges are soft, but are adjusted when removed to ensure a good electrical contact is made between the two surfaces when reconnected.

The coaxial test fixture is connected to a Network Analyzer for measuring the scattering parameters from 50 MHz to 3.05 GHz as described in chapter II. As mentioned previously, the system, NWA and test fixture (including the sample holder),

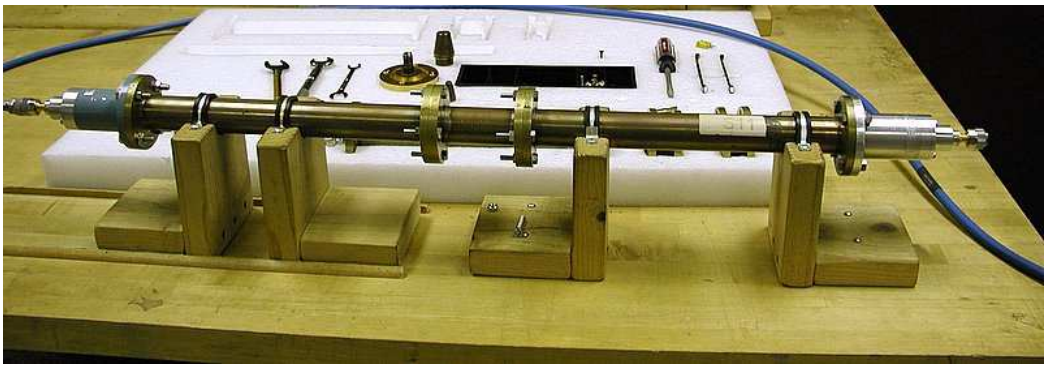

Figure 4.2: Assembled coaxial test fixture.

are calibrated via the TRL method prior to measurement and care is taken to limit cable movement.

4.2 Error Analysis

Sources of potential error include, but are not limited to, uncertainty in sample length measurements and radial thickness of sample. All measurements were made with a calibrated set of calipers with precision of 0.5 mils. Repeated measurements by a second person, showed general accuracy of $\pm$ 1.0 mil from the originally measured values[1]. Both the sample length and radial thickness dimensions were measured using the same method and hence the observed uncertainty in measuring is assumed to be equally applicable to each source.

An error analysis for the real and imaginary permittivity and permeability are accomplished as in [7]. The permittivity and permeability as a function of sample length, L, and sample radius thickness, R, are expanded in a Taylor Series around the original measurements L_0 and R_0 plus measurement uncertainty ΔL and ΔR, respectively. The modal method is not differentiable, as expected by the Taylor Series, but if higher-order terms are assumed negligible and the errors assumed to be relatively small, the exact error is approximated by a sum of partial derivatives, shown here for the real permittivity, as

$$\Delta\epsilon_{\text{exact}}{}' \approx \frac{\partial\epsilon\,'(L,R)}{\partial L}\Delta L + \frac{\partial\epsilon\,'(L,R)}{\partial R}\Delta R$$

[1]The radial thickness of several, random samples were measured a second time by a second, less-experienced individual. The first measurements, made by an individual experienced with the equipment, is assumed to be the actual value.

which are, in turn, approximated using finite difference derivatives. The result, again shown for the real permittivity is a simple form

$$\begin{aligned}
\Delta\epsilon_L{}' \approx \frac{\partial\epsilon'(L,R)}{\partial L}\Delta L &\approx \frac{\epsilon'(L+\Delta L,R)-\epsilon'(L,R)}{\Delta L}\Delta L \\
&= \epsilon'(L+\Delta L,R)-\epsilon'(L,R) \\
\Delta\epsilon_R{}' \approx \frac{\partial\epsilon'(L,R)}{\partial R}\Delta R &\approx \epsilon'(L,R+\Delta R)-\epsilon'(L,R)
\end{aligned}$$

that individually accounts for sources of error. A worst case error estimate is achieved by a composite of the error quantities as a triangle inequality

$$\left|\Delta\epsilon'_{approx}\right| = |\Delta\epsilon'| = |\Delta\epsilon'_L + \Delta\epsilon'_R| \leq |\Delta\epsilon'_L| + |\Delta\epsilon'_R|$$

where the magnitude of the individual terms is used to prevent error cancellation when the terms are opposite in sign. Assuming the errors ΔL and ΔR are relatively small, the error is assumed to be symmetric around the actual value (i.e. +2 mil measurement error will produce the same results as -2 mil measurement error). Error bars on graphs are a result of analyzing uncertainty in sample length and radial thickness of sample measurements of ± 2 mil measurement to produce a conservative estimate of the error.

4.3 Modal Method Performance

The same NWA measurements used to produce figures 2.4 and 2.5 for Rexolite® with 100 mil inner and outer air gap and MagRAM with 9 mil inner and outer air gap respectively, are now used here in evaluating the performance of the modal method.

4.3.1 Modal method performance for Rexolite®. The modal method performed very well for the Rexolite® data considering 10 modes. The permittivity, ϵ'_r and ϵ''_r, is extracted with a high degree of accuracy as shown in figure 4.3. As a low-loss, low dielectric constant material, the wavenumbers for Rexolite® are easily

predicted, producing a single propagating mode and 9 highly evanescent modes (see table 2.2).

The results for ϵ_r'' in Rexolite® are as expected and show very little error. Although the ϵ_r'' are negative at lower frequencies, the magnitude of the values (-.015 being the peak) suggests noise in the system or other unaccounted for anomaly, rather than calculation error. There are, however, two noticeable phenomenon in the ϵ_r' results, namely inner air gap error and data oscillations.

The inner air gap calculation for ϵ_r' is not as accurate as the outer air gap when considering the same number of modes. For a coaxial line filled with freespace and considering the electric field component of a TEM wave, 32% of the potential is in the space between the inner conductor and a point 100 mil out radially. Only 17% of the potential is contained in the space between the outer conductor and a point 100 mil in radially. Applied to the air gap scenario, the sample material perturbs less of the electric field strength when an inner air gap is present versus an outer air gap. Therefore, analysis where an inner gap is present is more susceptible to error, including that from uncertainty in the radial width measurement (as shown in figure 4.4).

Oscillations in the results are attributed to effects within the test system that were not accounted for in the calibration. A TRL calibration of the NWA and coaxial test fixture requires breaking the inner conductor two times. The measurement process requires the coaxial line be broke again to insert the test sample. The act of breaking and reassembling the coaxial line, even during calibration, will effect the quality of the calibration and ultimately the measurement. The oscillations present in figure 4.3 are not significant enough to cause concern.

The impact of sample length measurement on the calculation of ϵ_r'' (figure 4.4(b)) is nearly imperceptible, but worth noting. Assuming a PEC coaxial line, loss within the sample material will be different based on the amount of material the fields travel through. Therefore, uncertainty in the sample length measurement will have a greater

impact on the the calculation of ϵ_r'' versus uncertainty in the radial width measurement of the sample. The small magnitude of the error in ϵ_r'' is a reflection of uncertainty, ± 2 mil, relative to the wavelength, 3.934 in. at 3 GHz.

A primary benefit of the modal method is the convergence of the result to the material properties. As shown in figure 4.5, using additional modes in the analysis does increase the accuracy of the result in an expected manner, but the accuracy gain is insignificant beyond 10 modes. Additionally, increasing the number of modes in the analysis only compensates for higher order mode excitation, not for other errors in the system. Radial width or sample length measurement uncertainty error does not decrease with an increase in the number of modes in the analysis. In figure 4.5, the number of modes is increased to 25. Error due to the radial width and sample length measurement uncertainty converges at the rate the calculated results do proving that the introduction of additional modes *only* compensates for error due to the excitation of those higher order modes.

Modal method performance for different gap sizes was tested as well. In total, 24 Rexolite® samples were machined to produce outer and inner gaps of 1, 2.5, 3.75, 5.25, 20, 40, 60, 80, 100, 200, 300, and 400 mils. As seen in figure 4.7, the modal method is able to accurately calculate the permittivity for each outer air gap size (data shown is for measurements at 2 GHz). The modal method applied to inner air gaps (not shown), produced a similar result up to 300 mil. Not surprisingly, the 400 mil inner air gap results are poor. For a 400 mil inner air gap, only 29.25 mil of Rexolite® lines the inside of the outer conductor and only 5% of the electric potential impinges on the material.

The lumped circuit correction, developed in chapter II, is compared to the modal method for varying gaps in figure 4.7. The lumped circuit model provides good results up to a 60 mil outer air gap and its behavior for greater gap sizes is similar to the modal method although different in magnitude. The lumped circuit correction is applied to the NRW algorithm output. The NRW algorithm uses the same measured

data that the modal method does, but assumes only single mode propagation. For that reason, the NRW algorithm and lumped circuit model behavior will compare well to the modal method when a finite number of modes are used and provides a good confidence metric for the modal method.

A critical assumption of the above theory is an axially symmetric air gap. Failing this assumption will not produce the expected results, even for small amounts of conductor or material eccentricity. In the case of a fully-filled coaxial line measurement, the optimal situation, the center conductor is physically supported by the sample material. When an air gap is introduced, proper support must be added to the center conductor to ensure the weight of the center conductor (for an inner air gap) or the weight of the center conductor plus sample (for an outer gap) do not pull the center conductor off the central axis of the coaxial line.

A test system is easily evaluated for an eccentric center conductor by measuring a known sample with known air gap and comparing the results as the number of modes is increased. An example is shown in figure 4.6, where a sample of Rexolite® only 29.25 mil thick (producing a 400 mil outer air gap) is analyzed using 20 modes. For the eccentric case, the center conductor was measured as 6 mil off the center axis of the coaxial line. The eccentricity of the center conductor limits the convergence of the permittivity (both real and imaginary) to a value different than the known value for the sample. Additionally, the results for ϵ_r'' incorrectly indicate the material is lossy, particularly at lower frequencies. Supports for the center conductor were than added and the measurement retaken. The modal method with 20 modes was used again to calculate the permittivity and the results, also shown in figure 4.6, match the expected value very well. Additionally, ϵ_r'' converges to the expected value over frequency. The low frequency values of ϵ_r'' are non-physical and noisy. The finite conductivity of the coaxial line adversely impacts the measurements at low frequencies, but the noise in the calculation is a good indication (for this thin of a sample) that the major source of error, higher order mode excitation, is accounted for.

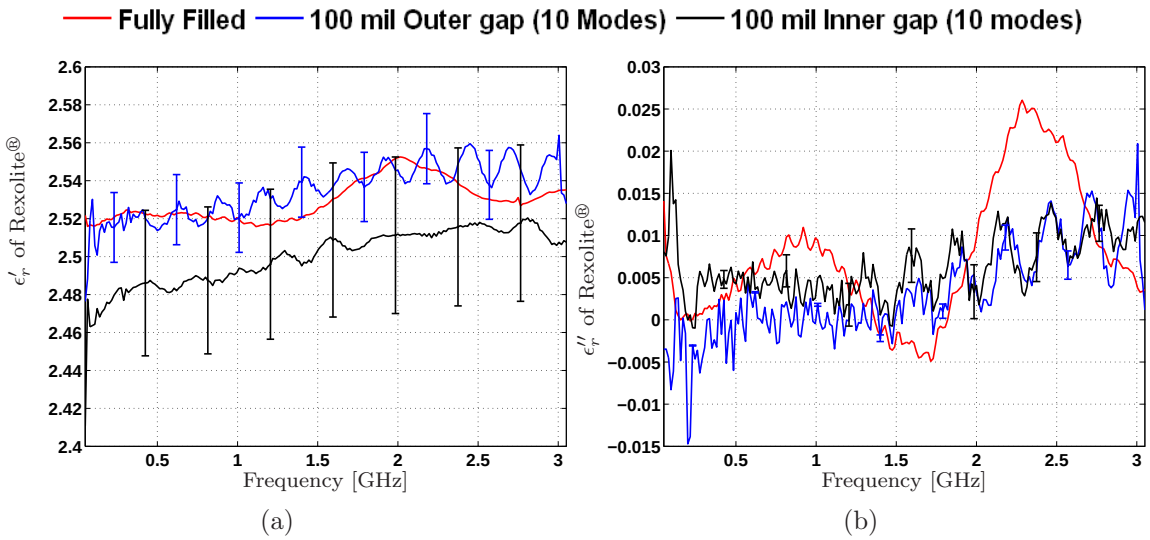

(a) (b)

Figure 4.3: Measured permittivity is shown as $\epsilon_r = \epsilon_r' - j\epsilon_r''$. Error bars indicate potential error in radial width (±2 mil) and length (±2 mil) measurements. Using the modal method with 10 modes considered produces a very accurate correction for the real (a) and imaginary (b) part of the permittivity. Oscillations in the results are on the order of .1 for the real part and .01 for the imaginary part. The oscillations are attributed to system imperfections not accounted for in the calibration.

4.3.2 Modal method performance for MagRAM. The modal method performed reasonably well for the MagRAM data with a 9 mil inner and outer air gap considering 10 modes. The outer air gap result, shown in figure 4.8, is fairly accurate and follows the behavior of the fully filled measurements for all parameters with some error still present in the ϵ_r'' result. The inner air gap data does not follow the behavior of the fully filled data very well at low frequencies for permittivity and high frequencies for permeability.

The error evident in the MagRAM permittivity results indicates one of four things. First, and most likely, eccentricity of the center conductor is again impacting measurements. Although only a small gap exists, the material is heavily loaded. The results, particularly ϵ_r'', indicate that the fields in the system are not exclusively axially symmetric. This conjecture requires additional measurements to prove.

Numerical instability of the Bessel functions with complex arguments is considered the second most likely cause of error. Bessel functions are a fundamental piece

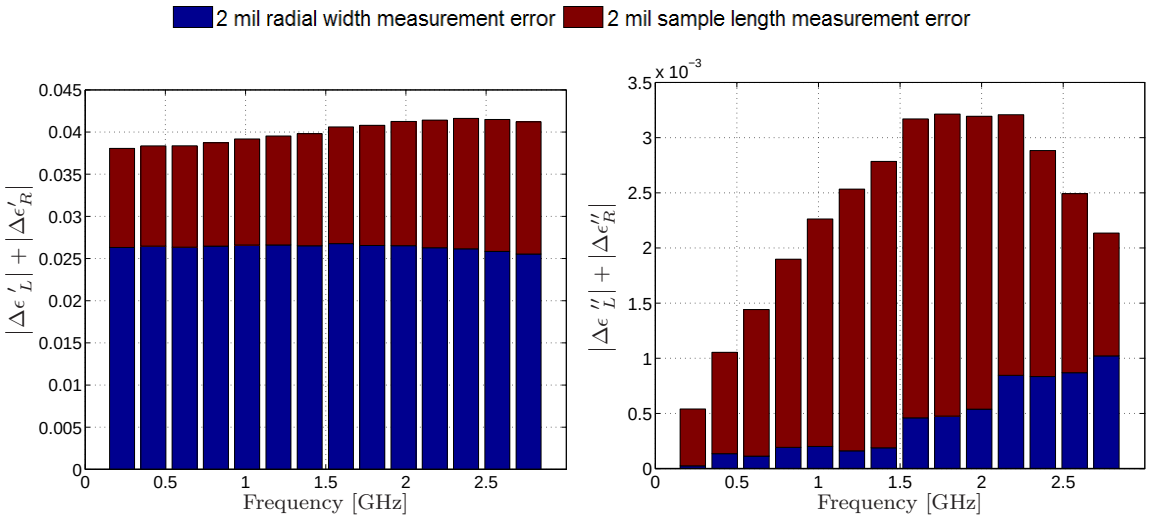

Figure 4.4: Permittivity of Rexolite® with 100 mil inner air gap using 10 mode analysis is shown for measurement error in sample radial width (air gap is 100 mil ±2 mil) and length (sample length is 1 in ±2 mil). Measurement of ϵ'_r is more impacted by error in the radial width measurement because of the high field concentration at the center conductor. Measurement of ϵ''_r is impacted more by the sample length measurement error as a homogeneous sample will produce more or less loss in the system as the length is decreased or increased respectively. Error in the real (a) and imaginary (b) part of the calculated permittivity is inconsequential.

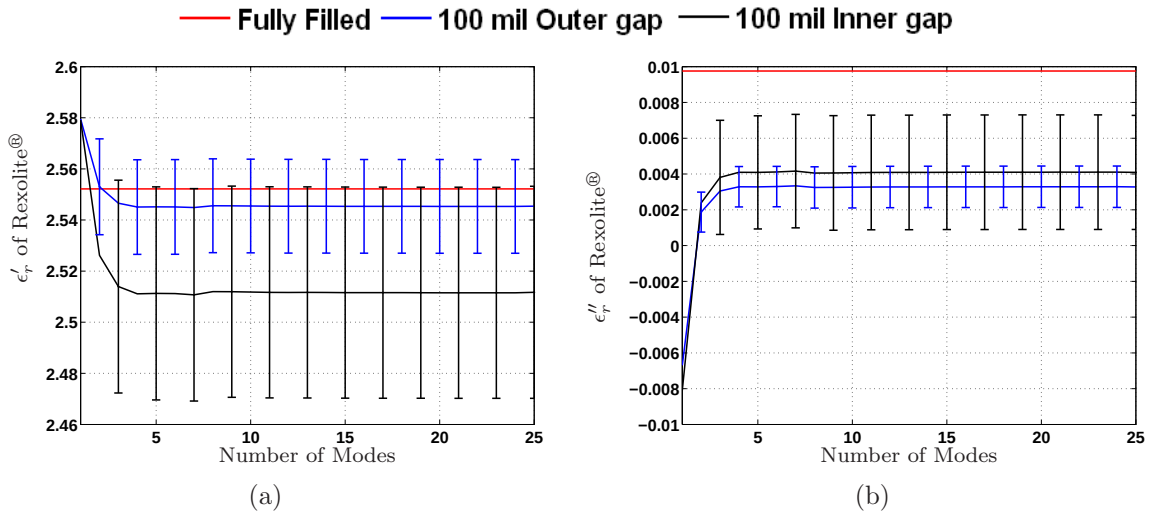

Figure 4.5: Measured permittivity at 2 GHz shown as $\epsilon_r = \epsilon'_r - j\epsilon''_r$. Error bars indicate potential error in radial width (±2 mil) and sample length (±2 mil) measurements. Increasing the number of modes does not impact the error from radial width and length measurments. For low loss, low dielectric constant Rexolite®, the results converge with 10 modes.

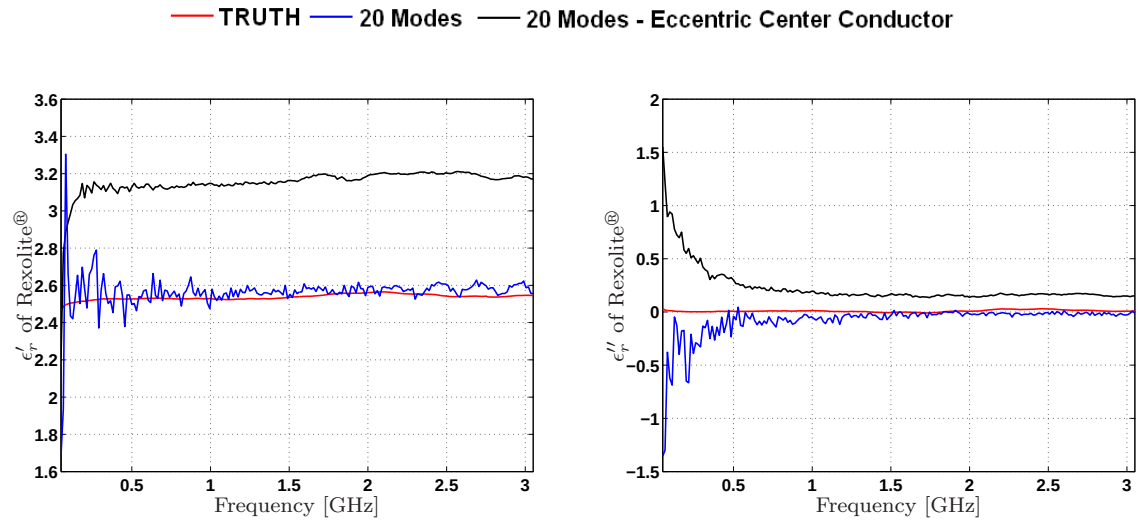

(a) (b)

Figure 4.6: Calculated permittivity for a Rexolite® sample 29.25 mil thick (400 mil outer air gap) using 20 modes and shown as $\epsilon_r = \epsilon_r' - j\epsilon_r''$. An eccentric center conductor will excite non-axially symmetric higher order modes that are not accounted for in this development. Extra support was added to ensure the center conductor remained along the center axis of the coaxial line so that only axially symmetric modes were excited.

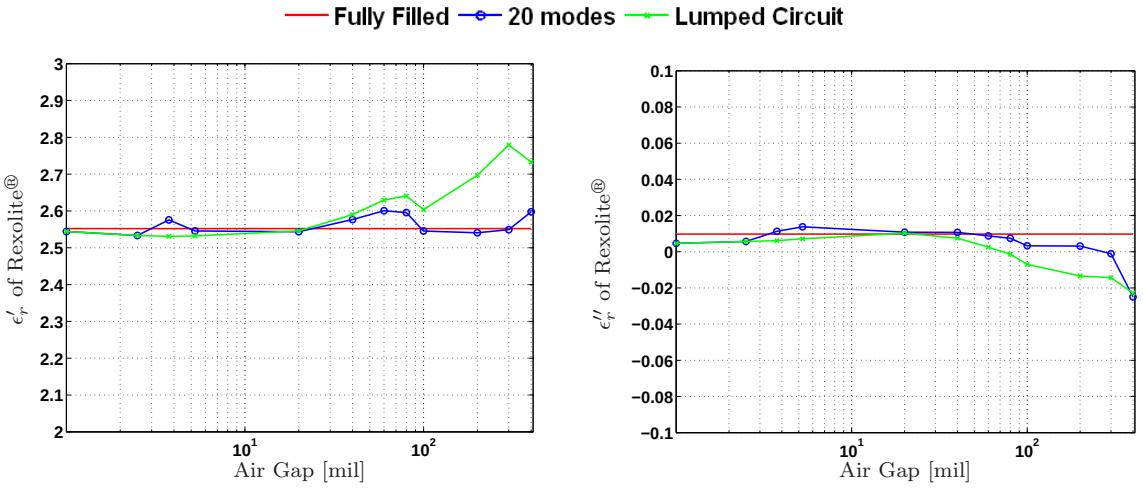

(a) (b)

Figure 4.7: Calculated permittivity for a Rexolite® shown as $\epsilon_r = \epsilon_r' - j\epsilon_r''$. Measurements are at 2 GHz. The outer air gap is varied (by using multiple samples) from 1 mil to 400 mil. The lumped circuit is shown for comparison.

to the theory presented here. Wavenumbers for higher order fields in the Rexolite® samples were exclusively real due to the measurement frequency band. The lossy nature of the MagRAM material insures the higher order wavenumbers are complex and, as mentioned previously, the real part grows as the imaginary part shrinks significantly. The Bessel functions must be very accurate. As seen in figure 4.15, the wave numbers calculated for the MagRAM material are non-physical beyond 25 modes. A more stable Bessel calculation is expected to address this potential source of error. The effects are discussed further in section 4.4.2.

Thirdly, the coaxial is not a perfect conductor, but is assumed to be such. If the actual conductivity of the conductor is used in the development, the boundary conditions, and therefore the fields, are different than those used in this research. The effect will be particularly pronounced at lower frequencies. Exploring these effects is worthwhile, but outside the scope of this research.

The fourth most likely cause of the error in the permittivity is inhomogeneity of the MagRAM sample. Care was taken in cutting samples from MagRAM sheets, but it is not unlikely that, with such a heavily loaded material, the samples may be of different dielectric composition.

The accurate and stable measurement of the permeability is particularly notably. An outer gap scenario is the most accurate, as mentioned previously, but both air gap scenarios shown in figure 4.8 provide good results for permeability over the measurement frequency. Figure 4.10 indicates the permeability results are also very stable with respect to the number of modes included in the analysis. The magnetic field, H_ϕ, is continuous across the material air gap boundary as shown in figure 2.11. This is required by tangential boundary conditions. As such, the H_ϕ field and therefore the results are not as sensitive to modest variations in the permeability.

Error caused by uncertainty in the sample length measurement is largely overshadowed by error from uncertainty in the radial width measurement in figure 4.9.

The effect is identical to that described for the Rexolite® material, but is significantly enhanced due to the heavy dielectric loading in the MagRAM sample.

The permittivity results converge fairly rapidly although not as quickly as the Rexolite® results, with the largest gains within the first 10 modes (figure 4.10). The boundary conditions require a discontinuous E_ρ field across the material to air gap boundary and the characteristic equation, (3.21), is largely dependent on this discontinuity. Viewed from a field perspective, the higher order fields that are excited do not decay as rapidly in the heavily loaded MagRAM as in the Rexolite® samples (evident by comparison of the wavenumbers in table 2.2 and 2.3). Hence, the inclusion of higher order fields is important to accurately determining the permittivity.

Modal method performance for different gap sizes was tested as well. In total, 8 MagRAM samples were machined to produce outer and inner gaps of 3, 6, 9, and 12 mils. The modal method is able to accurately calculate the permittivity for each outer air gap size, shown in figure 4.11. The modal method applied to inner air gaps (not shown), produced similar results for all the gap sizes.

The lumped circuit correction again is a good confidence metric for the modal method. The lump circuit correction results, compared in figure 4.11, have the same behavior and similar values.

4.4 Root Search Algorithm Performance

This research uses both Newton and Muller root searches. The Newton root search essentially follows linear paths looking for the smallest value on a line (1D) or surface (2D). The Newton root search only requires a single initial guess for each variable. A Muller root search is similar to the Newton method, but uses inverse quadratic interpolation rather than a linear interpolation [18]. The Muller root search was used when the roots of an equation might be in close proximity and therefore small, non-linear interpolations were necessary to ensure the appropriate root was found.

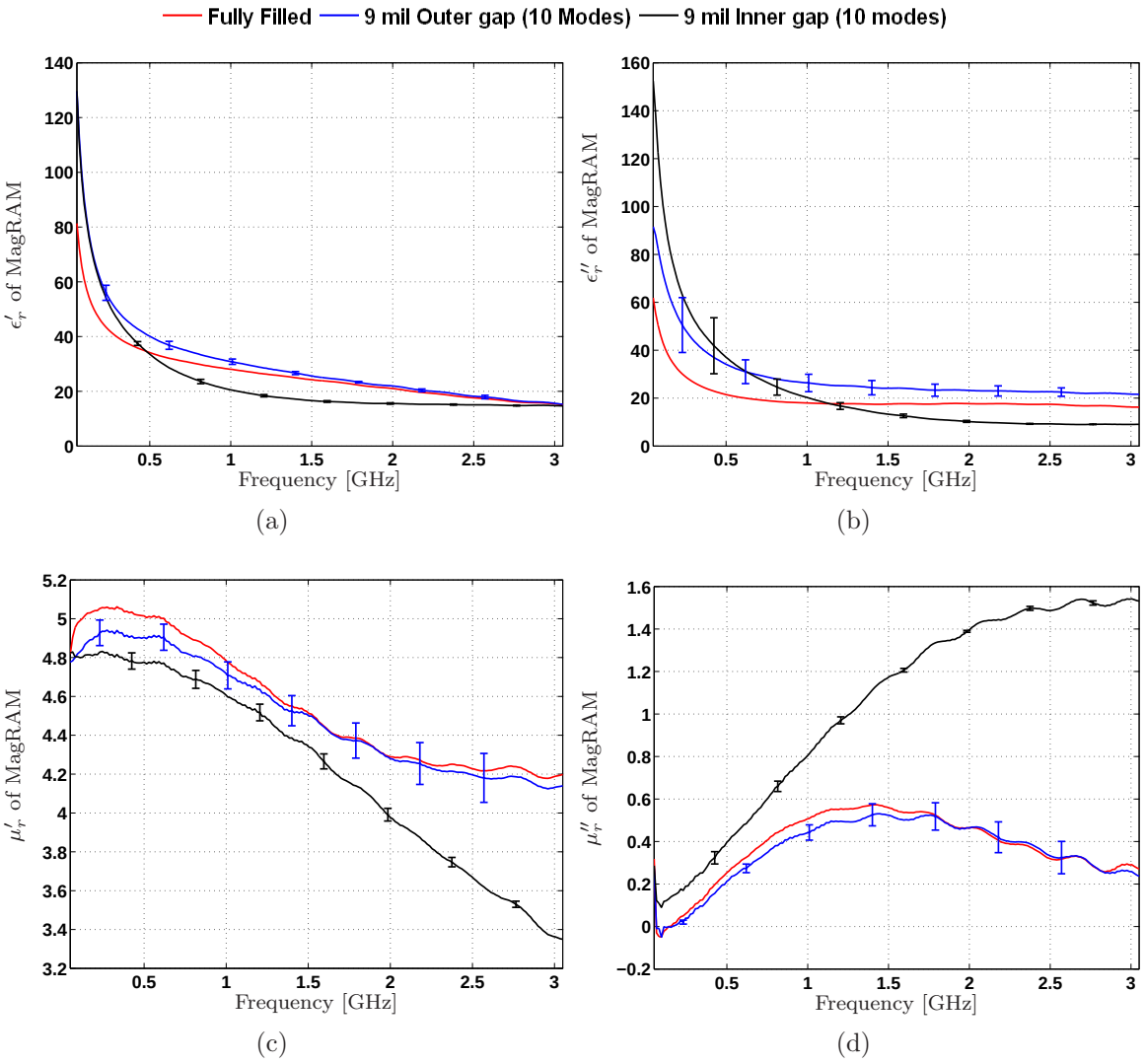

Figure 4.8: Measured permittivity and permeability of MagRAM are shown as $\epsilon_r = \epsilon_r' - j\epsilon_r''$ and $\mu_r = \mu_r' - j\mu_r''$, repectively. Error bars indicate potential error in radial width (± 2 mil) and length (± 2 mil) measurements. Using the modal method with 10 modes considered produces a very accurate correction for the real (a) and imaginary (b) part of the permittivity and real (c) and imaginary (d) part of the permeability.

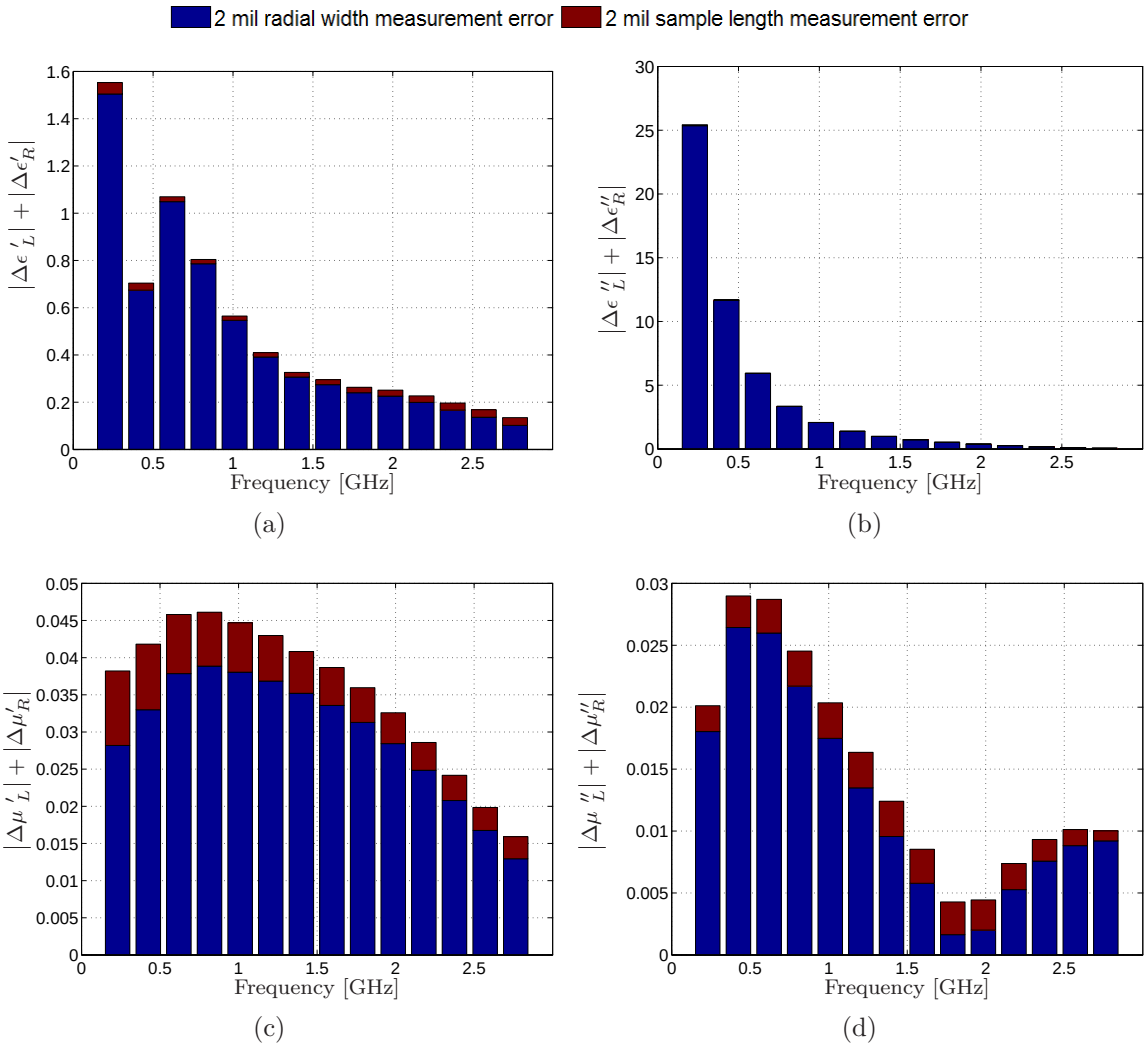

Figure 4.9: Measured permittivity and permeability of MagRAM are shown as $\epsilon_r = \epsilon'_r - j\epsilon''_r$ and $\mu_r = \mu'_r - j\mu''_r$, repectively. Error bars indicate potential error in radial width ($\pm$2 mil) and length ($\pm$2 mil) measurements. Using the modal method with 10 modes considered produces a very accurate correction for the real (a) and imaginary (b) part of the permittivity and real (c) and imaginary (d) part of the permeability.

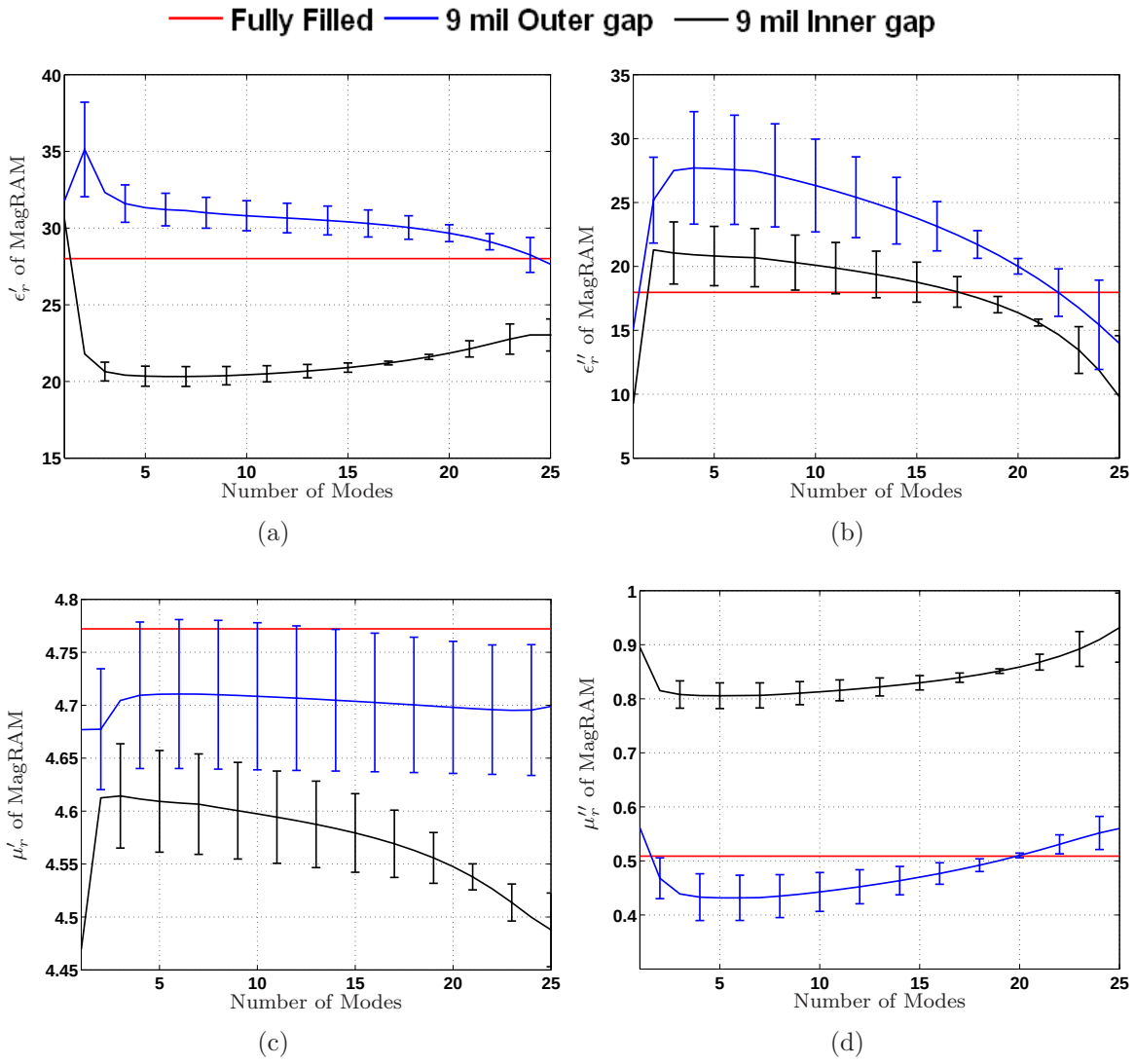

Figure 4.10: Calculated permittivity and permeability of MagRAM are shown as $\epsilon_r = \epsilon_r' - j\epsilon_r''$ and $\mu_r = \mu_r' - j\mu_r''$, repectively. Error bars indicate potential error in sample radial width (± 2 mil) and length (± 2 mil) measurements. Results are for measurements at 1 GHz and increasing number of modes. The measurements are reasonable, but appear to diverge after 20 modes.

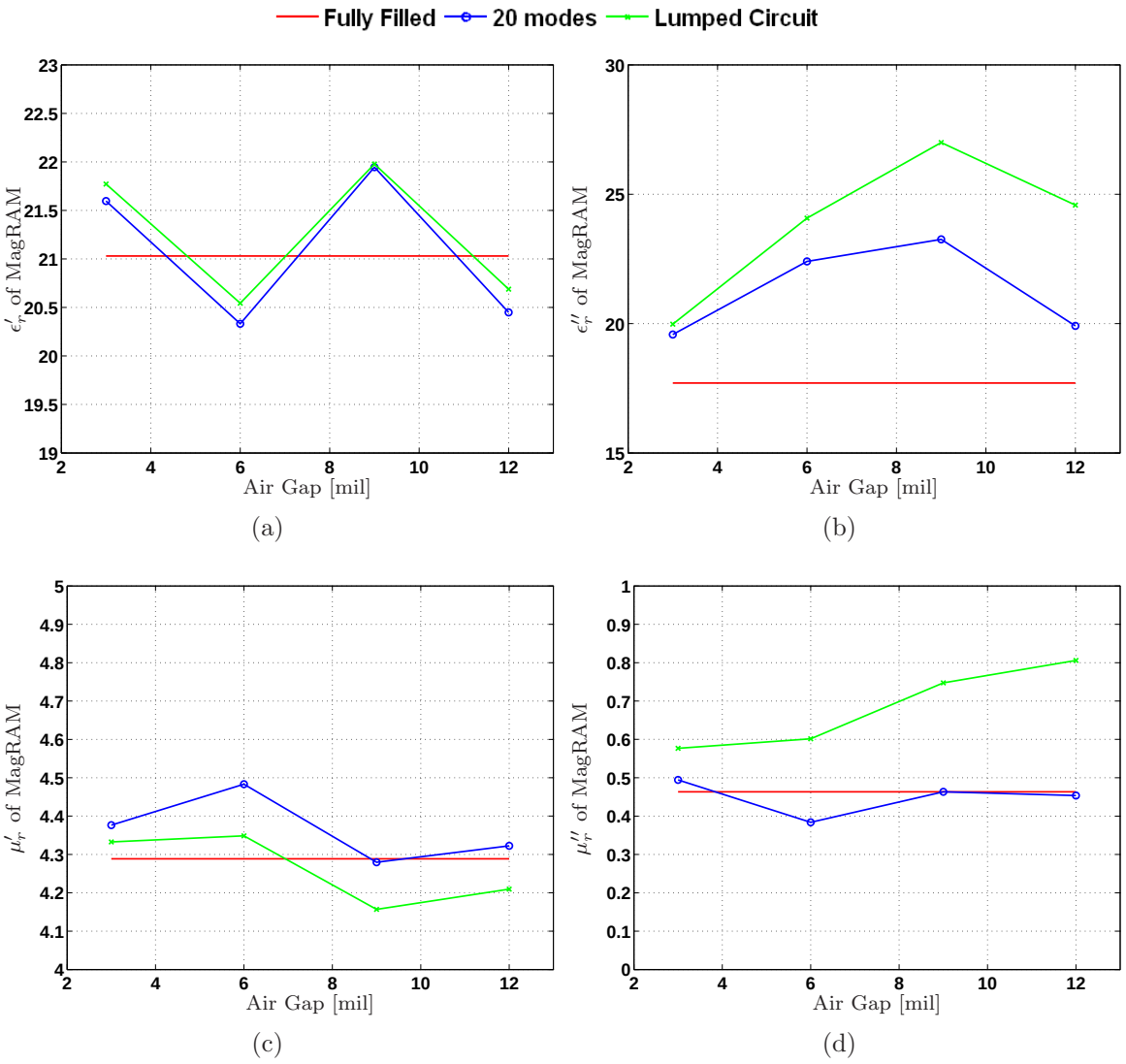

Figure 4.11: Calculated permittivity and permeability of MagRAM are shown as $\epsilon_r = \epsilon_r' - j\epsilon_r''$ and $\mu_r = \mu_r' - j\mu_r''$, repectively. The outer air gap is varied (by using multiple samples) from 3 mil to 12 mil. The lumped circuit is shown for comparison.

Applying both root search methods to a complex valued system, $\epsilon' - j\epsilon''$ for example, introduces another degree of freedom to the root search as both the real and imaginary parts are variable. Both root search methods test the magnitude of the difference in sequential steps in the interpolation, thereby removing the additional degree of freedom when determining convergence.

A complex value root search may produce non-physical results for very low loss or lossless materials. For example, ϵ_r'' is defined to always be positive, thereby matching the physical system. The root search in this research was not constrained to this physical expectation. In testing for convergence, the threshold provided by the user may by reached when the imaginary part of the permittivity is very small, but negative. Therefore, very small ($< .05$) negative values of ϵ_r'' are reported on occasion. Allowing the algorithm results to vary unconstrained provides a good check of the algorithm. If the value of ϵ_r'', for example, becomes very negative, it is a visual indication that either the model assumptions were violated or the algorithm is not performing correctly.

4.4.1 Newton Root Search for Minimization. A Newton root search was used to perform the minimization in (4.1). An accurate initial guess is always a concern when using a Newton root search. In this application, the user is expected to have a reasonable guess for the permittivity and permeability of the material being measured. If multiple roots exist in (4.1), the Newton root search may find the wrong root if the initial guess is not close enough to the actual value. For the non-magnetic Rexolite® material with a 100 mil outer air gap, the magnitude of the difference between the theoretical and experimental S_{21} were evaluated and plotted (figure 4.12) in a complex region immediately surrounding the expected permittivity to look for potential multiple roots for both 1 mode and 10 mode solutions[2]. No extra roots were noted in either S_{21} or S_{11} plots and there is little difference in the regions calculated

[2]For non-magnetic material, $\mu_r = 1$ is assumed. Therefore, only a one dimension root search is needed using either S_{21} or S_{11}.

using 1 mode versus 10 modes with the exception that the solution is shifted more toward the actual value (as expected when increasing the number of modes). This indicates that, for a non-magnetic material, only a reasonable initial guess is necessary.

Analyzing the Newton root search's sensitivity to an initial guess is more difficult when magnetic material is evaluated. A two dimensional root search is used and hence the permittivity and permeability are iterated with (4.1). The simple plots produced for Rexolite® are not possible. Rather an empirical analysis is more appropriate and understandable. Initial guesses of $\epsilon_r = 1 - 1j$ and $\mu_r = 1 - 1j$ produced the same result as a more accurate initial guess. It must be noted that, for the sake of efficiency and accuracy, the initial guess is only used to find the first values of ϵ_r and μ_r for the material. Calculations for the next higher frequency use as the initial guess the result from the previous frequency. This technique assumes the permittivity and permeability do not change rapidly with frequency.

The Newton root search is appropriate for evaluating (4.1). The roots are distinct and separated. Provided the initial guess is reasonable, the Newton algorithm converged to the necessary root.

4.4.2 Muller Root Search for Wavenumbers. Determining the wavenumbers in Region II of the coaxial test fixture is the primary and most critical calculation in the modal method. The wavenumbers are determined by finding the roots of (3.21), reprinted here as

$$k_{\rho_{1n}} Z_{1n}\ V_0\left(k_{\rho_{1n}} R\right)\ W_1\left(k_{\rho_{2n}} R\right) - k_{\rho_{2n}} Z_{2n}\ V_1\left(k_{\rho_{1n}} R\right)\ W_0\left(k_{\rho_{2n}} R\right) = 0 \tag{4.2}$$

The oscillatory nature of the Bessel functions guarantees an infinite number of roots that must be determined in sequential order. In the case of heavily loaded materials, the first roots in the sequence are often in close proximity to each other. For this reason, a Muller root search method was used to ensure the proper root was located in sequential order [18].

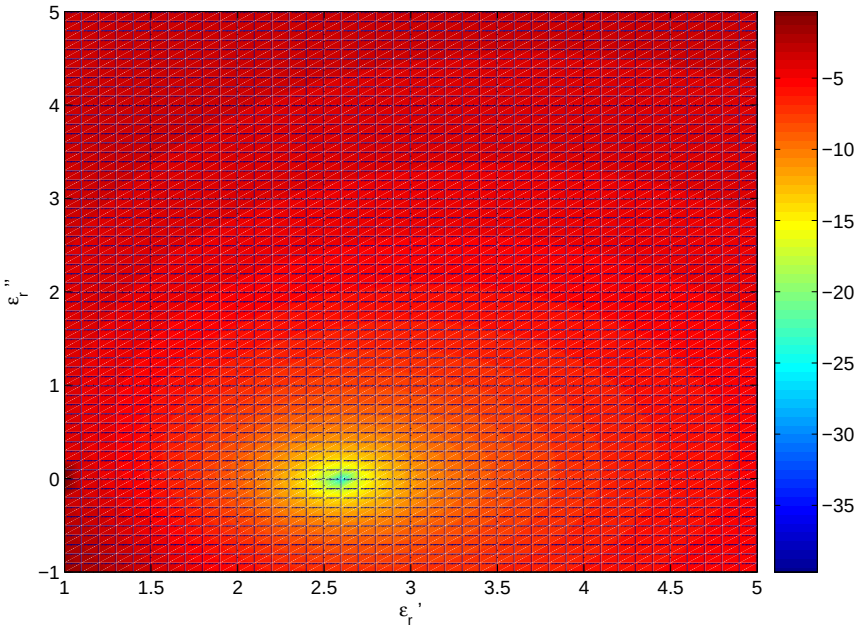

(a)

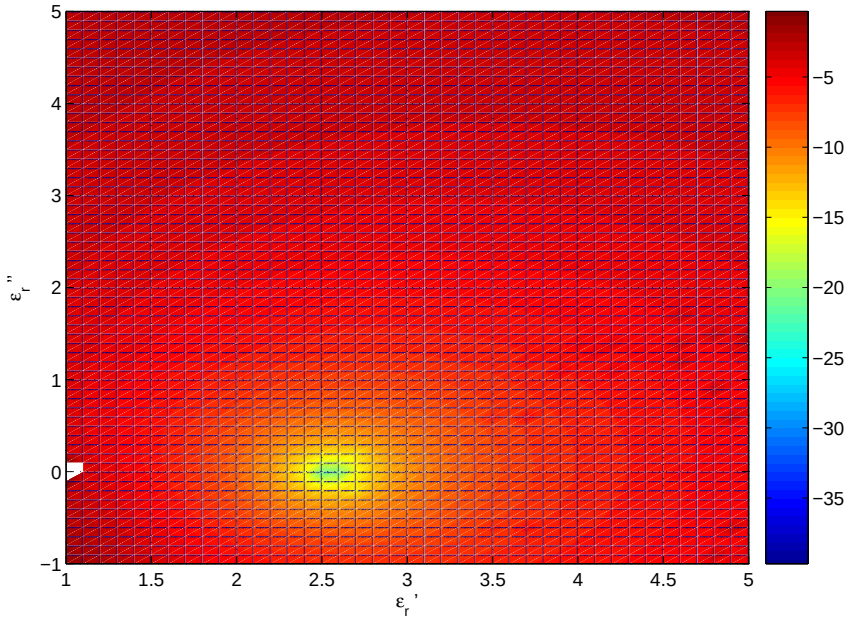

(b)

Figure 4.12: For a Rexolite® sample with 100 mil outer air gap, the magnitude, in dB, of the difference between the theoretical and experimentally measured S_{21} parameter is plotted as a complex surface around the expected solution of $\epsilon_r = 2.525$. The smallest value on the surface (blue) is the solution of the matrix (and hence the permittivity of the material). A single root is apparent for the modal method using 1 mode (a) and 10 modes (b). Similar results were noted for the S_{11} parameter.

The Muller root search method requires three initial guesses. The roots of (4.2) vary based on material parameters, air gap size, test fixture dimensions, and frequency. For low frequency measurements of low-loss, low dielectric constant material such as Rexolite®, the initial guess of the roots of (4.2) is sufficiently estimated with the roots of (3.20), the fully filled coaxial line case. Table 2.2 validates this assumption. There is very little difference between the filled and air gap wavenumbers.

Wavenumbers for a heavily loaded material may be significantly different between a filled and air gap scenario, even for small air gaps as shown in table 2.3 and figure 4.13. An initial guess in this case is extremely important. For heavily-loaded MagRAM, the initial guess was calculated based on asymptotic expansions for (4.2) at the lowest measurement frequency, 50 MHz. The frequency was increased incrementally by 15 MHz steps, tracking the root at each step, until the desired frequency was reached shown in figure 4.13.

Initial guesses for $\tilde{\gamma}_n$ for high frequency and heavily loaded material samples are made with asymptotic expansions as $\tilde{\gamma}_n$ goes to ∞. Large argument approximations of Bessel functions are well-known [1] as

$$\begin{aligned} J_n(z) &= \sqrt{\frac{2}{\pi z}} \cos\left[z - \left(n + \frac{1}{2}\right)\frac{\pi}{2}\right] \\ Y_n(z) &= \sqrt{\frac{2}{\pi z}} \sin\left[z - \left(n + \frac{1}{2}\right)\frac{\pi}{2}\right] \end{aligned}$$

for $8z >> 4n^2 - 1$. Substituting into (4.2) and reducing produces a large argument approximation as

$$\frac{\sqrt{\tilde{\gamma}_n^2 + k_1^2}}{\epsilon_{r1}} \tan\left(\sqrt{\tilde{\gamma}_n^2 + k_1^2}(R - a)\right) + \frac{\sqrt{\tilde{\gamma}_n^2 + k_2^2}}{\epsilon_{r2}} \tan\left(\sqrt{\tilde{\gamma}_n^2 + k_2^2}(b - R)\right) = 0 \quad (4.3)$$

The tangent function is not considered stable based on its divergence at multiples of $\frac{\pi}{2}$, but that fact is utilized in estimating the roots. A heavily loaded material

produces a high contrast between the air gap and the material (i.e. for an outer air gap $k_1 >> k_2$). Additionally, considering the small air gaps used in this research, the radial width of the air gap is significantly smaller than the radial width of the material (i.e. for an outer gap $(b-R) << (R-a)$). The tangent function arguments

$$\theta_n = \sqrt{\tilde{\gamma}_n^2 + k_1^2}(R-a) \tag{4.4}$$

$$\phi_n = \sqrt{\tilde{\gamma}_n^2 + k_2^2}(b-R) \tag{4.5}$$

and the tangent function weights are therefore significantly different, are related via $\tilde{\gamma}_n$, and ensure the two tangent functions are separated in magnitude and phase. The large difference in magnitude requires that the roots of 4.3 are at points very near to poles of the tangent functions such that large $\tilde{\gamma}_n$ is estimated reasonably well as

$$\tilde{\gamma}_n^2 = \left(\frac{\theta_n}{R-a}\right)^2 - k_1^2 \tag{4.6}$$

$$\tilde{\gamma}_n^2 = \left(\frac{\phi_n}{b-R}\right)^2 - k_2^2 \tag{4.7}$$

where $\phi_n = \frac{\pi}{2} + n\pi$ and $\theta_n = \frac{\pi}{2} + n\pi$. The gamma estimate must be based on the material properties and thus (4.6) is used for outer air gap gamma estimates and (4.7) for inner air gaps.

The first root of 4.2 at low frequencies for the heavily loaded MagRAM falls far below the criteria for a large argument. Therefore, a small argument approximation (table F.1) is used to reduce (4.2) to

$$\tilde{\gamma}^2 = \frac{\Omega k_1^2 - k_2^2}{1-\Omega} \tag{4.8}$$

where

$$\Omega = \frac{-\epsilon_{r2} \ln\left(\frac{R}{a}\right)}{\epsilon_{r1} \ln\left(\frac{b}{R}\right)} \tag{4.9}$$

The n subscript is absent. Only the principle value of the small argument approximation for $Y_n(z)$ is used (where z is complex). The small argument approximation

provides an initial guess for the first zero of (4.2) at low frequency with a heavily loaded material and therefore multiple values are not needed.

The initial guesses for $\tilde{\gamma}_n$ calculated from asymptotic techniques, in conjunction with the Muller root search method, are able to quickly and accurately find the actual value of $\tilde{\gamma}_n$. Figure 4.14 is a complex surface of values calculated via (4.2) for varying values of $\tilde{\gamma}_n$ at 2GHz for a coaxial line fully filled with MagRAM (a) and a coaxial line with MagRAM having a 9 mil inner air gap (b). The inner air gap case is used because it proved to be the most difficult to track over frequency. The first four wavenumbers determined by the Muller method and the complex path the Muller method took to find the root are both shown. The lowest magnitudes in the plot (blues spots) are the actual roots the Muller method is attempting to locate. Although the roots are significantly different from the no gap to 9 mil inner air gap case, with the proper initial guess the Muller method quickly locates the roots. This is true despite the decrease in gradient between successive roots in the 9 mil inner air gap case in comparison to the no air gap case.

The accuracy of the Bessel function calculations are critical in determining $\tilde{\gamma}_n$ from (4.2). The Matlab® software package was used to implement all of the routines required for this research. The native Bessel functions were used. The first 50 wave numbers for a MagRAM material with 9 mil inner air gap at 50MHz were calculated and are plotted in figure 4.15. The initial guess, γ_n^{est}, is also plotted. It appears that (4.2) is being approximated by a tangent function for the higher order modes (large argument). This is consistent with the large argument approximation used in the derivation of initial guesses, implying that the large argument approximations are being used in the software package when calculating Bessel functions. Based on the figure, including more than 23 modes is counter productive and, not knowing at what point the argument is large enough that the software package begins to approximate the Bessel function, including more than 15 modes may alter the outcome for complex $\tilde{\gamma}_n$. This is evident in the modal method results for MagRAM (figure 4.10), but not in the results for Rexolite®. This implies that the approximation is embedded in

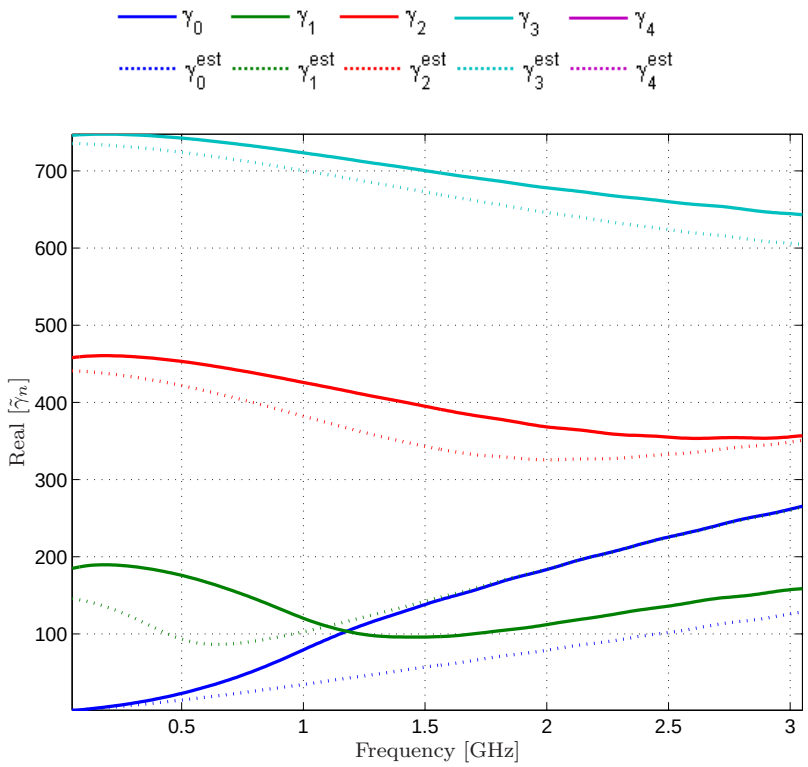

(a)

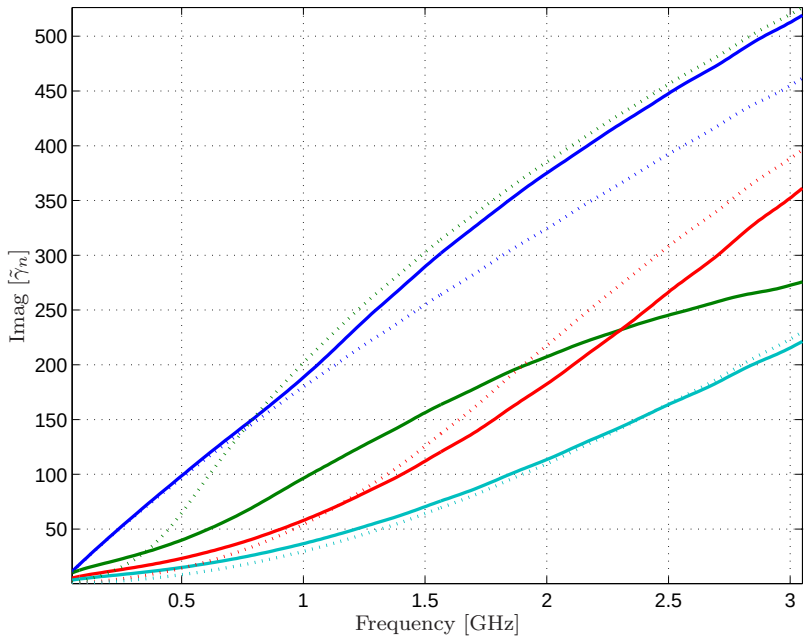

(b)

Figure 4.13: The real (a) and imaginary (b) parts of the wavenumber, $\tilde{\gamma}_n$, for the first four modes, TM_{0n}, as a function of frequency. The initial guesses, estimated using asymptotic techniques, are shown. For $\tilde{\gamma}_0$, the initial guess begins to diverge from the actual value at 500 MHz.

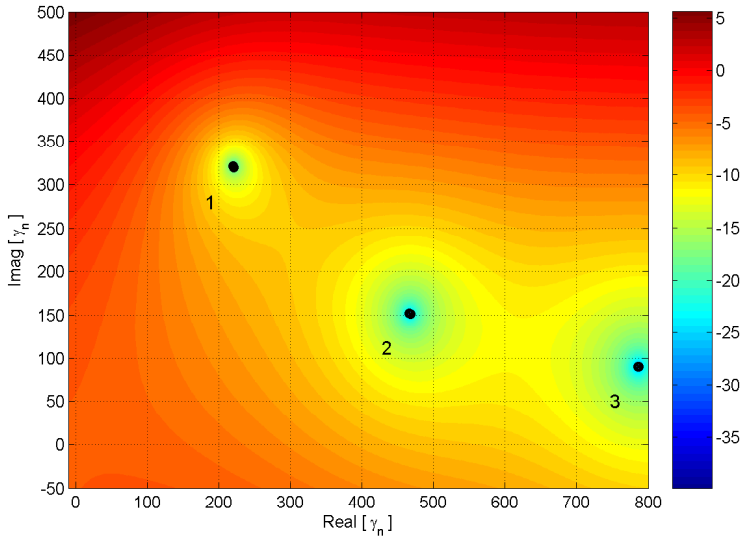

(a)

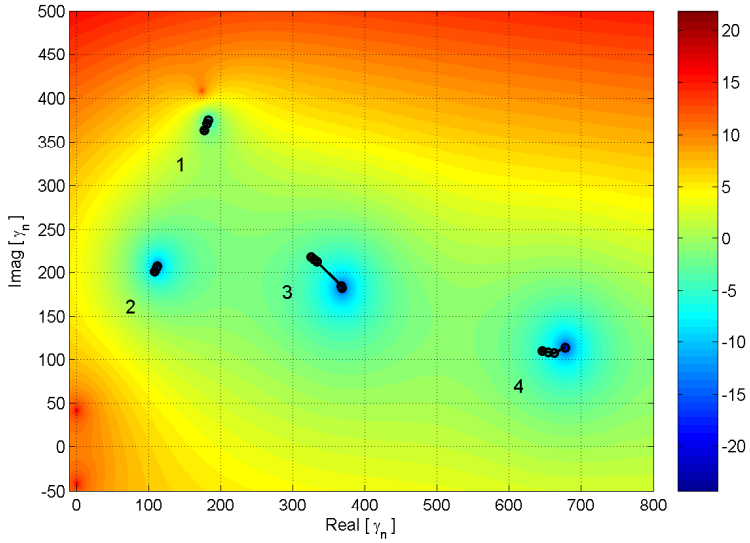

(b)

Figure 4.14: The potential solutions to the characteristic equations for a fully filled (a) and air gap (b) coaxial line plotted as a complex plane. The Muller root search locates the lowest point on the surface (the blue areas). The frequency is 2 GHz for these plots. When the MagRAM fully fills the coaxial line the wavenumbers are visually sequential and, with an accurate initial guess, are found quickly. Conversely, when an air gap is present, $\tilde{\gamma}_n$ is not necessarily sequential and the gradient between successive wavenumbers is shallower, implying a more accurate initial guess is critical. The first four wavenumbers and the search path followed by the Muller root finding method are labeled on the graphs.

the native Bessel functions when the large argument is complex (the MagRAM case), but not for purely real (as in the Rexolite® case). This requires further research to validate.

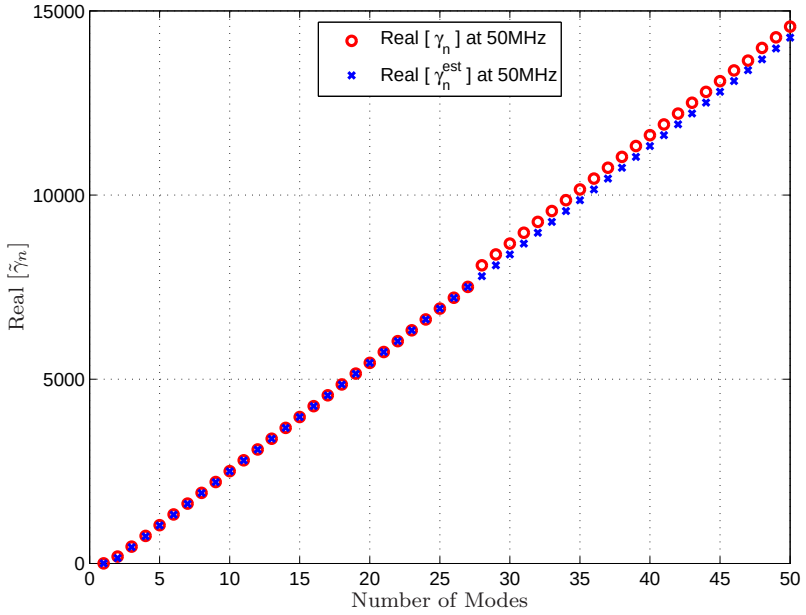

(a)

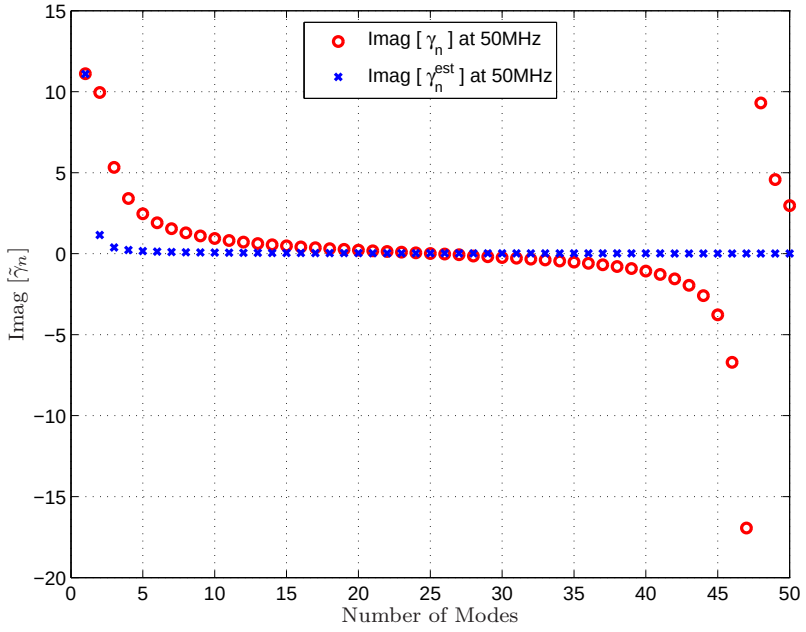

(b)

Figure 4.15: The real (a) and imaginary (b) parts of the wavenumbers , $\tilde{\gamma}_n$, for $n = 0, 2, \ldots, 49$ at 50MHz. Wavenumbers > 23 are non-physical in that the imaginary part is < 0. Note the initial guesses, γ_n^{est}, remain physical at higher order modes, but the located roots appear to follow a tangent function.

V. Conclusions and Recommendations for Improvement

The excitation of higher order modes is a major source of error in material characterization measurements using the NRW algorithm. Higher order modes in coaxial line measurements are typically caused by axially symmetric air gaps between the material sample and the inner or outer conductor. A modal method was developed assuming axially symmetric modes are excited. The method was proven to remove error associated only with axially symmetric modes. One property of the modal method is the convergence of the result to the actual material properteris as the number of modes are increased, provided the only significant measurement error is from axially symmetric higher order mode excitation. This is in contrast to the lumped circuit correction factor that weights the NRW result based on material and air gap dimensions. The weighting, although fairly accurate, does not provide confidence in the solution, particularly for heavily loaded materials.

5.1 Recommended Improvements

The shortcomings of the modal method developed here and potential ways to account for them are described here.

5.1.1 Initial Guesses for Wavenumbers. Using large and small argument approximations for Bessel functions proved very valuable for estimating the wavenumbers in heavily loaded MagRAM with air gaps considered in this research. The method is simplified at best and would benefit greatly from a more thorough exploration and mathematical analysis. The wavenumbers are extremely important and as such the initial guesses are a critical component of the modal method.

5.1.2 Compensation for Eccentric Center Conductor. A properly machined sample that fully fills the cross-section of the coaxial line (i.e. no air gap) physically supports the center conductor in the center of the waveguide. As shown, if the sample, when measured, has either an inner or outer air gap the physical support that keeps the center conductor on the center axis of the coaxial line is gone (see figure 5.1). In

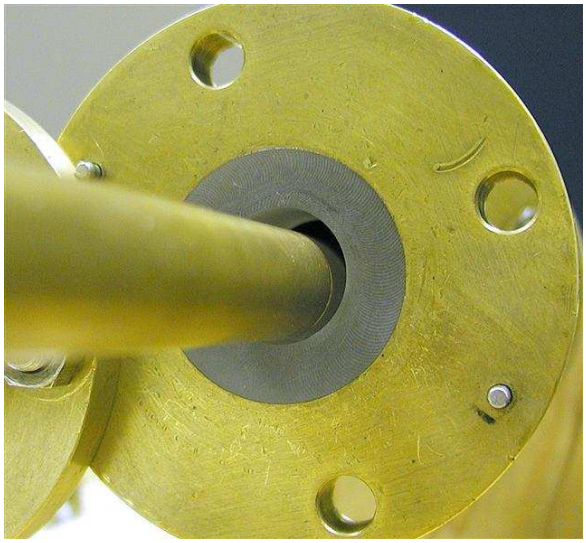

Figure 5.1: The physical support provided by a sample that fully fills the coaxial line is lost when an air gap is present. More physical support to the conductor, a different mathematical model, or a combination are needed to overcome the effect on measurements.

the case of an outer air gap, not only is the outer support removed, but the sample puts additional weight on the center conductor. This research assumed a center conductor that remained along the center axis when an air gap was present and therefore only axially symmetric modes were excited. Additional supports are necessary within the coaxial line to ensure the center conductor remained in the center. However, given the dimensions in figure 5.2, for a small droop, d, a perturbation analysis of the fields in the material and air gap region could be performed to produce a modified propagation constant, $\tilde{\gamma}_n$, for use in the modal algorithm defined in this research.

5.1.3 Compensation for Eccentric Material. The presence of an inner and outer air gap in the material region was not addressed by this research. Assuming the coaxial center conductor does not droop, an inner and outer air gap will produce the scenario shown in figure 5.3. Note that for a small inner radius of the material, r_1, the droop, d, will be small and a perturbation analysis similar to the previous section could be accomplished. However, as d increases the field modes are less axially symmetric. For a significant d, a rigorous means of determining $\tilde{\gamma}_n$ is found via

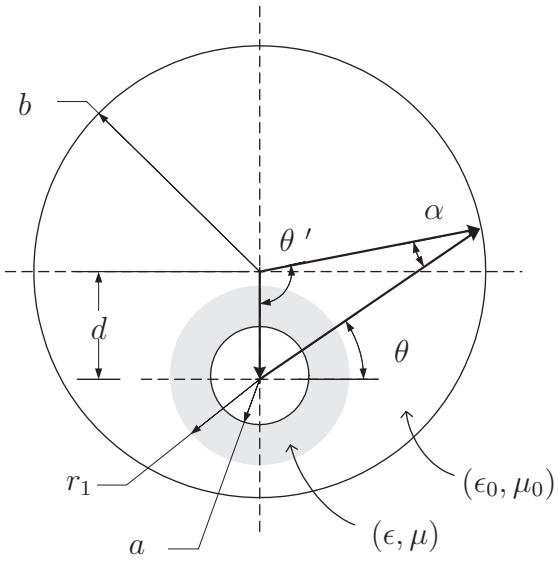

Figure 5.2: An air gap in the measurement reduces the physical support to the center conductor. Higher order modes that are not axially symmetric may be excited. The dimensions, particularly the droop, d, are exaggerated in the drawing for clarity.

the addition theorem of Bessel functions. The addition theorem translates the field definitions from the origin of the material to the origin of the conductors (or vice versa). The application of the addition theorem involves another truncated series and significantly more terms to calculate. This method has previously been applied to determining the wavenumbers for eccentric center conductors [13], [19] and eccentric circular dielectric rods [20]. With this method, a single sample could be machined that could be measured at room temperature as well as higher temperatures (provided the conductors did not expand to the point of applying excessive pressure on the sample). Beyond the mathematical difficulty in applying the addition theorem, there is also the physical difficulty of measuring the dimensions r_1, r_2, a, b, and d as the sample and conductor are heated. A method must be devised to accurately measure these dimensions during the testing process or a good estimate provided.

5.1.4 Impedance Boundary Conditions. The coaxial test fixture inner and outer conductors are assumed to be PEC ($\sigma \to \infty$). Considering the electric field will

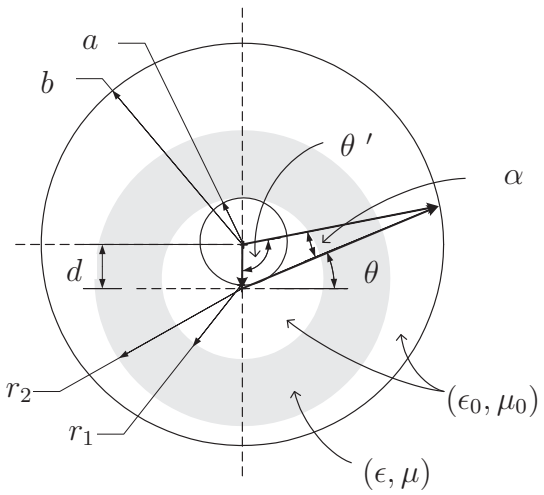

Figure 5.3: An air gap in the measurement reduces the physical support to the center conductor. Higher order modes that are not axially symmetric may be excited. The dimensions, particularly the droop, d, are exaggerated in the drawing for clarity.

penetrate the conducting walls like

$$\delta = \sqrt{\frac{2}{\omega\mu\sigma}}$$

when σ is finite, but large, and the frequency ,ω, is large, the electric field within the conductors are easily approximated as zero. However, as the frequency decreases and σ remains finite, the electric field will begin to penetrate the conducting walls and power will be dissipated in the walls based on $\mathbf{S} = \mathbf{E} \times \mathbf{H}^*$. The tangential electric field, $\mathbf{E}_z$ for a TM^z_{0n} mode, must remain continuous across the boundary, $\hat{n} \times \mathbf{E}_1 = \hat{n} \times \mathbf{E}_2$, and therefore the electric field penetration of the conducting wall and the subsequent attenuation has a direct impact on the intensity of the fields within the waveguide. The effect is seen by making measurements without a sample present. The result is expected to be equivalent to the properties of freespace, but figure 5.4 shows the loss of the coaxial line is more noticeable at lower frequencies. This impacts the accuracy of the measurements as evident in the low frequency regimes of the data presented in this research. The effect is expected to be more pronounced as the loading of the material increases. Reformulating the results of this research

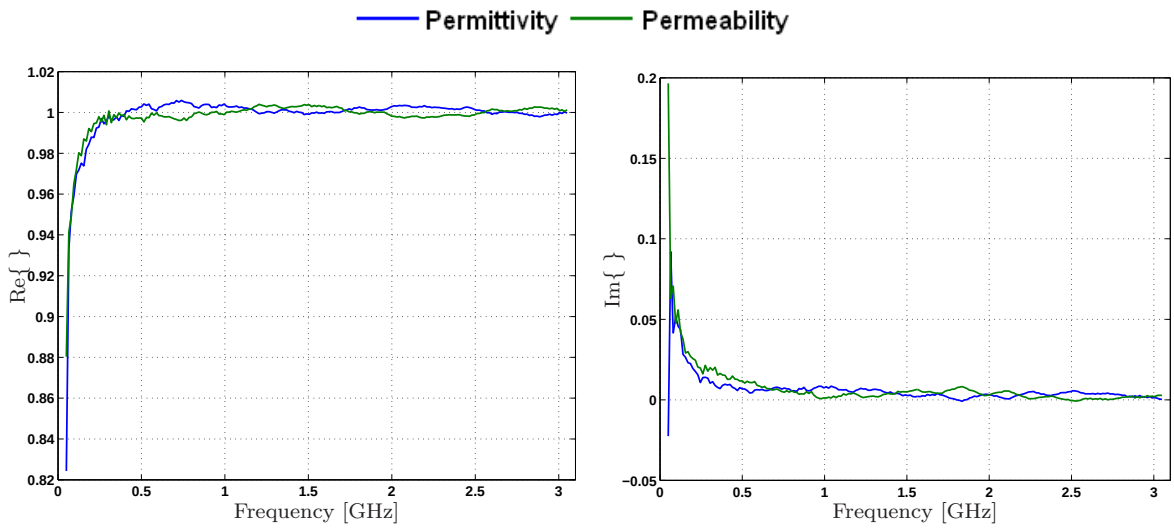

(a) (b)

Figure 5.4: The measured real (a) and imaginary (b) part of the permittivity and permeability for the coaxial test line when no sample is present. The result should be that of freespace ($\epsilon_r = 1$, $\mu_r = 1$). The low frequency perturbations are likely due to the finite impedance of the coaxial line.

using impedance boundary conditions is expected to improve the accuracy of lower frequency measurements in the coaxial test fixture.

5.1.5 Time Domain Analysis of Scattering Parameters. The generally large difference between sequential wavenumbers provides an excellent opportunity to analyze the scattering of individual modes. In time, each mode will propagate at a different rate based on the group velocity, as a function of the wavenumber. Sampling the fields in time or increasing the frequency bandwidth of the measurement should allow the different propagating modes to be identifiable such that they could be treated individually in the modal matrix. The first non-axially symmetric TM mode is TM^z_{11} with a cutoff frequency at 14 GHz in a free space filled coax line (see table 2.1). This offers a potential four fold increase in measurement bandwidth (assuming a pure TEM excitation).

5.1.6 Non-linear Least Squares Algorithm for Minimization. The Newton root search is performed well for this research, but is not the only algorithm available

to accomplish the minimization of (3.1). Previous research has used a non-linear least squares algorithm to minimize the difference between theoretical and measured scattering parameters. One advantage is the use of all four scattering parameters, S_{11}^{exp}, S_{22}^{exp}, S_{21}^{exp}, and S_{12}^{exp}, in the process. For a simple material and good forward and reverse measurements, the inclusion of all four scattering parameters is expected to stabilize the results.

5.1.7 Efficiency in calculation of Bessel Functions. Matlab® is not designed for computational efficiency and the computation of Bessel functions are no exception. Two dimension root searches using 10 modes, particularly for magnetic materials, easily took 5-6 hours to evaluate. The primary calculations responsible for the amount of time are the Bessel functions. For this research to be practical in a testing environment, the code must be ported to a language that supports very fast calculation of Bessel functions (i.e. Fortran®).

Appendix A. Wave Equation

Maxwell's Equations are a collection of experimentally derived, mathematical descriptions for electromagnetic waves. In time-harmonic (frequency domain) form they are given as

$$\nabla \times \mathbf{E} = -j\omega\mathbf{B} \qquad \text{Faraday's Law} \tag{A.1}$$

$$\nabla \times \mathbf{H} = \mathbf{J} + j\omega\mathbf{D} \qquad \text{Ampere's Law} \tag{A.2}$$

$$\nabla \cdot \mathbf{D} = q_e \qquad \text{Gauss's Law for D} \tag{A.3}$$

$$\nabla \cdot \mathbf{B} = 0 \qquad \text{Gauss's Law for B} \tag{A.4}$$

where q_e is the static charge in the system and ω is the radian frequency of the field.

In words, Faraday's law states that an electric field, **E**, rotates around a magnetic flux density, **B**. Ampere's law states that a magnetic field, **H**, rotates around a linear combination of an electric current, **J**, and an electric flux density, **D**. Gauss's Law states that the electric flux density, **D**, diverges from an electric charge and the magnetic flux density, **B**, does not diverge from a magnetic charge, implying that the magnetic field is purely rotational. divergence of a field integrated over a closed surface is equal to the electric or magnetic charge contained within that surface and is applicable to both the electric and magnetic flux densities respectively.

The test setup of network analyzer and coaxial line test fixture are assumed free of static sources. The excitation is generated external to the coaxial line and therefore $q_e^i, \mathbf{J}^i = 0$.

Further, it is assumed that the material is linear, homogeneous, and isotropic and therefore the electric and magnetic flux densities are a function of the material in which the respective fields are applied. The following constitutive relationships

$$\mathbf{D} = \epsilon\mathbf{E} \tag{A.5}$$

$$\mathbf{B} = \mu\mathbf{H} \tag{A.6}$$

are therefore valid within the material where ϵ is the permittivity and μ the permeability of the material.

Maxwell's equations can now be simplified using this assumption. Removing the sources and substituting (A.5) into (A.1) and (A.3), and (A.6) into (A.2) and (A.4) yields

$$\nabla \times \mathbf{E} = -j\omega\mu\mathbf{H} \tag{A.7}$$

$$\nabla \times \mathbf{H} = j\omega\epsilon\,\mathbf{E} \tag{A.8}$$

$$\nabla \cdot \mathbf{E} = 0 \tag{A.9}$$

$$\nabla \cdot \mathbf{H} = 0 \tag{A.10}$$

or specifically a system of coupled, first order partial differential equations.

Although (A.7)-(A.10) completely describe the fields with the coaxial line, the mathematical solution is difficult to determine. The system of equations are simplified and uncoupled by application of vector identities. Applying the curl operation to Faraday's law produces

$$\begin{aligned} \nabla \times (\nabla \times \mathbf{E}) &= \nabla \times (-j\omega\mu\mathbf{H}) \\ &= \nabla(-j\omega\mu) \times \mathbf{H} + (-j\omega\mu)\nabla \times \mathbf{H} \qquad \text{(A.11)} \\ &= -j\omega\mu\,(\nabla \times \mathbf{H}) \qquad \text{(A.12)} \end{aligned}$$

where the RHS is expanded via vector identity [3]

$$\nabla \times (\psi\mathbf{A}) = \nabla\psi \times \mathbf{A} + \psi\nabla \times \mathbf{A}$$

and reduce by recognizing that the gradient of a constant is equal to zero. This form allows substituting (A.8) into (A.12). Additionally using vector identity

$$\nabla \times (\nabla \times \mathbf{A}) = \nabla(\nabla \cdot \mathbf{A}) - \nabla^2\mathbf{A}$$

to expand the LHS of (A.12) and substituting (A.9) produces

$$\nabla(0) - \nabla^2\mathbf{E} \;=\; -j\omega\mu\,(j\omega\epsilon\,\mathbf{E})\,. \tag{A.13}$$

Substituting $k = \omega^2\epsilon\mu$ and rearranging into the standard form of the wave equation

$$\nabla^2\mathbf{E} + k^2\mathbf{E} \;=\; 0 \tag{A.14}$$

is an uncoupled, homogeneous, second-order partial differential equation that describes the behavior of an electric field in general. A similar procedure is accomplished to derive the wave equation as a function of the magnetic field

$$\nabla^2\mathbf{H} + k^2\mathbf{H} \;=\; 0 \tag{A.15}$$

Appendix B. Solution to Helmholtz's Wave Equation in Cylindrical Coordinates

The coaxial line is naturally described in cylindrical coordinates. A solution to Helmoholtz's wave equation [9]

$$\nabla^2\Psi + k^2\Psi = 0 \tag{B.1}$$

for cylindrical coordinates is needed to describe the fields in the coaxial line. Expanded in cylindrical coordinates, (B.1) is

$$\frac{1}{\rho}\frac{\partial}{\partial\rho}\left(\rho\frac{\partial\Psi}{\partial\rho}\right) + \frac{1}{\rho^2}\frac{\partial^2\Psi}{\partial\phi^2} + \frac{\partial^2\Psi}{\partial z^2} + k^2\Psi = 0 \tag{B.2}$$

Assume that the solution Ψ is separable into a product of functions that are dependent on a single coordinate direction (the well-known separation of variables technique [1]) and can therefore be written as

$$\Psi(\rho,\phi,z) = F(\rho)G(\phi)H(z) \tag{B.3}$$

Using (B.3) in (B.2) produces

$$\frac{1}{F\rho}\frac{d}{d\rho}\left(\rho\frac{dF}{d\rho}\right) + \frac{1}{\rho^2}\left(\frac{1}{G}\frac{d^2G}{d\phi^2}\right) + \left(\frac{1}{H}\frac{d^2H}{dz^2}\right) + k^2 = 0 \tag{B.4}$$

The second and third parenthetical terms are dependent only on ϕ and z respectively. For the solution to sum to zero over all space, these terms must also be constant [9]. Therefore, the assignments

$$\frac{1}{G}\frac{d^2G}{d\phi^2} = -m^2 \tag{B.5}$$

$$\frac{1}{H}\frac{d^2H}{dz^2} = -k_z^2 \tag{B.6}$$

are made and substituted into (B.4) resulting in

$$\frac{\rho}{F}\frac{d}{d\rho}\left(\rho\frac{dF}{d\rho}\right) + \left(-m^2\right) + \rho^2\left(-k_z^2\right) + \rho^2k^2 = 0 \tag{B.7}$$

Defining

$$k_\rho^2 = k^2 - k_z^2 \tag{B.8}$$

and rearranging terms, the defining equations (B.5), (B.6), and (B.7) for G, H, and F respectively are

$$\rho\frac{d}{d\rho}\left(\rho\frac{dF}{d\rho}\right) + \left[(k_\rho\rho)^2 - m^2\right]F = 0 \tag{B.9}$$

$$\frac{d^2G}{d\phi^2} + Gm^2 = 0 \tag{B.10}$$

$$\frac{d^2H}{dz^2} + Hk_z^2 = 0 \tag{B.11}$$

of which the solutions are constrained by (B.8).

Equation (B.9) is recognizable as the Bessel differential equation. The general solution will be a linear combination of Bessel functions chosen to best describe the $\hat{\rho}$ directed field in the original problem. For a coaxial line, the field will be a standing wave and therefore the general solution is defined as

$$F(\rho) = AJ_m(k_\rho\rho) + BY_m(k_\rho\rho) \tag{B.12}$$

where J_m is a Bessel function of the first kind with order m and Y_m is a Bessel function of the second kind with order m [9].

Solutions of the ordinary differential equations (B.10) and (B.11) are well-known. The general solutions are chosen based on the description of the original problem. In the case of a coaxial waveguide whose center axis lies along the $\hat{z}$ axis, the natural solutions are

$$G(\phi) = C\cos(m\phi) + D\sin(m\phi) \tag{B.13}$$

$$H(z) = Ee^{-jk_zz} + Fe^{jk_zz} \tag{B.14}$$

where z dependent exponential terms describe propagation in the $\hat{z}$ direction and ϕ dependent terms describe the circumferential variation of the field around the $\hat{z}$ axis.

The solution to (B.1) is now given by a product of the individual solutions as in (B.3),

$$\Psi_{m,n}(\rho,\phi,z) = \left[A_{m,n}J_m(k_\rho\rho) + B_{m,n}Y_m(k_\rho\rho)\right]\left[C_{m,n}\cos(m\phi) + D_{m,n}\sin(m\phi)\right]\times \left[E_{m,n}e^{-\gamma z} + F_{m,n}e^{\gamma z}\right] \quad \text{(B.15)}$$

where $\gamma = jk_z$ and subscripts m and n are added for denoting unique solutions. Additionally the constraint equation

$$k_\rho^2 = k^2 + \gamma^2 \quad \text{(B.16)}$$

must hold for all solutions.

Appendix C. Cutoff Frequency of a TEM Field

The cutoff frequency of a TEM field is 0 Hz. This property allows low frequency measurements when a TEM field is excited (such as in a two conductor transmission line). Proving the cutoff frequency bound is done by examining the fields with respect to Maxwell's equations, and, by implication, the wave equation. By definition, the $\hat{z}$ directed field components of a TEM^z wave are equivalent to zero. The electric and magnetic fields in a TEM^z wave are therefore completely described by transverse field components

$$\mathbf{E} = \mathbf{E}_t(\rho, \phi, z) \tag{C.1}$$

$$\mathbf{H} = \mathbf{H}_t(\rho, \phi, z) \tag{C.2}$$

which must satisfy Maxwell's equations and, as a consequence, the wave equation (A.14).

Faraday's law is reduced to

$$\nabla \times \mathbf{E}_t = 0 \tag{C.3}$$

when only the transverse field components are present. Using the vector identitiy [3]:

$$\nabla \times (\nabla_t \psi) = 0 \tag{C.4}$$

the transverse electric field can be posed as the transverse gradient of the scalar $\psi(\rho, \phi, z)$. Substituting into Gauss' law and assuming a simple media

$$\begin{aligned} \nabla \cdot \mathbf{E}_t &= \nabla \cdot (\nabla_t \psi) \\ &= \nabla_t^2 \psi \\ &= 0 \end{aligned} \tag{C.5}$$

where ∇_t is the gradient of the transverse components only or

$$\nabla = \underbrace{\hat{\rho}\frac{\partial}{\partial\rho} + \hat{\phi}\frac{1}{\rho}\frac{\partial}{\partial\phi}}_{\nabla_t} + \frac{\partial}{\partial z} \tag{C.6}$$

The wave equation where only transverse fields are present is

$$\nabla^2\mathbf{E}_t + k^2\mathbf{E}_t = 0 \tag{C.7}$$

For a wave travelling in the $\hat{z}$ direction, the tangential electric field $\mathbf{E}_t(\rho,\phi,z)$ is equivalent to $\mathbf{E}_t(\rho,\phi)e^{-\gamma z}$. The vector Laplacian defined with respect to transverse and longitudinal components is

$$\nabla^2 = \nabla_t^2 + \frac{\partial^2}{\partial z^2} \tag{C.8}$$

and when applied to the electric field is

$$\begin{aligned}\nabla^2\mathbf{E}_t(\rho,\phi)e^{-\gamma z} &= \left(\nabla_t^2 + \frac{\partial^2}{\partial z^2}\right)\mathbf{E}_t(\rho,\phi)e^{-\gamma z} \\ &= \nabla_t^2\mathbf{E}_t(\rho,\phi)e^{-\gamma z} + \gamma\mathbf{E}_t(\rho,\phi)e^{-\gamma z} \\ &= \left(\nabla_t^2 + \gamma^2\right)\mathbf{E}_t(\rho,\phi,z)\end{aligned} \tag{C.9}$$

Substituting (C.9) into (C.7) results in

$$\nabla_t^2\mathbf{E}_t + (\gamma^2 + k^2)\mathbf{E}_t = 0 \tag{C.10}$$

Restating previous results from (C.5)

$$\begin{aligned}\mathbf{E}_t &= \nabla_t\psi \\ \nabla_t^2\psi &= 0\end{aligned}$$

and substituting into (C.10) produces

$$\begin{aligned}
\nabla_t^2 \left(\nabla_t \psi\right) + \left(\gamma^2 + k^2\right)\left(\nabla_t \psi\right) &= 0 \\
\nabla_t \left(\nabla_t^2 \psi + (\gamma^2 + k^2)\psi\right) &= 0 \\
(\gamma^2 + k^2)\nabla_t \psi &= 0 \\
(\gamma^2 + k^2)\mathbf{E}_t &= 0
\end{aligned}$$

The non-trivial result requires that $\gamma^2 = -k^2$. Recalling the constraint equation (B.16) and $k = \omega\sqrt{\epsilon\mu}$, it is evident $k_\rho = 0$ for a TEM wave. As such the propagation constant, γ, varies directly with frequency, ω, and there is no frequency at which the term describing propagation, $e^{-\gamma z}$, is purely real. A purely real result would produces an evanescent (decaying) wave. A TEM wave, when possible, will always propagate without respect to frequency.

Appendix D. TEM and TM Mode Orthogonality

Mode orthogonality is a critical component to understanding the power carrying mechanisms in waveguide. Each mode must independently carry power to which the total power is the summation of the individual mode powers [6]. Therefore, each mode function must be orthogonal. Mathematically, the solutions to the scalar wave equation must satisfy [1]

$$\int_S \Psi_g \Psi_h dS = 0 \qquad \ldots \quad g \neq h \tag{D.1}$$

or the equivalent for vectors

$$\int_S \nabla_t \Psi_g \cdot \nabla_t \Psi_h dS = 0 \qquad \ldots \quad g \neq h \tag{D.2}$$

The following analysis assumes a coaxial waveguide with no discontinuities and only TEM and TM modes present. Although a parallel analysis for TE modes is possible, it is unnecessary for this research.

D.1 General Field Solution in Cylindrical Coordinates

Constructing field equations from vector potentials is thoroughly covered in [3]. Generating TM^z fields requires only a $\hat{z}$ directed potential function that satisfies the scalar wave equation

$$\nabla^2 A_z + k^2 A_z = 0$$

This is equivalent to (B.1) and therefore (B.15) is a valid form of A_z or

$$A_z = \Psi_g(\rho, \phi, z) = \Psi_g(\rho, \phi)\, e^{-\gamma z} \tag{D.3}$$

where m, n pairs are replaced by a single mode identifier, g, and only the forward propagating wave is considered for simplicity. The electric field for a TM^z mode is

therefore defined as

$$\begin{aligned}
\mathbf{E} &= \frac{1}{j\omega\epsilon\mu}\left(k^2 + \nabla\nabla\cdot\right)\hat{z}\Psi_g\left(\rho,\phi\right)e^{-\gamma z} \\
&= \frac{1}{j\omega\epsilon\mu}\left[\hat{z}k^2\Psi_g\left(\rho,\phi\right)e^{-\gamma z} + \left(\nabla_t + \hat{z}\frac{\partial}{\partial z}\right)\left(-\gamma\Psi_g\left(\rho,\phi\right)e^{-\gamma z}\right)\right] \\
&= \frac{1}{j\omega\epsilon\mu}\left[\hat{z}\left(k^2+\gamma^2\right)\Psi_g\left(\rho,\phi\right)e^{-\gamma z} - \gamma e^{-\gamma z}\nabla_t\Psi_g\left(\rho,\phi\right)\right] \qquad \text{(D.4)}
\end{aligned}$$

where ∇ is replaced with the transverse and longitudinal operator (C.6). The result is the separation of the $\hat{z}$ directed field from the transverse fields. Both must satisfy the scalar wave equation.

D.2 Orthogonality of $\hat{z}$ directed fields

The $\hat{z}$ directed fields are a function of and proportional to the original solution, $\Psi_g\left(\rho,\phi\right)e^{-\gamma z}$. Considering two unique solutions, $\Psi_g\left(\rho,\phi,z\right)$ and $\Psi_h\left(\rho,\phi,z\right)$, they both must independently satisfy the scalar wave equation as

$$\begin{aligned}
\nabla_t^2\Psi_g + (k^2+\gamma_g^2)\Psi_g &= 0 \qquad \text{(D.5)} \\
\nabla_t^2\Psi_h + (k^2+\gamma_h^2)\Psi_h &= 0
\end{aligned}$$

Multiplying each scalar wave equation by the opposing solution and subtracting the two results produces

$$(\gamma_g^2-\gamma_h^2)\Psi_g\Psi_h = \Psi_g\nabla_t^2\Psi_h - \Psi_h\nabla_t^2\Psi_g \qquad \text{(D.6)}$$

Thought the LHS is well-suited to analysis via (D.1), the RHS can be further manipulated via the identities

$$\begin{aligned}
\nabla^2\psi &= \nabla\cdot\nabla\psi \qquad \text{(D.7)} \\
\psi\left(\nabla\cdot\mathbf{A}\right) &= \nabla\cdot\left(\psi\mathbf{A}\right) - \mathbf{A}\cdot\nabla\psi \qquad \text{(D.8)}
\end{aligned}$$

Figure D.1: In two dimensions, the surface and closed line integration for the orthogonality condition in an empty coaxial is the freespace region bounded by the inner and outer conductor. The closed line integration connects the inner and outer conductor via a twice followed path whose integration is equal and opposite thereby reducing the the connecting integration to zero.

to produce

$$\begin{aligned} \Psi_g \nabla_t^2 \Psi_h - \Psi_h \nabla_t^2 \Psi_g &= \nabla_t \cdot (\Psi_g \nabla_t \Psi_h) - \nabla_t \cdot (\Psi_h \nabla_t \Psi_g) \\ &= \nabla_t \cdot (\Psi_g \nabla_t \Psi_h - \Psi_h \nabla_t \Psi_g) \end{aligned}$$

Substituting this result into (D.6), integrating with respect to the paths in figure D.1, and applying the divergence theorem in two dimensions [9]

$$\begin{aligned} (\gamma_g^2 - \gamma_h^2) \iint_S \Psi_g \Psi_h dS &= \iint_S \left[\nabla_t \cdot (\Psi_g \nabla_t \Psi_h - \Psi_h \nabla_t \Psi_g)\right] dS \\ &= \oint_C (\Psi_g \nabla_t \Psi_h - \Psi_h \nabla_t \Psi_g) \cdot \hat{n} dl \end{aligned} \tag{D.9}$$

Recalling that Ψ_g and Ψ_h are proportional to the $\hat{z}$ directed electric field for mode g and h respectively, the enforcement of tangential boundary conditions on the PEC wall of the coaxial line requires $E_z = 0$ and therefore requiring the solutions Ψ_g and Ψ_h are equivalent to 0 along the integration contour. For this reason (D.9) reduces to (D.1) and the $\hat{z}$ directed fields are proven orthogonal.

It is important to note the following:

1. The development above applies to TM fields. By definition, $E_z = 0$ for a TEM field and (D.1) reduces to a trivial result ensuring orthogonality.

2. Evident in (D.9) is the potential for a trivial solution should two unique solutions have identical eigenvalues ($\gamma_g^2 = \gamma_h^2$). The solutions are then considered degenerate [6]. In assuming only axially symmetric modes, this research does not require consideration of degenerate modes.

3. The solutions Ψ_g and Ψ_h are only valid over the surface shown in figure D.1.

D.3 Orthogonality of transverse fields

The transverse fields are a function of and proportional to the transverse gradient of the original solution, $\Psi_g(\rho,\phi)\,e^{-\gamma z}$. Unique solutions are then $\nabla_t\Psi_g(\rho,\phi,z)$ and $\nabla_t\Psi_h(\rho,\phi,z)$. A simple derivation is produced by substituting the transverse solutions into (D.7) and (D.8) as

$$\begin{aligned}\nabla_t\Psi_g\cdot\nabla_t\Psi_h &= \nabla_t\cdot(\Psi_h\nabla_t\Psi_g)-\Psi_h(\nabla_t\cdot\nabla_t\Psi_g)\\ &= \nabla_t\cdot(\Psi_h\nabla_t\Psi_g)-\Psi_h\nabla_t^2\Psi_g \end{aligned}\tag{D.10}$$

The integral of (D.10) over the cross-sectional surface of the waveguide produces Green's identity in two dimensions [9]

$$\iint_S \nabla_t\Psi_g\cdot\nabla_t\Psi_h dS = \oint_C \Psi_h\nabla_t\Psi_g\cdot\hat{n}dl - \iint_S \Psi_h\nabla_t^2\Psi_g dS \tag{D.11}$$

Again, the RHS closed contour integration is equivalent to zero based on the enforcement of tangential boundary conditions and the proportionality of Ψ_h to E_z. By substituting (D.5) into (D.11)

$$\iint_S \nabla_t\Psi_g\cdot\nabla_t\Psi_h dS = -(k^2+\gamma_g^2)\iint_S \Psi_h\Psi_g dS \tag{D.12}$$

for which the already proven (D.1) reduces the RHS to 0, proving (D.2) and consequently the orthogonality of transverse fields of a TM^z wave. Recalling the use of $\mathbf{E}_{TEM} = \nabla_t \Psi$ in appendix C, it is apparent that the orthogonality proven for the transverse fields of a TM^z wave applies to a TEM^z wave.

Appendix E. Bessel Integration Identities

The following identities are used to produce reduced analytical expressions for the coupling integrals of the MAM. The identities are developed in similar forms in [8], [11], [14], and [16].

$$\begin{aligned}\int \left[\mathbf{Z_n}(\alpha\mathbf{x})\right]^{\mathbf{2}} \mathbf{x}\mathbf{dx} &= \frac{\mathbf{x^2}}{\mathbf{2}}\left\{\left[\mathbf{Z_n}(\alpha\mathbf{x})\right]^{\mathbf{2}} - \mathbf{Z_{n-1}}(\alpha\mathbf{x})\mathbf{Z_{n+1}}(\alpha\mathbf{x})\right\} \qquad \text{(E.1)}\\ &= \frac{\mathbf{x^2}}{\mathbf{2}}\left\{\left[\mathbf{Z_n}(\alpha\mathbf{x})\right]^{\mathbf{2}} + \left[\mathbf{Z_{n-1}}(\alpha\mathbf{x})\right]^{\mathbf{2}} - \frac{\mathbf{2n}}{\alpha\mathbf{x}}\mathbf{Z_{n-1}}(\alpha\mathbf{x})\mathbf{Z_n}(\alpha\mathbf{x})\right\}\end{aligned}$$

where Z_n is a Bessel function or linear summation of Bessel functions of the first and second kind.

Proof

Starting with Bessel's differential equation

$$\begin{aligned} x^2u'' + xu' + \left[(\alpha x)^2 - n^2\right]u &= 0 \\ 2x^2u'u'' + 2xu'u' + 2uu'(\alpha x)^2 - 2uu'n^2 &= 0 \quad \ldots(\text{mult. by } 2u') \\ 2x^2u'u'' + 2xu'u' + 2uu'(\alpha x)^2 - 2uu'n^2 + (2\alpha^2xu^2 - 2\alpha^2xu^2) &= 0 \quad \ldots(\text{adding zero}) \\ \frac{d}{dx}\left\{x^2(u')^2 + \left[(\alpha x)^2 - n^2\right]u^2\right\} - 2\alpha^2xu^2 &= 0 \\ \left\{x^2(u')^2 + \left[(\alpha x)^2 - n^2\right]u^2\right\} &= 2\alpha^2\int xu^2dx \end{aligned}$$

The solution to Bessel's equation, u, must take the form of a Bessel function or linear summation of Bessel functions. This research uses linear summation's of Bessel functions of the first and second kind (J_n and Y_n , respectively) such that

$$u = Z_n(\alpha x)$$

where Z_n can take the form $J_n(\lambda x)$, $Y_n(\lambda x)$, or $AJ_n(\lambda x) + BY_n(\lambda x)$ It is important to note that derivatives in the Bessel differential equation are taken with respect to

x such as $u' = \frac{du}{dx}$. Applying this to the substitution $u = Z_n(\alpha x)$ produces

$$\begin{aligned} \frac{du}{dx} &= \frac{d}{dx} Z_n(\alpha x) \\ &= \alpha \frac{d}{dx} Z_n(\alpha x) \\ &= \alpha Z_n'(\alpha x) \end{aligned}$$

Continuing the proof by substituting for u

$$\int [Z_n(\alpha x)]^2 x dx = \frac{x^2}{2} \left\{ [Z_n'(\alpha x)]^2 + [Z_n(\alpha x)]^2 - \left(\frac{n}{\alpha x}\right)^2 [Z_n(\alpha x)]^2 \right\}$$

the recursion relations [1]

$$\begin{aligned} Z_{n-1}(\alpha x) &= \frac{n}{\alpha x} Z_n(\alpha x) + \frac{d}{d(\alpha x)} Z_n(\alpha x) \\ Z_{n+1}(\alpha x) &= \frac{n}{\alpha x} Z_n(\alpha x) - \frac{d}{d(\alpha x)} Z_n(\alpha x) \end{aligned}$$

are readily used to complete the proof as

$$\int [Z_n(\alpha x)]^2 x dx = \frac{x^2}{2} \left\{ [Z_n(\alpha x)]^2 - Z_{n-1}(\alpha x) Z_{n+1}(\alpha x) \right\}$$

$$\int \mathbf{Z_n}(\alpha\mathbf{x})\mathbf{W_n}(\beta\mathbf{x})\mathbf{x}\mathbf{dx} = \frac{\mathbf{x}\beta\mathbf{Z_n}(\alpha\mathbf{x})\mathbf{W_{n-1}}(\beta\mathbf{x}) - \mathbf{x}\alpha\mathbf{Z_{n-1}}(\alpha\mathbf{x})\mathbf{W_n}(\beta\mathbf{x})}{\alpha^{\mathbf{2}} - \beta^{\mathbf{2}}} \qquad \text{(E.2)}$$

where Z_n and W_n are Bessel functions or linear summation of Bessel functions of the first and second kind.

Proof

Starting with Bessel's differential equation

$$\begin{aligned} x^2u'' + xu' + \left[(\alpha x)^2 - n^2\right] u &= 0 \\ x^2v'' + xv' + \left[(\beta x)^2 - n^2\right] v &= 0 \end{aligned}$$

where u and v are unique solutions. Multiplying by $\frac{v}{x}$ and $\frac{u}{x}$ respectively and subtracting the result gives

$$\begin{aligned} xu''v + u'v + (\alpha^2x^2 - n^2)\frac{uv}{x} - xv''u - v'u - (\beta^2x^2 - n^2)\frac{uv}{x} &= 0 \\ xu''v - xv''u + u'v - uv' + (\alpha^2 - \beta^2)uvx &= 0 \\ \frac{d}{dx}\left\{x(u'v - uv')\right\} + uvx(\alpha^2 - \beta^2) &= 0 \end{aligned}$$

Integrating with respect to x produces

$$\int uvxdx = \frac{x(uv' - u'v)}{\alpha^2 - \beta^2}$$

The solutions to Bessel's equation, u and v, must take the form of a Bessel function or linear summation of Bessel functions. This research uses linear summation's of Bessel functions of the first and second kind (J_n and Y_n , respectively) such that

$$\begin{aligned} u &= Z_n(\alpha x) \\ v &= W_n(\beta x) \end{aligned}$$

where both Z_n and W_n can take the form $J_n(\lambda x)$, $Y_n(\lambda x)$, or $AJ_n(\lambda x) + BY_n(\lambda x)$. Using the recursion relation [1]

$$\frac{d}{dx}Z_n(\alpha x) = \alpha Z_n'(\alpha x) = \alpha\left[Z_{n-1}(\alpha x) - \frac{n}{\alpha x}Z_n(\alpha x)\right]$$

and substituting $u = Z_n(\alpha x)$ and $v = W_n(\beta x)$ produces

$$\begin{aligned}\int Z_n(\alpha x)W_n(\beta x)x dx &= \frac{x\left\{Z_n(\alpha x)\frac{d}{dx}W_n(\beta x) - \frac{d}{dx}Z_n(\alpha x)W_n(\beta x)\right\}}{\alpha^2 - \beta^2} \\ &= \frac{x\beta Z_n(\alpha x)W_{n-1}(\beta x) - x\alpha Z_{n-1}(\alpha x)W_n(\beta x)}{\alpha^2 - \beta^2}\end{aligned}$$

completing the proof.

Appendix F. Fields Within a Coaxial Transmission Line

The fields within a coaxial transmission line are well-documented, [10]. There specific forms are developed here as a reference.

F.1 TM Fields in a Coaxial Line

TM^z fields in region I and III of figure 3.1 are generated from a $\hat{z}$ directed potential function that is a solution to the wave equation [3]. The potential function is (B.15) and the generation functions are

$$E_\rho = -j\frac{1}{\omega\mu\varepsilon}\frac{\partial^2\Psi}{\partial\rho\partial z} \qquad H_\rho = \frac{1}{\mu}\frac{1}{\rho}\frac{\partial\Psi}{\partial\phi}$$

$$E_\phi = -j\frac{1}{\omega\mu\varepsilon}\frac{1}{\rho}\frac{\partial^2\Psi}{\partial\phi\partial z} \qquad H_\phi = -\frac{1}{\mu}\frac{\partial\Psi}{\partial\rho}$$

$$E_z = -j\frac{1}{\omega\mu\varepsilon}\left(\frac{\partial^2}{\partial z^2} + k^2\right)\Psi \qquad H_z = 0$$

which, considering only a forward propagating wave, produce

$$\begin{aligned}
E_\rho &= j\frac{\gamma k_\rho}{\omega\mu\epsilon}\underline{\mathrm{V}}'_m\left(k_{\rho_n}\rho\right)\left[C_{m,n}\cos\left(m\phi\right) + D_{m,n}\sin\left(m\phi\right)\right]e^{-\gamma_z} \\
E_\phi &= j\frac{m\gamma}{\omega\mu\epsilon}\left(\frac{1}{\rho}\right)\underline{\mathrm{V}}_m\left(k_{\rho_n}\rho\right)\left[C_{m,n}\sin\left(m\phi\right) - D_{m,n}\cos\left(m\phi\right)\right]e^{-\gamma_z} \\
E_z &= -j\frac{k_{\rho_n}^2}{\omega\mu\epsilon}\underline{\mathrm{V}}_m\left(k_{\rho_n}\rho\right)\left[C_{m,n}\cos\left(m\phi\right) + D_{m,n}\sin\left(m\phi\right)\right]e^{-\gamma_z} \\
H_\rho &= \frac{m}{\mu}\left(\frac{1}{\rho}\right)\underline{\mathrm{V}}_m\left(k_{\rho_n}\rho\right)\left[C_{m,n}\sin\left(m\phi\right) - D_{m,n}\cos\left(m\phi\right)\right]e^{-\gamma_z} \\
H_\phi &= -\frac{k_{\rho_n}}{\mu}\underline{\mathrm{V}}'_m\left(k_{\rho_n}\rho\right)\left[C_{m,n}\cos\left(m\phi\right) + D_{m,n}\sin\left(m\phi\right)\right]e^{-\gamma_z} \\
H_z &= 0
\end{aligned}$$

where

$$\begin{aligned}\underline{\mathrm{V}}_m\left(k_{\rho_n}\rho\right) &= \left[A_{m,n}J_m\left(k_{\rho_n}\rho\right)+B_{m,n}Y_m\left(k_{\rho_n}\rho\right)\right]\\ \underline{\mathrm{V}}'_m\left(k_{\rho_n}\rho\right) &= \left[A_{m,n}J'_m\left(k_{\rho_n}\rho\right)+B_{m,n}Y'_m\left(k_{\rho_n}\rho\right)\right]\end{aligned}$$

and m, n identify the TM_{mn} mode. Boundary conditions require the tangential electric fields to be zero at the inner and outer conductor of a coaxial line. Assuming the conductor is a PEC, knowing that the condition must be met independently of ϕ, and that the surface normal reference for the tangential fields is $\hat{\rho}$, the appropriate boundary conditions are

$$E_\phi(\rho=a,\phi,z)=E_\phi(\rho=b,\phi,z)=E_z(\rho=a,\phi,z)=E_z(\rho=b,\phi,z)=0$$

where a and b are the radius of the outer surface of the inner conductor and the inner surface of the outer conductor respectively. Applying the boundary condtion at $\rho=a$, solving for the constant

$$A_{m,n}=-B_{m,n}\frac{Y_m\left(k_{\rho_n}a\right)}{J_m\left(k_{\rho_n}a\right)}$$

and substituting modifies the field equations to

$$\begin{aligned}E_\rho &= j\frac{\gamma k_\rho B_{m,n}}{\omega\mu\epsilon J_m\left(k_{\rho_n}a\right)}V'_m\left(k_{\rho_n}\rho\right)\left[C_{m,n}\cos\left(m\phi\right)+D_{m,n}\sin\left(m\phi\right)\right]e^{-\gamma_z}\\ E_\phi &= j\frac{m\gamma B_{m,n}}{\omega\mu\epsilon J_m\left(k_{\rho_n}a\right)}\left(\frac{1}{\rho}\right)V_m\left(k_{\rho_n}\rho\right)\left[C_{m,n}\sin\left(m\phi\right)-D_{m,n}\cos\left(m\phi\right)\right]e^{-\gamma_z}\\ E_z &= -j\frac{k_{\rho_n}^2 B_{m,n}}{\omega\mu\epsilon J_m\left(k_{\rho_n}a\right)}V_m\left(k_{\rho_n}\rho\right)\left[C_{m,n}\cos\left(m\phi\right)+D_{m,n}\sin\left(m\phi\right)\right]e^{-\gamma_z}\\ H_\rho &= \frac{mB_{m,n}}{\mu J_m\left(k_{\rho_n}a\right)}\left(\frac{1}{\rho}\right)V_m\left(k_{\rho_n}\rho\right)\left[C_{m,n}\sin\left(m\phi\right)-D_{m,n}\cos\left(m\phi\right)\right]e^{-\gamma_z}\\ H_\phi &= -\frac{k_{\rho_n}B_{m,n}}{\mu J_m\left(k_{\rho_n}a\right)}V'_m\left(k_{\rho_n}\rho\right)\left[C_{m,n}\cos\left(m\phi\right)+D_{m,n}\sin\left(m\phi\right)\right]e^{-\gamma_z}\\ H_z &= 0\end{aligned}$$

where

$$\begin{aligned} V_m\left(k_{\rho_n}\rho\right) &= \left[J_m\left(k_{\rho_n}\rho\right)Y_m\left(k_{\rho_n}a\right) - J_m\left(k_{\rho_n}a\right)Y_m\left(k_{\rho_n}\rho\right)\right] \\ V'_m\left(k_{\rho_n}\rho\right) &= \left[J'_m\left(k_{\rho_n}\rho\right)Y_m\left(k_{\rho_n}a\right) - J_m\left(k_{\rho_n}a\right)Y'_m\left(k_{\rho_n}\rho\right)\right] \end{aligned}$$

Applying boundary conditions at $\rho = b$ produces the characteristic equation necessary to solve for k_{ρ_n} as

$$\left[J_m\left(k_{\rho_n}b\right)Y_m\left(k_{\rho_n}a\right) - J_m\left(k_{\rho_n}a\right)Y_m\left(k_{\rho_n}b\right)\right] = 0 \tag{F.1}$$

where the subscript n denotes the nth zero of (F.1).

F.2 TEM Fields in a Coaxial Line

TEM^z fields are the dominant mode in a coaxial line and have a cutoff frequency equal to 0 Hz. The development of appendix C can be continued to define the electric and magnetic field equations, but a more interesting method is to apply the result $\mathbf{E} = \nabla_t\psi$ and $k_\rho = 0$ to the TM^z fields derived in the previous section. Physically, a potential gradient will not exist in the $\hat{\phi}$ direction for a TEM field because the conductors are coaxial and therefore $\mathbf{E} = \nabla_t\psi$ implies a $\hat{\rho}$ directed electric field potential gradient. Additionally, the electric potential gradient, $\nabla_t\psi$, must be independent of ϕ making the resulting field axially symmetric. The TM^z fields are axially symmetric when $m = 0$.

Taking the limit as $k_{\rho_n} \to 0$ for axially symmetric ($m = 0$) TM^z fields, using the small argument approximations shown in table F.1, and considering only forward propagating waves

$$\begin{aligned} E_\phi &= 0 \quad \ldots \quad m = 0 \text{ for axially symmetric fields} \\ H_\rho &= 0 \quad \ldots \quad m = 0 \text{ for axially symmetric fields} \\ H_z &= 0 \quad \ldots \quad \text{TM}^z \end{aligned}$$

$$\lim_{k_{\rho_n}\to 0} E_\rho = \frac{k_{\rho_n}\gamma_n B^+_{0,n}}{j\omega\mu\epsilon}\left[\left(\frac{k_{\rho_n}\rho}{2}\right)\left(\frac{2}{\pi}\ln\left(\frac{\gamma k_{\rho_n}a}{2}\right)\right)-(1)\left(\frac{-2}{\pi k_{\rho_n}\rho}\right)\right]e^{-\gamma_n z}$$

$$= \frac{\gamma_n B^+_{0,n}}{j\omega\mu\epsilon}\left[\left(\frac{2k_{\rho_n}\rho}{\pi a\gamma}\right)\left(\frac{\gamma k_{\rho_n}a}{2}\ln\left(\frac{\gamma k_{\rho_n}a}{2}\right)\right)+\left(\frac{2}{\pi\rho}\right)\right]e^{-\gamma_n z}$$

$$= \frac{2kB^+_{0,n}}{\pi\omega\mu\epsilon}\left[\frac{1}{\rho}\right]e^{-jkz} \quad \ldots \quad \lim_{k_{\rho_n}\to 0} k^2 = k_{\rho_n}^2 + k_z^2 = \omega^2\mu\epsilon$$

$$\lim_{k_{\rho_n}\to 0} E_z = \frac{k^2_{\rho_n}B^+_{0,n}}{j\omega\mu\epsilon}\left[(1)\left(\frac{2}{\pi}\ln\left(\frac{\gamma k_{\rho_n}a}{2}\right)\right)-(1)\left(\frac{2}{\pi}\ln\left(\frac{\gamma k_{\rho_n}\rho}{2}\right)\right)\right]e^{-\gamma_n z}$$

$$= \frac{k_{\rho_n}B^+_{0,n}}{j\omega\mu\epsilon}\left[\frac{4\gamma k_{\rho_n}a}{2\pi a\gamma}\ln\left(\frac{\gamma k_{\rho_n}a}{2}\right)-\frac{4\gamma k_{\rho_n}\rho}{2\pi\rho\gamma}\ln\left(\frac{\gamma k_{\rho_n}\rho}{2}\right)\right]e^{-\gamma_n z}$$

$$= 0$$

$$\lim_{k_{\rho_n}\to 0} H_\phi = \frac{k_{\rho_n}B^+_{0,n}}{\mu}\left[\left(\frac{k_{\rho_n}\rho}{2}\right)\left(\frac{2}{\pi}\ln\left(\frac{\gamma k_{\rho_n}a}{2}\right)\right)-(1)\left(\frac{-2}{\pi k_{\rho_n}\rho}\right)\right]e^{-\gamma_n z}$$

$$= \frac{B^+_{0,n}}{\mu}\left[\left(\frac{2k_{\rho_n}\rho}{\pi a\gamma}\right)\left(\frac{\gamma k_{\rho_n}a}{2}\ln\left(\frac{\gamma k_{\rho_n}a}{2}\right)\right)+\left(\frac{2}{\pi\rho}\right)\right]e^{-\gamma_n z}$$

$$= \frac{2B^+_{0,n}}{\pi\mu}\left[\frac{1}{\rho}\right]e^{-\gamma_n z}$$

$$= \left(\frac{k_z\omega\epsilon\mu}{k_z\omega\epsilon\mu}\right)\frac{2B^+_{0,n}}{\pi\mu}\left[\frac{1}{\rho}\right]e^{-\gamma_n z}$$

$$= \left(\frac{2kB^+_{0,n}}{\pi\omega\epsilon\mu}\right)\frac{\omega\epsilon\mu}{\mu\omega\sqrt{\epsilon\mu}}\left[\frac{1}{\rho}\right]e^{-jkz} \quad \ldots \quad \lim_{k_{\rho_n}\to 0} k^2 = k_{\rho_n}^2 + k_z^2 = \omega^2\mu\epsilon$$

$$= \left(\frac{2kB^+_{0,n}}{\pi\omega\epsilon\mu}\right)\frac{1}{Z_{TEM}}\left[\frac{1}{\rho}\right]e^{-jkz}$$

where $Z_{TEM} = \sqrt{\frac{\mu}{\epsilon}}$.

Table F.1: Bessel and logarithmic function small argument limits

$\lim_{x\to 0} J_0(x)$	$\simeq$	1	$\lim_{x\to 0} Y_0(x)$	$\simeq$	$\frac{2}{\pi}\ln\left(\frac{\gamma x}{2}\right)$
$\lim_{x\to 0} J_1(x)$	$\simeq$	$\frac{x}{2}$	$\lim_{x\to 0} Y_1(x)$	$\simeq$	$\frac{-2}{\pi x}$
$\lim_{x\to 0} x^{\alpha}\ln x$	$=$	0	(α constant, $\Re(\alpha) > 0$)		

In summary, axially symmetric TM^z fields reduce to a TEM field defined by

$$E_\rho = \Upsilon\left[\frac{1}{\rho}\right]e^{-jkz} \tag{F.2}$$

$$H_\phi = \frac{\Upsilon}{Z_{TEM}}\left[\frac{1}{\rho}\right]e^{-jkz} \tag{F.3}$$

where

$$\Upsilon = \frac{2kB_{0,n}^{+}}{\pi\omega\mu\epsilon} \tag{F.4}$$

Appendix G. Transverse Mode dependent Vector Coupling Integrals

This appendix documents the development of coupling integral solutions. It does not provide the greatest simplification, but does give a general solution and a simplified solution for both inner and outer air gaps. Coaxial line regions I, II, and III are as indicated in figure G.1.

G.1 Symbols Defined

G.1.1 General.

$$\begin{aligned} V_m(\alpha\rho) &= J_m(\alpha\rho)\,Y_0(\alpha a) - J_0(\alpha a)\,Y_m(\alpha\rho) \\ W_m(\alpha\rho) &= J_m(\alpha\rho)\,Y_0(\alpha b) - J_0(\alpha b)\,Y_m(\alpha\rho) \end{aligned}$$

where J_m is a Bessel function of the first kind of order m and Y_m is a Bessel function of the second kind of order m (sometimes referred to as a Neumann function).

G.1.2 Regions I and III (Freespace).

$$\gamma_n^2 = k_{\rho n}^2 - k_0^2 \qquad k_0 = \omega\sqrt{\mu_0\epsilon_0}$$

$$Z_n = \frac{\gamma_n}{j\omega\epsilon_0} \qquad H = \frac{\pi\gamma_n k_{\rho n}}{j2k_0}$$

where k_{ρ_n} is the nth solution of

$$V_0 = J_0(k_{\rho_n} b)\,Y_0(k_{\rho_n} a) - J_0(k_{\rho_n} a)\,Y_0(k_{\rho_n} b) = 0$$

G.1.3 Region II (Material with Air Gap).

$$\begin{aligned} k_{\rho 1n}^2 &= \tilde{\gamma}_n^2 + k_1^2 & k_{\rho 2n}^2 &= \tilde{\gamma_n}^2 + k_2^2 \\ k_1 &= \omega\sqrt{\mu_1\epsilon_1} & k_1 &= \omega\sqrt{\mu_2\epsilon_2} \\ Z_{1n} &= \frac{\tilde{\gamma_n}}{j\omega\epsilon_1} & Z_{2n} &= \frac{\tilde{\gamma_n}}{j\omega\epsilon_2} \end{aligned}$$

where $k_{\rho 1n}$ and $k_{\rho 2n}$ are solutions to

$$k_{\rho 1n} Z_{1n}\ V_0\left(k_{\rho 1n} R\right)\ W_1\left(k_{\rho 2n} R\right) - k_{\rho 2n} Z_{2n}\ V_1\left(k_{\rho 1n} R\right)\ W_0\left(k_{\rho 2n} R\right) = 0 \qquad \text{(G.1)}$$

and

Outer Air Gap	Inner Air Gap
$R = r_2$	$R = r_1$
ϵ_1, μ_1 are sample properties	ϵ_1, μ_1 are ϵ_0, μ_0
ϵ_2, μ_2 are ϵ_0, μ_0	ϵ_2, μ_2 are sample properties
$C = \dfrac{\pi k_{\rho 1n} \tilde{\gamma_n}}{j2k_1}$	$C = \dfrac{\pi k_{\rho 2n} \tilde{\gamma_n}}{j2k_2}\ \dfrac{\epsilon_2}{\epsilon_1} \dfrac{W_1\left(k_{\rho 2n} R\right)}{V_1\left(k_{\rho 1n} R\right)}$
$D = \dfrac{\pi k_{\rho 1n} \tilde{\gamma_n}}{j2k_1}\ \dfrac{\epsilon_1}{\epsilon_2} \dfrac{V_1\left(k_{\rho 1n} R\right)}{W_1\left(k_{\rho 2n} R\right)}$	$D = \dfrac{\pi k_{\rho 2n} \tilde{\gamma_n}}{j2k_2}$

G.2 TEM testing operator coupling to Region II TM fields

$$\begin{aligned}
B_{1n} &= \int_a^R \mathbf{e}_1 \cdot \tilde{\mathbf{e}}_n\ \rho d\rho + \int_R^b \mathbf{e}_1 \cdot \tilde{\mathbf{e}}_n \rho d\rho \\
C_{1n} &= \int_a^R \mathbf{h}_1 \cdot \tilde{\mathbf{h}}_n\ \rho d\rho + \int_R^b \mathbf{h}_1 \cdot \tilde{\mathbf{h}}_n \rho d\rho \\
&= \frac{1}{Z_n Z_{1n}} \int_a^R \mathbf{e}_1 \cdot \tilde{\mathbf{e}}_n\ \rho d\rho + \frac{1}{Z_n Z_{2n}} \int_R^b \mathbf{e}_1 \cdot \tilde{\mathbf{e}}_n \rho d\rho
\end{aligned}$$

First Integral:

$$\begin{aligned}
\int_a^R \mathbf{e}_1 \cdot \tilde{\mathbf{e}}_n \ \rho d\rho &= C \int_a^R \left\{\frac{1}{\rho}\right\} \{V_1(k_{\rho 1n}\rho)\} \ \rho d\rho \\
&= C \int_a^R V_1(k_{\rho 1n}\rho) \ d\rho \\
&= C \left\{\frac{-1}{k_{\rho 1n}} V_0(k_{\rho 1n}\rho)\right\}\Big|_a^R \\
&= \frac{-C}{k_{\rho 1n}} V_0(k_{\rho 1n}R)
\end{aligned}$$

Second Integral:

$$\begin{aligned}
\int_R^b \mathbf{e}_1 \cdot \tilde{\mathbf{e}}_n \ \rho d\rho &= D \int_R^b \left\{\frac{1}{\rho}\right\} \{W_1(k_{\rho 2n}\rho)\} \ \rho d\rho \\
&= D \int_R^b W_1(k_{\rho 2n}\rho) \ d\rho \\
&= D \left\{\frac{-1}{k_{\rho 2n}} W_0(k_{\rho 2n}\rho)\right\}\Big|_R^b \\
&= \frac{D}{k_{\rho 2n}} W_0(k_{\rho 2n}R)
\end{aligned}$$

Therefore

$$\begin{aligned}
B_{1n} &= \frac{D}{k_{\rho 2n}} W_0(k_{\rho 2n}R) - \frac{C}{k_{\rho 1n}} V_0(k_{\rho 1n}R) \\
C_{1n} &= \frac{D}{Z_n Z_{2n} k_{\rho 2n}} W_0(k_{\rho 2n}R) - \frac{C}{Z_n Z_{1n} k_{\rho 1n}} V_0(k_{\rho 1n}R)
\end{aligned}$$

in general form. Using the characteristic equation (G.1), the general forms are simplified to for each gap scenario to:

Outer Gap

$$
\begin{aligned}
B_{1n} &= \frac{\pi\tilde{\gamma}_n}{j2k_1}\left[\left(\frac{k_{\rho 1n}}{k_{\rho 2n}}\right)^2 - 1\right] V_0(k_{\rho 1n}R) \\
C_{1n} &= \frac{\pi\tilde{\gamma}_n}{j2k_1 Z_n}\left[\frac{1}{Z_{2n}}\left(\frac{k_{\rho 1n}}{k_{\rho 2n}}\right)^2 - \frac{1}{Z_{1n}}\right] V_0(k_{\rho 1n}R)
\end{aligned}
$$

Inner Gap

$$
\begin{aligned}
B_{1n} &= \frac{\pi\tilde{\gamma}_n}{j2k_2}\left[1 - \left(\frac{k_{\rho 1n}}{k_{\rho 1n}}\right)^2\right] W_0(k_{\rho 2n}R) \\
C_{1n} &= \frac{\pi\tilde{\gamma}_n}{j2k_2 Z_n}\left[\frac{1}{Z_{2n}} - \frac{1}{Z_{1n}}\left(\frac{k_{\rho 1n}}{k_{\rho 1n}}\right)^2\right] W_0(k_{\rho 2n}R)
\end{aligned}
$$

G.3 TM testing operator coupling to Region II TM fields

$$
\begin{aligned}
B_{mn} &= \int_a^R \mathbf{e}_m \cdot \tilde{\mathbf{e}}_n \ \rho d\rho + \int_R^b \mathbf{e}_m \cdot \tilde{\mathbf{e}}_n \rho \ d\rho \qquad \ldots m > 1 \\
C_{mn} &= \frac{1}{Z_n Z_{1n}} \int_a^R \mathbf{e}_1 \cdot \tilde{\mathbf{e}}_n \ \rho d\rho + \frac{1}{Z_n Z_{2n}} \int_R^b \mathbf{e}_1 \cdot \tilde{\mathbf{e}}_n \rho \ d\rho \qquad \ldots m > 1
\end{aligned}
$$

First Integral:

$$
\begin{aligned}
\int_a^R \mathbf{e}_1 \cdot \tilde{\mathbf{e}}_n \ \rho d\rho &= H\ C \int_a^R V_1(k_{\rho n}\rho) V_1(k_{\rho 1n}\rho) \ \rho d\rho \\
&= H\ C \left.\frac{\rho k_{\rho 1n} V_1(k_{\rho n}\rho) V_0(k_{\rho 1n}\rho) - \rho k_{\rho n} V_0(k_{\rho n}\rho) V_1(k_{\rho 1n}\rho)}{k_{\rho n}^2 - k_{\rho 1n}^2}\right|_a^R \\
&= H\ C \frac{R k_{\rho 1n} V_1(k_{\rho n}R) V_0(k_{\rho 1n}R) - R k_{\rho n} V_0(k_{\rho n}R) V_1(k_{\rho 1n}R)}{k_{\rho n}^2 - k_{\rho 1n}^2}
\end{aligned}
$$

Second Integral:

$$\begin{aligned}
\int_a^R \mathbf{e}_1 \cdot \tilde{\mathbf{e}}_n \ \rho d\rho &= H\ D \int_a^R V_1(k_{\rho n}\rho) W_1(k_{\rho 2n}\rho)\ \rho d\rho \\
&= H\ D\ \frac{\rho k_{\rho 2n} V_1(k_{\rho n}\rho) W_0(k_{\rho 2n}\rho) - \rho k_{\rho n} V_0(k_{\rho n}\rho) W_1(k_{\rho 2n}\rho)}{k_{\rho n}^2 - k_{\rho 2n}^2}\Bigg|_R^b \\
&= -H\ D \frac{R k_{\rho 2n} V_1(k_{\rho n}R) W_0(k_{\rho 2n}R) - R k_{\rho n} V_0(k_{\rho n}R) W_1(k_{\rho 2n}R)}{k_{\rho n}^2 - k_{\rho 2n}^2}
\end{aligned}$$

Therefore

$$\begin{aligned}
B_{mn} = H\ R \Bigg\{ & C \frac{k_{\rho 1n} V_1(k_{\rho n}R) V_0(k_{\rho 1n}R) - k_{\rho n} V_0(k_{\rho n}R) V_1(k_{\rho 1n}R)}{k_{\rho n}^2 - k_{\rho 1n}^2} - \\
& D \frac{k_{\rho 2n} V_1(k_{\rho n}R) W_0(k_{\rho 2n}R) - k_{\rho n} V_0(k_{\rho n}R) W_1(k_{\rho 2n}R)}{k_{\rho n}^2 - k_{\rho 2n}^2} \Bigg\} \qquad \ldots m > 1
\end{aligned}$$

$$\begin{aligned}
C_{mn} = H\ R \Bigg\{ & C \frac{k_{\rho 1n} V_1(k_{\rho n}R) V_0(k_{\rho 1n}R) - k_{\rho n} V_0(k_{\rho n}R) V_1(k_{\rho 1n}R)}{Z_n Z_{1n} \left(k_{\rho n}^2 - k_{\rho 1n}^2\right)} - \\
& D \frac{k_{\rho 2n} V_1(k_{\rho n}R) W_0(k_{\rho 2n}R) - k_{\rho n} V_0(k_{\rho n}R) W_1(k_{\rho 2n}R)}{Z_n Z_{2n} \left(k_{\rho n}^2 - k_{\rho 2n}^2\right)} \Bigg\} \qquad \ldots m > 1
\end{aligned}$$

in general form, which simplifies for each gap scenario to

Outer Gap ($m > 1$)

$$B_{mn} = \frac{\pi\gamma_n k_{\rho n}}{j2k_0}\frac{\pi\tilde{\gamma}_n k_{\rho 1n}}{j2k_1}R \times \left[\left(\frac{1}{k_{\rho n}^2 - k_{\rho 1n}^2} - \frac{1}{k_{\rho n}^2 - k_{\rho 2n}^2}\right) k_{\rho 1n} V_1(k_{\rho n}R)V_0(k_{\rho 1n}R) + \left(\frac{\epsilon_1}{\epsilon_2(k_{\rho n}^2 - k_{\rho 2n}^2)} - \frac{1}{k_{\rho n}^2 - k_{\rho 2n}^2}\right) k_{\rho n} V_0(k_{\rho n}R)V_1(k_{\rho 1n}R)\right]$$

$$C_{mn} = \frac{\pi\gamma_n k_{\rho n}}{j2k_0 Z_n}\frac{\pi\tilde{\gamma}_n k_{\rho 2n}}{j2k_2 Z_{1n}}R \times \left[\left(\frac{1}{k_{\rho n}^2 - k_{\rho 1n}^2} - \frac{\epsilon_2}{\epsilon_1(k_{\rho n}^2 - k_{\rho 2n}^2)}\right) k_{\rho 2n} V_1(k_{\rho n}R)V_0(k_{\rho 2n}R) + \left(\frac{1}{k_{\rho n}^2 - k_{\rho 2n}^2} - \frac{1}{k_{\rho n}^2 - k_{\rho 2n}^2}\right) k_{\rho n} V_0(k_{\rho n}R)V_1(k_{\rho 1n}R)\right]$$

Inner Gap ($m > 1$)

$$B_{mn} = \frac{\pi\gamma_n k_{\rho n}}{j2k_0}\frac{\pi\tilde{\gamma}_n k_{\rho 2n}}{j2k_2}R \times \left[\left(\frac{1}{k_{\rho n}^2 - k_{\rho 1n}^2} - \frac{1}{k_{\rho n}^2 - k_{\rho 2n}^2}\right) k_{\rho 2n} V_1(k_{\rho n}R)W_0(k_{\rho 2n}R) + \left(\frac{1}{k_{\rho n}^2 - k_{\rho 2n}^2} - \frac{\epsilon_2}{\epsilon_1(k_{\rho n}^2 - k_{\rho 1n}^2)}\right) k_{\rho n} V_0(k_{\rho n}R)W_1(k_{\rho 2n}R)\right]$$

$$C_{mn} = \frac{\pi\gamma_n k_{\rho n}}{j2k_0 Z_n}\frac{\pi\tilde{\gamma}_n k_{\rho 2n}}{j2k_2 Z_{2n}}R \times \left[\left(\frac{\epsilon_1}{\epsilon_2(k_{\rho n}^2 - k_{\rho 1n}^2)} - \frac{1}{k_{\rho n}^2 - k_{\rho 2n}^2}\right) k_{\rho 2n} V_1(k_{\rho n}R)W_0(k_{\rho 2n}R) + \left(\frac{1}{k_{\rho n}^2 - k_{\rho 2n}^2} - \frac{1}{k_{\rho n}^2 - k_{\rho 1n}^2}\right) k_{\rho n} V_0(k_{\rho n}R)W_1(k_{\rho 2n}R)\right]$$

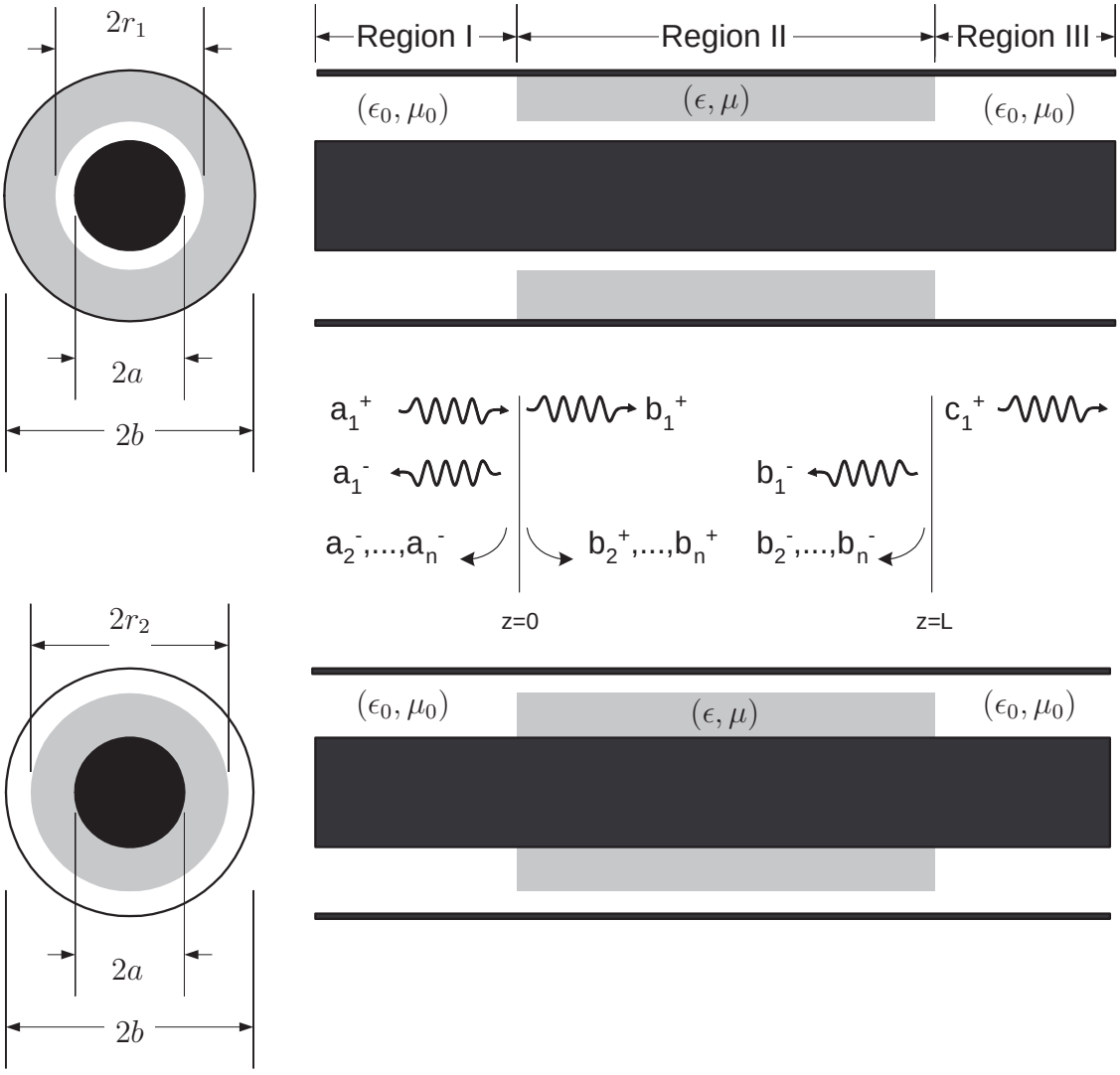

Figure G.1: The coupling of transverse electric and magnetic mode vectors is evaluate at $z = 0$ and $z = L$.

Appendix H. Higher Order Mode Excitation By Waveguide Discontinuity

Not all discontinuities excite higher order modes. Considering a simple media, higher order mode excitation is determined by examining the coupling of one mode, that of the excitation, to the infinite number of possible field modes within the system. The general modal method developed in the text (section 3.1) will be applied to the scenarios shown in figures H.1(a) and (b) to prove the excitation of higher order modes. It is important to recall that applying a testing operator in modal analysis is equivalent to determining the power coupling between two modes provided the testing operators are the fields in one section of the coaxial line.

The transverse interface in the guided structure of figure H.1(a) will not excite higher order modes. For this scenario, the mode dependent transverse vectors on both sides of the boundary ($z = 0$) represent a coaxial line with the same dimensions, but filled with different material. Therefore, they are defined as

$$\begin{aligned}
\mathbf{e}_n &= \hat{\rho}E_\rho(z<0) + \hat{\phi}E_\phi(z<0) \\
\mathbf{h}_n &= \hat{\rho}H_\rho(z<0) + \hat{\phi}H_\phi(z<0) \\
\tilde{\mathbf{e}}_n &= \hat{\rho}E_\rho(z>0) + \hat{\phi}E_\phi(z>0) \\
\tilde{\mathbf{h}}_n &= \hat{\rho}H_\rho(z>0) + \hat{\phi}H_\phi(z>0)
\end{aligned}$$

where the expressions for E_ρ, E_ϕ, H_ρ, and H_ϕ are defined in appendix F. Applying boundary conditions at the single boundary in figure H.1(a) and assuming a single mode excitation, the system of equations is

$$\begin{aligned}
\mathbf{e}_1 + \sum_{n=1}^{N} R_n \mathbf{e}_n &= \sum_{n=1}^{N} T_n \tilde{\mathbf{e}}_n \\
\mathbf{h}_1 + \sum_{n=1}^{N} R_n \mathbf{h}_n &= \sum_{n=1}^{N} T_n \tilde{\mathbf{h}}_n
\end{aligned}$$

The final step is to apply a testing operator via the integrals

$$\int_{CS} \mathbf{e}_m \cdot \{\} dS \qquad (m = 1, 2, \ldots, N) \qquad \ldots \text{Operator for E-field}$$

$$\int_{CS} \mathbf{h}_m \cdot \{\} dS \qquad (m = 1, 2, \ldots, N) \qquad \ldots \text{Operator for H-field}$$

It is shown in appendix D that unique modes (i.e. unique solutions to the wave equation) that are defined over the same surface of integration, CS, are orthogonal. Therefore, the integrations in this scenario

$$\begin{aligned}
\int_{r_{in}}^{r_b} \int_{0}^{2\pi} \mathbf{e}_m \cdot \mathbf{e}_n \rho \; d\rho d\phi &= 0 \qquad (m \neq n) \\
\int_{r_{in}}^{r_b} \int_{0}^{2\pi} \mathbf{e}_m \cdot \tilde{\mathbf{e}}_n \rho \; d\rho d\phi &= 0 \qquad (m \neq n) \\
\int_{r_{in}}^{r_b} \int_{0}^{2\pi} \mathbf{h}_m \cdot \mathbf{h}_n \rho \; d\rho d\phi &= 0 \qquad (m \neq n) \\
\int_{r_{in}}^{r_b} \int_{0}^{2\pi} \mathbf{h}_m \cdot \tilde{\mathbf{h}}_n \rho \; d\rho d\phi &= 0 \qquad (m \neq n)
\end{aligned}$$

Recognizing that only the $n = 1$ field, $\mathbf{e}_1$ and $\mathbf{h}_1$, carries power into the system then power is only coupled into modes where $m = n = 1$. Therefore, only a single mode propagates through the system.

It is highly likely that the coaxial line step at $z = 0$ in the guided structure of figure H.1(b) will excite higher order modes. For this scenario, the mode dependent transverse vectors on both sides of the boundary ($z = 0$) represent the fields within a coaxial line with differing dimensions and filled with different material. Therefore,

they are defined as

$$\begin{aligned}
\mathbf{e}_n &= \hat{\rho}E_\rho(z<0) + \hat{\phi}E_\phi(z<0) \qquad r_{in} < \rho < r_a \\
\mathbf{h}_n &= \hat{\rho}H_\rho(z<0) + \hat{\phi}H_\phi(z<0) \qquad r_{in} < \rho < r_a \\
\tilde{\mathbf{e}}_n &= \hat{\rho}E_\rho(z>0) + \hat{\phi}E_\phi(z>0) \qquad r_{in} < \rho < r_b \\
\tilde{\mathbf{h}}_n &= \hat{\rho}H_\rho(z>0) + \hat{\phi}H_\phi(z>0) \qquad r_{in} < \rho < r_b
\end{aligned}$$

where the expressions for E_ρ, E_ϕ, H_ρ, and H_ϕ are defined in appendix F.

The system of equations has the same form as the previous example, but the limits of integration are now different. Applying the testing operator for $z < 0$

$$\begin{aligned}
\int_{r_{in}}^{r_a}\int_{0}^{2\pi} \mathbf{e}_m \cdot \mathbf{e}_n \rho \; d\rho d\phi &= 0 \qquad (m \neq n) \\
\int_{r_{in}}^{r_b}\int_{0}^{2\pi} \mathbf{h}_m \cdot \mathbf{h}_n \rho \; d\rho d\phi &= 0 \qquad (m \neq n)
\end{aligned}$$

but for $z > 0$, the fields $m \neq n$ cannot rely on the orthogonality proof of appendix D. The surface[1] over which the fields $z < 0$ are defined is different than the fields $z > 0$ and therefore it is highly likely that the fields are not orthogonal or

$$\begin{aligned}
\int_{r_{in}}^{r_b}\int_{0}^{2\pi} \mathbf{e}_m \cdot \tilde{\mathbf{e}}_n \rho \; d\rho d\phi + \int_{r_b}^{r_a}\int_{0}^{2\pi} \mathbf{e}_m \cdot \{\ 0\ \} \rho \; d\rho d\phi &\neq 0 \qquad (m \neq n) \\
\int_{r_{in}}^{r_b}\int_{0}^{2\pi} \mathbf{h}_m \cdot \tilde{\mathbf{h}}_n \rho \; d\rho d\phi + \int_{r_b}^{r_a}\int_{0}^{2\pi} \mathbf{h}_m \cdot \{\ 0\ \} \rho \; d\rho d\phi &\neq 0 \qquad (m \neq n)
\end{aligned}$$

[1]While reference is made to the surface of integration for the sake of comparing coupling integrals, the particular solutions to Bessel integral are defined between radial boundaries (the circumferential boundaries are repeating). Therefore, it is equivalent to say the particular solutions are defined between a different set of boundaries and therefore orthogonality is highly unlikely.

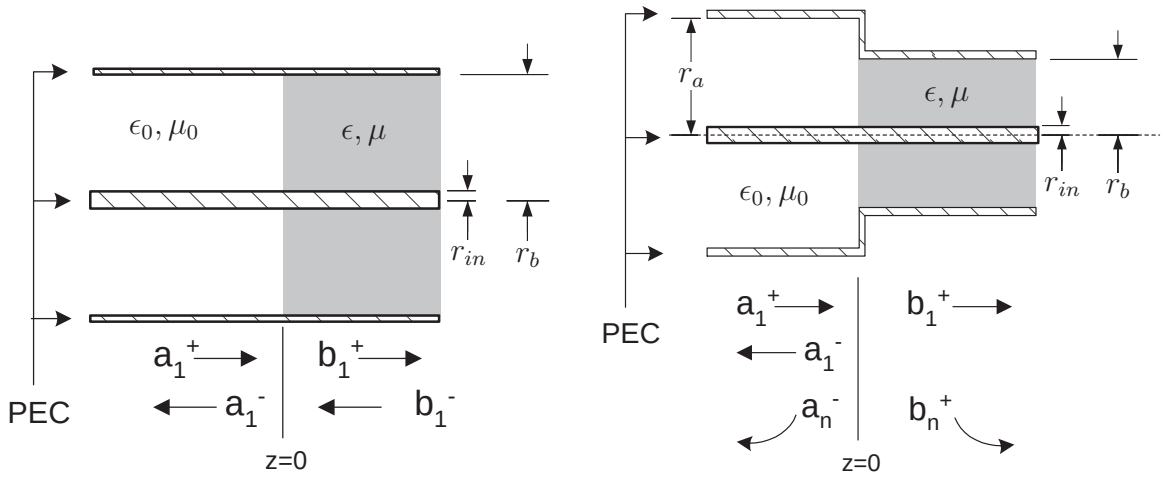

Figure H.1: Transverse discontinuities in a coaxial waveguide (a) will not excite higher order modes. The step-junction discontinuity at $z = 0$ in (b) will couple incident ($n = 1$) energy into higher order ($n > 1$) modes.

Returning to the system of equations for the modal method and using this result produces (considering only the electric field and $N = 2$)

$$\int_{r_{in}}^{r_a}\int_{0}^{2\pi} \mathbf{e}_1 \cdot \mathbf{e}_1 \rho \; d\rho d\phi + R_1 \int_{r_{in}}^{r_a}\int_{0}^{2\pi} \mathbf{e}_1 \cdot \mathbf{e}_1 \rho \; d\rho d\phi = T_1 \int_{r_{in}}^{r_b}\int_{0}^{2\pi} \mathbf{e}_1 \cdot \tilde{\mathbf{e}}_1 \rho \; d\rho d\phi + T_2 \int_{r_{in}}^{r_b}\int_{0}^{2\pi} \mathbf{e}_1 \cdot \tilde{\mathbf{e}}_2 \rho \; d\rho d\phi$$

when applying the testing operator $\mathbf{e}_1$ and

$$R_2 \int_{r_{in}}^{r_a}\int_{0}^{2\pi} \mathbf{e}_2 \cdot \mathbf{e}_2 \rho \; d\rho d\phi \quad = \quad T_1 \int_{r_{in}}^{r_b}\int_{0}^{2\pi} \mathbf{e}_2 \cdot \tilde{\mathbf{e}}_1 \rho \; d\rho d\phi \quad + \quad T_2 \int_{r_{in}}^{r_b}\int_{0}^{2\pi} \mathbf{e}_2 \cdot \tilde{\mathbf{e}}_2 \rho \; d\rho d\phi$$

when applying the testing operator $\mathbf{e}_2$ where only non-zero terms are retained. Physically, if the initial excitation, $\mathbf{e}_1$, couples power into (excites) modes $\tilde{\mathbf{e}}_n$ where $n > 1$, that power is coupled into the remaining modes, $\mathbf{e}_n$ and $\tilde{\mathbf{e}}_n$ for $n > 1$, in the system.

Bibliography

1. Arfken, G. and H. Weber. *Mathematical Methods for Physicists*. Harcourt Academic Press, 5th edition, 2001.

2. Baker-Jarvis, J.R., M.D. Janezic, J.H. Grosvenor Jr., and R.G. Geyer. *Transmission/Reflection and Short-Circuit Line Methods for Measuring Permittivity and Permeability (Tech. Note 1355-R)*. Nat. Inst. Stands. Tech., Dec 1993.

3. Balanis, Constantine A. *Advanced Engineering Electromagnetics*. John Wiley & Sons, 1st edition, 1989. ISBN 0471621943.

4. Chen, L.F., C. K. Ong, C.P. Neo, V.V. Varadan, and V.K. Varadan. *Microwave Electronics Measurement and Materials Characterization*. John Wiley & Sons, 1 edition, 2004.

5. Collin, Robert E. *Field Theory of Guided Waves*. IEEE Press, New Jersey, 2nd edition, 1990.

6. Collin, Robert E. *Foundations for Microwave Engineering*. IEEE Press, New York, 2nd edition, 2000.

7. Dorey, Sean P. *Stepped-waveguide electromagnetic material characterization technique*. Master's thesis, School of Engineering and Management, Air Force Institute of Technology (AU), Wright-Patterson AFB OH, Feb 2003.

8. Gray, Andrew and G.B. Matthews. *A Treatise on Bessel Functions and Their Applications to Physics*. Dover, New York, 1966.

9. Harrington, Roger F. *Time-Harmonic Electromagnetic Fields*. McGraw-Hill, Inc., 1961.

10. Marcuvitz, N. "Waveguide Handbook". *MIT Radiation Laboratory Series*, 10, 1951.

11. McLachlan, N.W. *Bessel Functions for Engineers*. Oxford University Press, London, 1941.

12. Nicolson, A.M. and G.F. Ross. "Measurement of the Intrinsic Properties of Materials by Time-domain Techniques". *IEEE Transactions on Instrumentation and Measurement*, IM-19:377–382, Nov 1970.

13. Ragheb, H.A., A. Sebak, and L. Shafai. "Cutoff Frequencies of Circular Waveguide Loaded With Eccentric Dielectric Cylinder". *IEE Proceedings - Microwave, Antennas and Propagation*, 144, Feb 1997.

14. Tranter, C.J. *Bessel Functions with Some Physical Applications*. Hart Publishing Company, Inc., New York, 1969.

15. Vanzura, E.J., J.R. Baker-Jarvis, J.H. Grosvenor Jr., and M.D. Janezic. "Intercomparison of Permittivity Measurements Using the Transmission Reflection Method in 7-mm Coaxial Transmission Lines". *IEEE Microwave Theory and Tech.*, 42(11), Nov 1994.

16. Watson, G.N. *A Treatise on the Theory of Bessel Functions*. Cambridge University Press, Cambridge, 2nd edition, 1966.

17. Weir, W.B. "Automatic Measurement of Complex Dielectric Constant and Permeability at Microwave Frequencies". *IEEE Proceedings*, volume 62, 33–36. Jan 1974.

18. Whites, Keith W. *Electromagnetic Wave Propagation Through Circular Waveguides Containing Radially Inhomogeneous Lossy Media*. Technical Report M-89/11, US Army Corps of Engineers, Sep 1989.

19. Yee, H.Y. and N.F. Audeh. "Cutoff Frequencies of Eccentric Waveguides". *IEEE Transactions on Microwave Theory and Techniques*, MTT-14(10), Oct 1966.

20. Zhang, L., J. Zhang, and W. Wang. "Correct Determination of TE and TM Cutoff Wavenumbers in Transmission Lines with Circular Outer Conductors and Eccentric Circular Inner Conductors". *IEEE Transactions on Microwave Theory and Techniques*, 39(8), Aug 1991.

REPORT DOCUMENTATION PAGE

Form Approved
OMB No. 0704–0188

1. REPORT DATE *(DD–MM–YYYY)*	2. REPORT TYPE	3. DATES COVERED *(From — To)*
23–03–2006	Master's Thesis	Sep 2004 — Mar 2006

4. TITLE AND SUBTITLE

Air Gap Error Compensation for
Coaxial Transmission Line Method of
Electromagnetic Material Characterization

5a. CONTRACT NUMBER

5b. GRANT NUMBER

5c. PROGRAM ELEMENT NUMBER

6. AUTHOR(S)

Fehlen, Ronald G., Captain, USAF

5d. PROJECT NUMBER

5e. TASK NUMBER

5f. WORK UNIT NUMBER

7. PERFORMING ORGANIZATION NAME(S) AND ADDRESS(ES)

Air Force Institute of Technology
Graduate School of Engineering and Management (AFIT/EN)
2950 Hobson Way
WPAFB OH 45433-7765

8. PERFORMING ORGANIZATION REPORT NUMBER

AFIT/GE/ENG/06-20

9. SPONSORING / MONITORING AGENCY NAME(S) AND ADDRESS(ES)

The Boeing Company
Attn: Dr. Lydell Frasch
PO Box 516
St. Louis, MO 63166
(314) 233-0843 ; lydell.l.frasch@boeing.com

10. SPONSOR/MONITOR'S ACRONYM(S)

11. SPONSOR/MONITOR'S REPORT NUMBER(S)

12. DISTRIBUTION / AVAILABILITY STATEMENT

APPROVED FOR PUBLIC RELEASE; DISTRIBUTION UNLIMITED

13. SUPPLEMENTARY NOTES

14. ABSTRACT

This research analyzes material characterization measurements from 50 Mhz to 3.05 GHz where an axially symmetric air gaps exist between the sample material and the inner or outer conductor. Higher order fields are excited by the air gap and are accounted for through modal analysis methods. A root search minimizes the difference between the calculated scattering parameters from the modal method and the experimentally measured scattering parameters. The root is the permittivity and permeability of the material. This method is tested with a non-magnetic material and a heavily loaded magnetic material. An error analysis based on dimension measurement uncertainty is performed. The method accurately calculates the permittivity of the non-magnetic material for an air gap to material width ratio of 13.6. For a magnetic material with air gap to material width ratio of 0.02, the method accurately calculates the permittivity and permeability using 10 higher modes, but diverges when using more than 10 modes. Accurate determination of the higher order mode wavenumbers is proven critical to the modal method converging.

15. SUBJECT TERMS

Electromagnetic properties, Radar absorbing materials, Theses, Coaxial cables, Material characterization measurements, Modal Field Analysis, Waveguide Discontinuities

16. SECURITY CLASSIFICATION OF:			17. LIMITATION OF ABSTRACT	18. NUMBER OF PAGES	19a. NAME OF RESPONSIBLE PERSON
a. REPORT	b. ABSTRACT	c. THIS PAGE			Dr. Michael J. Havrilla (ENG)
U	U	U	UU	135	19b. TELEPHONE NUMBER *(include area code)* (937) 255–3636, ext 4582; michael.havrilla@afit.edu